

Scuola di Scienze  
Dipartimento di Fisica e Astronomia  
Corso di Laurea magistrale in Astrofisica e Cosmologia

**Adaptive-mesh refinement hydrodynamical simulations  
of cold gas clouds in the hot corona of the Milky Way**

Tesi di Laurea Magistrale

Presentata da:  
**Marco Canducci**

Relatore:  
Chiar.mo Prof. **Filippo Fraternali**

Correlatore:  
Dr. **Lucia Armillotta**



*Look wide, beyond your immediate surroundings and limits,  
and you see things in their right proportion.  
Look above the level of things around you  
and see a higher aim and possibility to your work.*

*- Sir Robert Baden-Powell*



## Abstract

Le galassie *star-forming*, come la Via Lattea, hanno formato stelle durante tutta la propria vita ( $\sim 10$  Gyrs) ad un tasso circa costante di  $\sim 1 - 3M_{\odot}yr^{-1}$  (e.g. Fraternali & Tomassetti 2012). Tipicamente la massa di gas contenuta nel disco di tali galassie può sostenere il processo di formazione stellare solo per pochi Gyr (e.g. Bauermeister et al. 2010). Tale problema, noto come *gas-consumption dilemma*, suggerisce la necessità di un continuo accrescimento di gas freddo da parte del disco della galassia ad un tasso di  $\sim 1M_{\odot}yr^{-1}$  per compensare la conversione di gas in stelle (Sancisi et al. 2008).

Indicazioni cosmologiche mostrano che questo gas proviene dall'Inter Galactic Medium (IGM), che circonda le galassie nella forma di corona calda a temperatura viriale ( $T \sim 10^6 K$ ). Le stime ottenute per la Via Lattea mostrano che la massa barionica della corona è comparabile con la massa stellare presente nel disco (Anderson & Bregman 2011). Queste corone cosmologiche sembrano dunque essere una sostanziale riserva di gas che potrebbe sostenere il processo di formazione stellare agli attuali tassi osservati. Tuttavia, non è ancora chiaro come il gas della corona possa raffreddare e cadere sul disco, infatti temperature di circa  $10^6$  K implicano tempi di cooling di qualche Gyr.

Marinacci et al. (2010) e Armillotta et al. (2016), tramite simulazioni idrodinamiche 2D, hanno mostrato che il gas coronale caldo può raffreddare in maniera efficiente in seguito all'interazione con nubi fontana fredde ( $T \sim 10^4$  K) espulse da feedback stellare fino ad alcuni kiloparsec dal disco galattico. Lo sviluppo dell'instabilità di Kelvin-Helmholtz sulla superficie di contatto tra gas freddo e corona, genera una rottura della nube che porta alla formazione di una coda turbolenta, luogo del mixing tra i due gas. L'interazione tra i due fluidi causa la diminuzione del tempo di cooling di parte del gas coronale e la sua condensazione. I risultati fino ad ora ottenuti mostrano che dopo 60 Myr la massa di gas della corona raffreddato dall'interazione con la nube è circa il 20% della massa iniziale della nube. Questo gas segue la nube nella sua orbita fino alla ricaduta sul disco rendendosi disponibile per la formazione stellare. Le simulazioni sono state eseguite con due codici Euleriani, paralleli e multidimensionali: **ECHO**<sub>++</sub> (Del Zanna et al. 2007) e **ATHENA** (Stone et al. 2008). La limitazione principale di questi codici è la loro struttura a griglia fissa: la risoluzione iniziale è la stessa per l'intero dominio durante tutta l'evoluzione. Con questi codici, simulazioni 3D richiederebbero un tempo di calcolo proibitivo con le risorse a nostra disposizione.

Per poter esplorare il problema attraverso simulazioni 3D riducendo il tempo di calcolo abbiamo scelto di utilizzare un codice MHD, parallelo a griglia adattiva (**Adaptive Mesh Refinement: AMR**): **ENZO** (Bryan et al. 2014).

ENZO utilizza una gerarchia adattiva di griglie a differenti livelli di risoluzione. Il criterio di raffinamento ed il rapporto tra le dimensioni di celle di due livelli consecutivi possono essere scelti dall'utente. La griglia a più bassa risoluzione copre tutto il dominio della simulazione. Quando in una certa regione del dominio è soddisfatto il criterio di raffinamento, vengono create griglie a risoluzione maggiore da sostituire a quelle della regione interessata. Solo queste quindi saranno risolte con maggior precisione, riducendo altamente il tempo di calcolo necessario.

La parte iniziale del lavoro di tesi è incentrata sul confronto tra i risultati ottenuti da simulazioni 2D con ENZO a griglia fissa e quelli prodotti da ATHENA. Nelle prime simulazioni dunque l'AMR non è attivo, in modo da verificare la concordanza dei due codici sotto le stesse condizioni. Per poter effettuare questo confronto si è introdotto in ENZO la stessa trattazione del cooling di ATHENA, mediante la funzione di cooling (Sutherland & Dopita 1993). Nonostante esistano alcune differenze negli algoritmi di risoluzione delle equazioni di Eulero, si è trovato un buon accordo tra i due risultati.

Il passo successivo è lo sviluppo di simulazioni AMR inizialmente 2D, per valutare le differenze tra griglie statiche e griglie adattive. In particolare, confrontando l'evoluzione temporale del gas freddo ( $T < 2 \times 10^4$  K), si è cercato il criterio di raffinamento con il miglior accordo rispetto ai risultati ottenuti nei lavori precedenti. Si è mostrato che il criterio più comunemente usato per tali simulazioni (overdensity) richiede un controllo eccessivo dei parametri e non consente un guadagno in termini di tempo computazionale, rispetto alle simulazioni con codici a griglia fissa. Esplorando varie alternative, si è trovato che il criterio che in minor tempo computazionale garantisce un solido accordo con i risultati a griglia fissa è il criterio *Slope*, applicato alla densità. Si è inoltre dimostrato essenziale ai fini della correttezza dei risultati, includere la nube in una griglia ad alta risoluzione come condizione iniziale.

Utilizzando il criterio *Slope* applicato alla densità, si è prodotta una simulazione AMR 3D a risoluzione massima  $2 \text{ pc} \times 2 \text{ pc}$ , con lo scopo di una trattazione più realistica del problema astrofisico. Tale simulazione ha permesso di stimare una condensazione pari a  $\sim 30\%$  della massa iniziale della nube dopo 60 Myrs di evoluzione. Questa discrepanza rispetto al caso 2D è dovuta alla maggior superficie di contatto tra gas freddo e gas coronale, che permette uno sviluppo più veloce dell'instabilità di KH e quindi un *mixing* più efficiente tra i due fluidi. In questo scenario, la condensazione del gas coronale nella coda turbolenta è favorita, giustificando la sovrastima della condensazione rispetto al caso 2D.

Lo scopo ultimo del lavoro di tesi è ottenere una descrizione più accurata dell'interazione tra disco e corona e determinare la quantità di gas coronale condensata e accresciuta sul disco, in modo da comprendere il legame tra le galassie *star-forming* e l'ambiente in cui esse evolvono.





# Contents

<b>1</b>	<b>Introduction</b>	<b>7</b>
1.1	Gaseous haloes in Star-forming galaxies . . . . .	7
1.1.1	External galaxies . . . . .	8
1.1.2	The Milky Way . . . . .	9
1.2	Gas accretion . . . . .	12
1.2.1	Cold mode . . . . .	13
1.2.2	Hot mode . . . . .	14
1.3	Galactic Fountain . . . . .	15
1.4	This thesis . . . . .	17
<b>2</b>	<b>Introducing ENZO</b>	<b>19</b>
2.1	Euler equations . . . . .	19
2.2	ENZO's Hydro solvers . . . . .	22
2.2.1	Riemann solvers . . . . .	25
2.3	Structured Adaptive Mesh Refinement . . . . .	27
2.3.1	Refinement Criteria . . . . .	31
2.4	Modifications to ENZO . . . . .	34
2.4.1	Radiative cooling . . . . .	35
<b>3</b>	<b>Adiabatic simulations of fountain clouds</b>	<b>39</b>
3.1	Setup of the simulations . . . . .	39
3.2	Non-AMR implementation . . . . .	41
3.3	Introduction of the AMR . . . . .	45
3.3.1	Over-density refining criterion . . . . .	45
3.3.2	Matching the fixed-grid results . . . . .	50
3.3.3	Fine tuning of the overdensity parameters . . . . .	52
3.3.4	Initial high-resolution box . . . . .	55
3.3.5	Other refinement criteria . . . . .	59

<b>4 Simulations with Radiative Cooling</b>	<b>65</b>
4.1 Comparison with adiabatic simulations . . . . .	66
4.2 Temporal resolution . . . . .	67
4.3 AMR simulations . . . . .	72
4.3.1 Over-density criterion . . . . .	73
4.3.2 Other refinement criteria . . . . .	76
4.3.3 Comparison between Refinement criteria . . . . .	80
4.4 3D simulation . . . . .	85
<b>Conclusions</b>	<b>91</b>

# Chapter 1

## Introduction

Over the last few years, evidence has been accumulated of the presence of extended gaseous haloes surrounding disc galaxies, extending to hundreds of kiloparsec away from the galactic plane. This so called *Circumgalactic Medium* (CGM) is supposed to be in continuous interaction with the disc via the exchange of gas. Even though the mechanisms driving these gas flows are still not well understood, the detection of neutral gas up to a few kpc from the plane, seems to suggest that such interaction actually takes place.

This Introduction will initially focus on the observational evidence of galactic haloes, both in external galaxies and in the Milky Way (sec. 1.1), as well as on the detections of the so called *extra-planar gas*: the neutral gas component of the haloes. Section 1.2 illustrates the main features of the two main gas accretion scenarios proposed in order to solve the gas-accretion dilemma, while section 1.3 describes the accretion model here studied. An outline of this work is given in section 1.4.

### 1.1 Gaseous haloes in Star-forming galaxies

It is widely accepted that all star-forming galaxies are enveloped in hot ( $T \sim 10^6$  K) gas haloes extending out to their virial radius (Fukugita & Peebles 2006), called *cosmological coronae*. Cosmological models suggest that such structures could contain the baryonic matter necessary for these galaxies to match the predictions

given their hosting Dark Matter haloes (Komatsu et al. 2009). Thus solving the problem of the so-called missing baryons. However, given the high temperatures and low densities of this gas, its X-ray surface brightness would fall below the sensitivity of the current instrumentation (Bregman 2007), providing a very low detection rate.

### 1.1.1 External galaxies

A few observations of very massive galaxies have shown evidence of extended hot ( $T > 10^6$  K) gas structures at distance beyond 50 kpc from their galactic centre (Bogdán et al. 2013a,b), as shown in fig 1.1. The masses estimated for these haloes are similar to the baryonic masses contained in the disc ( $\sim 10^{11} M_{\odot}$ ) and the gas is extremely rarefied, with densities around  $10^{-3} - 10^{-4} \text{ cm}^{-3}$ .

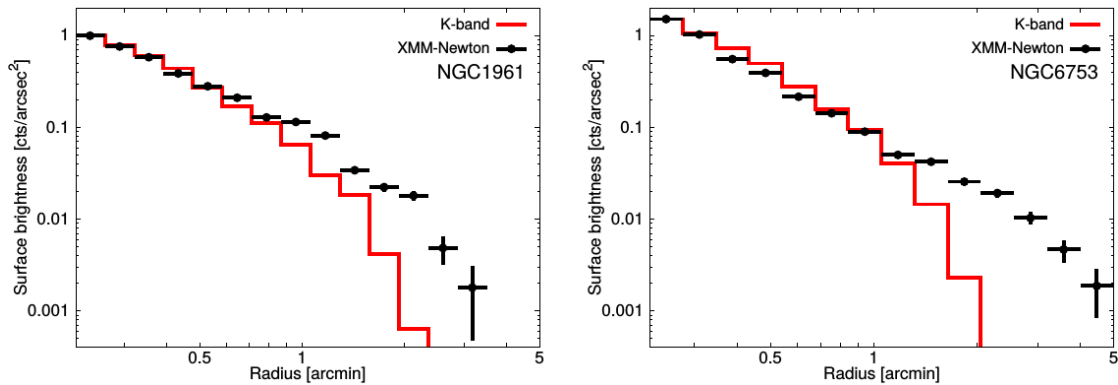


Figure 1.1: X-Ray surface brightness of NGC1961 and NGC6753 as detected by Bogdán et al. (2013a). Emission is detected at distances larger than 50 kpc (57 kpc for the former and 63 kpc for the latter).

The lower component of galactic haloes (close to the disc) is primarily neutral gas. Due to its low column density ( $N_{\text{HI}} = 10^{19-20} \text{ cm}^{-2}$ ), very sensitive observations are required to detect its emission. In edge-on galaxies, it is possible to separate the halo H I emission from that of the disc, as in the case of NGC 891 (Oosterloo et al. 2007). Usually, this gas is referred to as *extra-planar gas* and its mass is estimated to be around 10 – 30% of the total H I mass of the galaxy (Sancisi et al. 2008). The extra-planar gas, shows a decline of the rotational velocity

with increasing height above the galactic plane. A vertical velocity gradient of

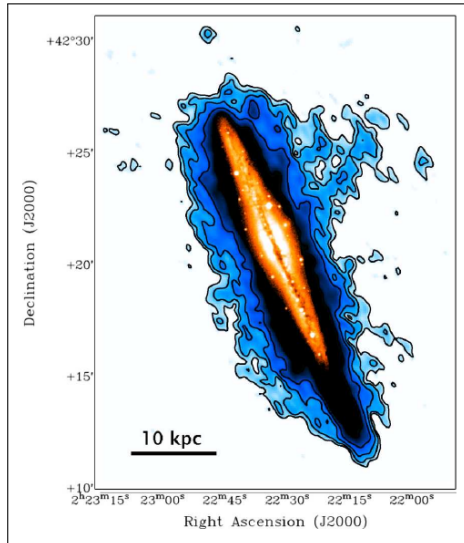


Figure 1.2: Contours of H I emission map of NGC 891 overlaid on the optical image of the galaxy (Oosterloo et al. 2007).

$\sim 15 - 30 \text{ km/s kpc}^{-1}$  has been measured in a significant number of spiral galaxies (Fraternali et al. 2002; Oosterloo et al. 2007; Zschaechner et al. 2011; Lucero et al. 2015). Also, the kinematics of the extra-planar H I gas shows the presence of non-circular motions and in particular a possible large-scale inflow (Fraternali et al. 2001). It has been argued that this extra-planar gas in the vicinity of the plane, could be originated by the galactic fountain mechanism, where cold gas clouds could be ejected from the disc into the corona by stellar feedback (Melioli et al. 2008, 2009) following ballistic trajectories and falling back onto the disc in orbital times  $\sim 80 - 100 \text{ Myrs}$  (Fraternali & Binney 2006). A brief description of this phenomenon is outlined in sec. 1.3.

The detection of high-velocity features in nearly face-on galaxies (Boomsma et al. 2008) seems to confirm the galactic origin of this gas, and links its spatial distribution to the star formation in the disc.

### 1.1.2 The Milky Way

As a disc galaxy, the Milky Way presents the same gaseous components detected in external galaxies. The existence of a hot ( $T \gtrsim 10^6$ ) gas halo surrounding the Milky Way has been proposed by Spitzer (1956) as a way to provide pressure confinement to the High-Velocity Clouds (HVCs). Since then, the search for a low-density, high-temperature gaseous medium has been extremely important, as a way to link observational properties of the Galaxy to cosmological structure formation (e.g. Oort (1966)). The main evidence of the presence of this gas however, are mostly indirect: the head-tail structures of HVCs (Brüns et al. 2000; Putman et al. 2011), the dispersion measure of pulsars in the Galactic halo (Gaensler et al. 2008) and

ram pressure stripping of dwarf galaxies in the Local Group (Grcevich & Putman 2009). A more direct evidence of this gas comes from the OVII and OVIII emission lines in the soft X-ray background (Miller & Bregman 2015) and OVII and OVIII absorption lines in quasar spectra (e.g. Bregman & Lloyd-Davies (2007)). Using these X-ray absorption lines, the density of the inner halo ( $d < 20$  kpc) has been estimated to be  $n_H \approx 8 \times 10^{-4} \text{ cm}^{-3}$ , while the dispersion measure of pulsars give an average coronal density slightly lower:  $n_H \approx 2 \times 10^{-4} \text{ cm}^{-3}$ . Despite these detections, it is still unclear if the hot gas can extend to the virial radius of the galaxy, and what is its mass. But for  $d < 250$  kpc, the total mass of the corona is estimated to be  $M_{\text{Corona}} \approx 10^{10} - 10^{11} M_{\odot}$  (Anderson & Bregman 2010; Gupta et al. 2012; Salem et al. 2015)

The cold ( $T \lesssim 10^4$  K) component of the Galactic halo is mainly detected in the High- and Intermediate- Velocity clouds (HVCs and IVCs respectively). HVCs are neutral and ionized clouds whose velocities in the local standard rest deviate by more than  $\sim 90$  km/s from the speed predicted by differentially rotating thin disc (Wakker et al. 2004; Kalberla et al. 2005), while IVCs have deviation velocities  $|v_{\text{dev}}| = 30 - 90$  km/s (Wakker 2001; Wakker et al. 2004).

## HVCs

The sky distribution of HVCs is quite complex and has a total covering fraction in 21cm of  $f_c \approx 0.35$  at neutral gas column densities  $N_{\text{HI}} = 7 \times 10^{17} \text{ cm}^{-2}$  (Wakker et al. (2004) and references therein). The main structures are Complex C, the Magellanic Stream (MS), Complex A, Complex H, the Anti-Center Cloud and Complexes WA - WE (Fig. 1.3, top panel). The MS spans a distance range of  $d = 50 - 100$  kpc from the galactic disc and together with Complexes WA and WE is generated by the interaction between the Milky Way and two of its satellite dwarf galaxies: Large Magellanic Cloud (LMC) and Small Magellanic Cloud (SMC).

The distances of the other HVCs have been determined using the *bracketing method*. The spectrum of a halo star at a known distance in the direction of the cloud is examined and if absorption lines are seen, then it is inferred that the cloud is in front of the star, while if no absorption features are detected, the cloud

lays behind it. The typical distances of HVCs are  $\lesssim 10$  kpc (except for the MS). As for the metallicity, it is generally derived a value of  $Z \sim 0.1 Z_{\odot}$  (Wakker et al. 2004), with small deviations depending on the specific cloud. For instance, Complex C metallicity has been constrained to 0.15 solar with a large spread (Sembach et al. 2004), complex A metallicity is estimated around  $0.1 - 0.4 Z_{\odot}$ .

The overall low metallicity of these structures is usually explained assuming an extragalactic origin and in particular by two main scenarios: infall from intragroup gas (pre-enriched intergalactic medium), or material stripped from satellite dwarf galaxies accreting onto the Milky Way. However, a galactic origin is also possible. In their work, Fraternali et al. (2015) show how the properties of Complex C can be explained assuming a galactic-fountain origin and condensation from the CGM.

## IVCs

The most relevant features in IVC gas are IV Arch, IV Spur, Complex K (in the northern emisphere), the Anticenter (AC) shell and Pegasus-Pisces (PP) Arch (in the southern emisphere). As afore mentioned, the deviation velocities of these structures are around  $|v_{\text{dev}}| = 30 - 90$  km/s. Their distances from the plain are measured via the bracketing method and generally do not exceed 2.5 kpc; furthermore, many of the IVC complexes are spatially and kinematically connected with 21 cm disc gas and their individual masses are of the order of  $10^5 M_{\odot}$ , giving an estimate of the total mass of this gas  $\sim 10^6 M_{\odot}$ . Marasco & Fraternali (2011) show that they are the local manifestation of the extraplanar layer surrounding the MW and extending to vertical heights of  $1.6_{-0.4}^{+0.6}$  kpc. In general, a higher metallicity with respect to the HVCs is found via absorption-line measurements (e.g. Wakker (2001)). The high metallicity of IVCs is the main indication that such structures cannot have formed via extragalactic accretion, but must have galactic origin. In particular, considering also their distribution in the disc-halo interface of the Milky Way, the favored scenario for the origin of IVCs is the galactic fountain mechanism (Shapiro & Field 1976; Bregman 1980; Norman & Ikeuchi 1989).

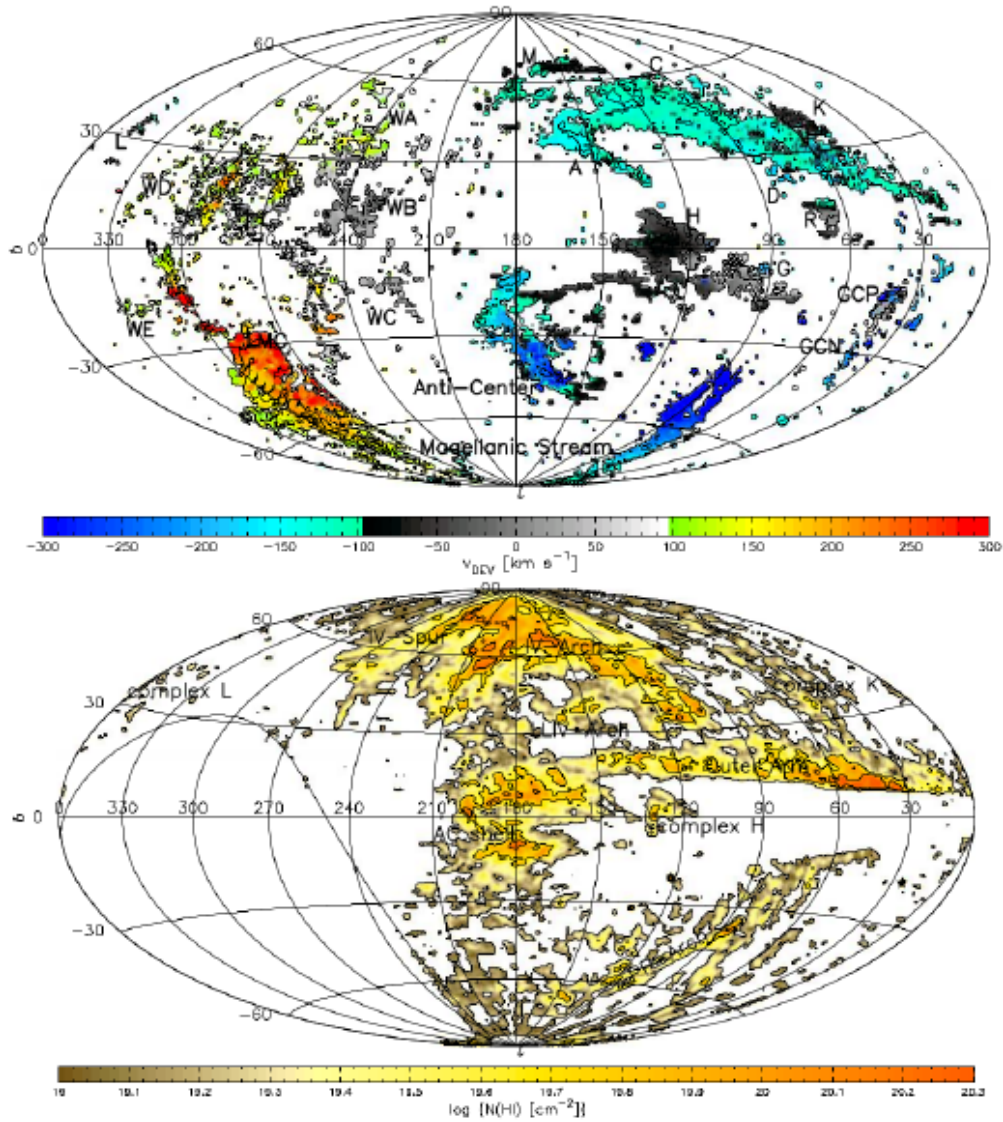


Figure 1.3: Aitoff projection all-sky map showing the spatial distribution of HVCs (top panel) with colours indicating  $v_{dev}$  and IVCs (bottom panel) with contours at  $1$ ,  $5$  and  $12 \times 10^{19} \text{ cm}^{-3}$  in H I column density.

## 1.2 Gas accretion

A long standing problem in the evolution of Milky Way-type galaxies is how they can sustain Star Formation (SF) for cosmological times. It is well known that the amount of gas contained in their discs is sufficient to maintain the current Star

Formation Rates (SFR), almost constant throughout their lives ( $\sim 10$  Gyrs, e.g. Fraternali & Tomassetti (2012)), for a few Gyrs only (*gas-consumption dilemma*). Furthermore, the gas content of such galaxies has remained roughly unchanged throughout the Hubble Time (Zafar et al. 2013), thus the galaxy needs a constant replenishment of gas from the outside at a rate of  $\sim 1 M_{\odot}\text{yr}^{-1}$  (Sancisi et al. 2008). It is still debated how this gas can be gathered from the intergalactic medium, but two main scenarios have been proposed over the years: the *Cold mode* and the *Hot mode accretion*.

### 1.2.1 Cold mode

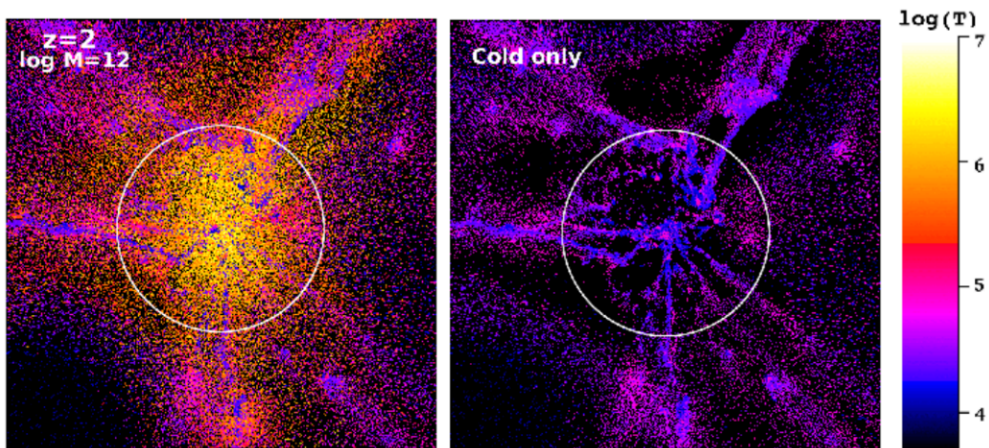


Figure 1.4: Temperature of the gas in Milky Way mass haloes at  $z = 2$  simulated with the Smoothed Particle Hydrodynamics (SPH) code Gadget-3. Panels show the gas in a region of  $1h^{-1}$  Mpc (comoving) on a side and  $1h^{-1}$  Mpc (comoving) in projected depth. The virial radius is shown as the circles. The halo mass is  $M_h = 1.1 \times 10^{12} M_{\odot}$ ; left panel shows all gas particles, while left panel shows only the gas with temperature  $T < 10^5$  K (adapted from Kereš et al. (2009)).

Galaxies with halo masses below  $10^{12} M_{\odot}$  are supposed to be dominated by the cold mode accretion. This mass threshold is mildly dependent on redshift, but as the hierarchical structure formation model implies that less massive structures formed first, it tells us that at high redshifts ( $z > 2$ ), the cold mode must have been the dominant accretion mechanism (Kereš et al. 2009). This model predicts that filaments of cold gas can go through the dark matter (DM) halo reaching its

central galaxy on timescales similar to the free fall time. In figure 1.4 a cosmological simulation is reported where the cold filaments can be seen to reach, mostly unscathed, the central galaxy hosted by a  $10^{12} M_{\odot}$  halo.

This accretion mode is permitted if the cooling time of the halo gas is shorter than the free-fall time. In this case, shock-heating due to the collapse of gas in the DM halo and to its collisional nature, does not take place. Any shock-heated material would cool and collapse so rapidly that it would not be able to sustain the shock front itself (Binney 1977).

### 1.2.2 Hot mode

When the mass of the halo is larger than  $10^{12} M_{\odot}$ , the Hot mode accretion mode becomes dominant. Compared to the previous case, the cooling time of these haloes is larger than the free fall time, but smaller than the Hubble time. Then, gas infalling from the IGM into the DM halo is shock-heated to almost the virial temperature of the halo (a few  $10^6$  K). At these temperatures, the gas resides in quasi-hydrostatic equilibrium with the DM potential well (Rees & Ostriker 1977). The gas then is able to cool and sink into the center of the potential where it is converted into stars, starting from regions near the central galaxy and later moving to higher distances.

Given temperatures around  $T \sim 2 \times 10^6$  K (Bregman et al. 2015) and electron densities  $n_e \sim 5.4 \times 10^{-4} \text{ cm}^{-3}$  (Anderson & Bregman 2011) the cooling time is  $> 1$  Gyrs. Thus it is still not clear how the coronal gas is able to cool down. An hypotheses proposed for solving this problem was that cold clouds could form due to the development of thermal instabilities in the corona (Kaufmann et al. 2006). However, it has been shown that heat conduction and buoyancy have as a net effect the damping of thermal instabilities: cold clouds with sizes smaller than 10 kpc can form only at distances larger than 100 kpc from the plane (Binney et al. 2009; Nipoti & Posti 2014), in contradiction with the spatial distribution of HVCs. Furthermore, SPH, with an appropriate treatment of phase mixing and Adaptive Mesh Refinement (AMR) cosmological simulations of MW-type galaxies, show that spontaneous cooling through formation of thermal instabilities in the corona should not occur (Joung et al. 2012; Hobbs et al. 2013).

## 1.3 Galactic Fountain

In order to explain the cooling of the coronal gas, thus justifying the hot mode accretion, Fraternali & Binney (2006) built a dynamical model of fountain clouds ejected from the disc into the coronal gas, following ballistic trajectories in orbital times around 100 Myrs. Applying this model to the 21 cm observations of the extraplanar gas of two nearby spiral galaxies (NGC891 and NGC 2403) they were able to reproduce its H I vertical distribution. At first, this model was not able to match the vertical gradient of the rotational velocity. However, if accretion from the ambient medium onto the clouds is permitted (Fraternali & Binney 2008), then the velocity gradient can be explained as a loss of angular momentum by the fountain clouds due to this interaction. Being the accretion rate the only free parameter in this model and finding a value similar to those two galaxies' SFR, they were able to move the quest for a mechanism able to sustain Star Formation over cosmic time to the process driving gas accretion onto galactic fountain clouds.

In order to study this interaction, Marinacci et al. (2010) performed 2D high resolution hydrodynamical simulations with the fixed-grid code ECHO++ (Del Zanna et al. 2007), of a cold ( $T = 10^4$  K) disc-like metallicity cloud travelling through the hot ( $T = 10^6$  K) coronal gas of the MW. This motion produces a Kelvin-Helmholtz (KH) instability at the interface between the cloud and the corona, that gradually disrupts the cloud forming a turbulent wake of mixed gas. This mixing drastically reduces the cooling time of the coronal gas, now able to cool down efficiently enough to condense in the wake and be dragged by the cloud back onto the disc. Furthermore, Marinacci et al. (2011) found that a relative velocity threshold between the cloud and the corona exists below which the hot corona stops absorbing momentum, suggesting that the corona must rotate, but with a lower velocity with respect to that of the disc.

Using the model of Fraternali & Binney (2008), Marasco et al. (2012) were able to reproduce the H I emission of the IVCs, thus proving their galactic origin. They found that this mechanism induces an accretion of coronal gas onto the disc at a rate of  $\sim 2 \text{ M}_{\odot}\text{yr}^{-1}$ . Moreover, including the condensation mechanism implemented by Marinacci et al. (2010), Marasco et al. (2013) could reproduce positions and velocities of most of the warm absorbers observed in the Galactic

halo (an artistical representation of the model is presented in fig. 1.5). It has also been demonstrated by Armillotta et al. (2016), that thermal conduction does not play an essential role in the condensation mechanism. By performing similar simulations as Marinacci et al. (2010) with the fixed-grid code ATHENA, and with a specific treatment of thermal conduction, they estimated that the latter has the only effect of delaying the condensation of the coronal gas onto the cloud's wake. The authors, also found that condensation is efficient only for haloes with masses below  $10^{13} M_{\odot}$ , implying that the ability to cool the corona decreases going from late-type to early-type disc galaxies.

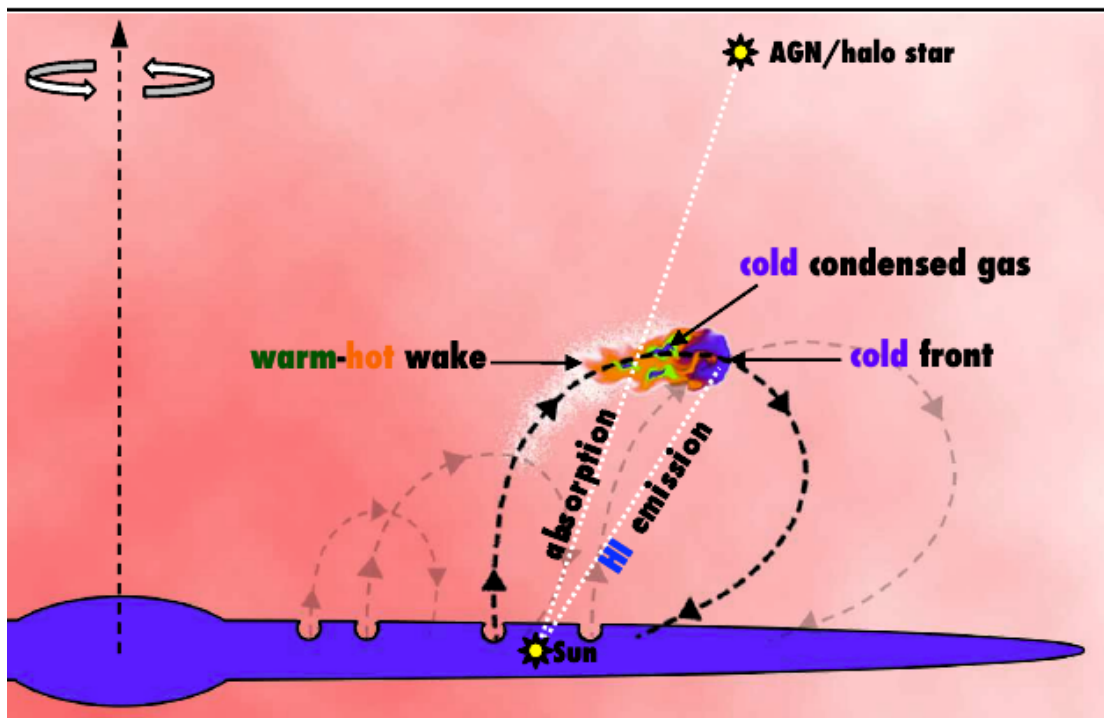


Figure 1.5: Artistical representation of the Galactic Fountain model described in the text. The cold cloud, initially spherical, while moving through the hot medium, gets disrupted and in its wake mixes with the hot coronal gas. The head of the cloud and the densest knots are expected to be detected via H I emission, while the warmer gas in the wake can be detected in absorption in spectra of background halo stars or QSOs.

## 1.4 This thesis

In the previous sections we outlined a schematic picture of the role of galactic haloes in the evolution of star-forming galaxies. We explained the main accretion scenarios, capable of sustaining SF over cosmic times and we pointed out the importance of well describing the interaction between galactic discs and haloes. In particular, we denoted as essential the condensation of coronal gas onto a galactic fountain's cloud wake, based on the model developed by Marinacci et al. (2010). In this work, we performed hydrodynamical simulations of cold galactic fountain's clouds moving through a hot corona as described by Marinacci et al. (2010) and Armillotta et al. (2016), but we move to a more practical and fast computing scheme: Adaptive Mesh Refinement. This technique uses certain refinement criteria to identify interesting regions in the computational domain and in these regions only increase the resolution, while the remaining part of the domain is left at a lower resolution. This selective behaviour generally speeds up the computation.

We aim at finding similar results for condensation obtained with fixed-grid codes and, given the gain in computational speed, we perform a 3D high-resolution hydrodynamical simulation, otherwise extremely time consuming. In a three dimensional representation of the problem, being the contact surface between the cloud and the coronal gas larger than in a 2D geometry, we do expect a higher condensation. Furthermore, a more realistic analysis of the problem could place an accurate constraint on the accretion rate due to this process.

In chapter 2 we present the parallel, (magneto-)hydrodynamic, AMR code ENZO used to perform all the simulations in this work. An accurate description of its automated spatial and temporal refinement can be found there, together with the modifications performed to the code in order to compare its results with those obtained in previous works.

In chapter 3 we describe the simulations performed when no radiative cooling is allowed. The cloud-corona interaction results in the development of a KH instability, but not being able to radiatively cool, the cold gas gradually evaporates. We present the different refinement criteria used, with particular attention dedicated to the over-density criterion, as one of the most widely used.

Chapter 4 shows what changes in the results when radiative cooling is introduced.

We compare there the results obtained with ENZO with those found by Armillotta et al. (2016) using ATHENA (Stone et al. 2008). Also, the 3D results are presented, and a new estimate of the condensation is found.

Chapter 5 contains a summary and the main results of this work.

# Chapter 2

## Introducing ENZO

In this work we used the AMR, magneto-hydrodynamical, parallel code ENZO to perform the hydrodynamical simulations of this Thesis. This chapter is dedicated to the description of ENZO's main features. An explanation of the modifications we made to the code can also be found here. The reason behind these modifications is the search for an agreement with the results obtained using ATHENA: a fixed-grid code. Our first aim is to evaluate how the introduction of AMR influences the outcome of a previously treated problem.

### 2.1 Euler equations

Considering a fluid in its entirety it is possible to define it as a continuum as long as the mean free path of its particles ( $\lambda$ ) is much smaller than the characteristic physical scale-length of the system ( $L$ ). When this happens a fluid element  $dV$  can be defined as a volume (often called Control Volume), whose linear length is between  $\lambda$  and  $L$ , containing all the fluid's particles enclosed in area  $S$ . If this condition holds, the number of particles in the volume is large so that we can define a mean velocity  $\mathbf{u}$  describing the motion of  $dV$ . Given that the typical length of interaction between particles is much smaller than the physical size of the control volume, all particles are forced at any time into a random walk around  $\mathbf{u}$ . If we denote with  $dV'$  the translation of each point of the fluid element  $dV$  through the mean velocity  $\mathbf{u}$  over a generic time interval  $\Delta t$ , we do not only

expect a conservation of the total number of particles, but also that the particles contained in  $dV'$  are the same ones previously enclosed in  $dV$  (only particles on the volume surface could escape the fluid element, but they could also be replaced by neighboring ones) (Shu 1991). The mean free path of a gas particle can be approximated as  $\lambda \sim (n\sigma)^{-1}$ , where  $n$  is the number density of the gas and  $\sigma$  the particle cross section. Given the very low densities for astrophysical fluids (ranging from  $10^6 \text{ cm}^{-3}$  for molecular clouds at temperature of order 10 K to  $10^{-2} \text{ cm}^{-3}$  in the Hot Ionized Medium, HIM, at temperatures of order  $10^6$  K) and also the low cross section (as an inferior limit computed for an hydrogen atom)  $\sigma \sim 10^{-15} \text{ cm}^2$ , the mean free path is at most of order few  $10^{16} \text{ cm} \sim 10^{-2} \text{ pc}$  (worst case scenario: HIM). In any case, the typical sizes of the analysed problem are at least two orders of magnitude greater, thus we can treat the fluid as a continuum and apply the equations of hydrodynamics.

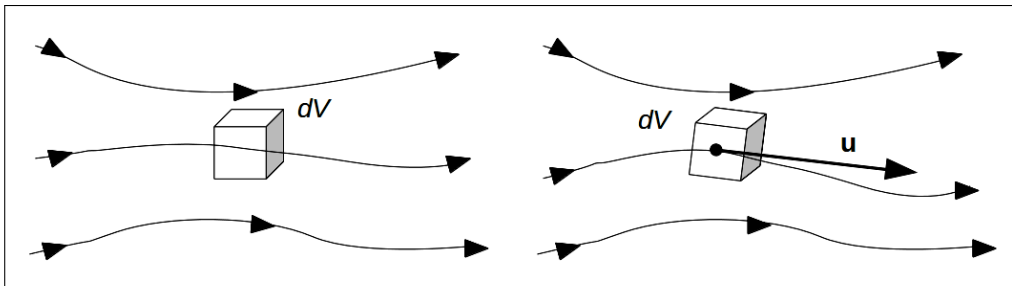


Figure 2.1: Left and right sketches are a schematical representation of Eulerian and Lagrangian approach respectively.  $\mathbf{u}$  is the fluid velocity and  $dV$  the infinitesimal control volume (adapted from Anderson (1995)).

The derivation of the hydrodynamical equations is not unique because it can be done following two main approaches: Eulerian and Lagrangian. Let's consider the same control volume  $dV$  discussed above. This volume could be either fixed in space with the fluid moving through it (Eulerian approach), or it could be moving with the fluid such that the same particles are always included (Lagrangian approach), as shown in fig. 2.1. The fluid flow equations obtained by direct application of the conservation laws (for mass, momentum and energy) to the finite control volume are in *integral* form, but they can be manipulated in order to become partial differential equations (PDEs). This set of equations is usually called *Euler equations* and a general analytical solution is not yet known. In the case of a

fixed-in-space control volume the obtained equations are said to be in *conservation* form, while in their PDE version they are referred to as in *nonconservation* form. ENZO is an Eulerian method that solves the *conservative* (Eulerian) form of (magneto-)hydrodynamical equations. In a 3D geometry the equations of conservation of mass, momentum and energy for an inviscid and un-magnetized fluid in the absence of a gravitational potential, and in Cartesian coordinates, are respectively:

$$\frac{\partial \rho}{\partial t} + \nabla \cdot (\rho \mathbf{u}) = 0 \quad (2.1a)$$

$$\frac{\partial(\rho \mathbf{u})}{\partial t} + \nabla \cdot (\rho \mathbf{u} \otimes \mathbf{u}) = -\nabla P \quad (2.1b)$$

$$\frac{\partial \rho E}{\partial t} + \nabla \cdot [(\rho E + P)\mathbf{u}] = 0 \quad (2.1c)$$

Here  $\rho$ ,  $E$  and  $\mathbf{u}$  are the fluid density, total energy per unit mass per unit volume and velocity respectively. In particular, the energy density  $E$  is defined as  $E = e + u^2/2$ , where  $e$  is the internal energy density. The symbol  $\otimes$  represents the dyadic product between two vectors. Equations 2.1a - 2.1b - 2.1c represent a system of quasi-linear, first order PDEs, hyperbolic conservation laws. This system can be written in the following form:

$$\frac{\partial \mathbf{U}}{\partial t} + \nabla \cdot \mathbf{F}(\mathbf{U}) = 0 \quad (2.2)$$

where  $\mathbf{U}$  is the vector of *conserved* variables  $(\rho, \rho \mathbf{u}, \rho E)^T$  (apex  $T$  representing the transpose operator) and  $\mathbf{F}$  is the flux matrix  $\mathbf{F} = (\rho \mathbf{u}, \rho \mathbf{u} \otimes \mathbf{u} + P, (\rho E + P)\mathbf{u})^T$ . Expanding the spatial derivative, the system 2.2 can be written as following:

$$\frac{\partial \mathbf{U}}{\partial t} + \sum_{n=1}^3 \frac{\partial \mathbf{F}_n(\mathbf{U})}{\partial \mathbf{U}} \frac{\partial \mathbf{U}}{\partial x_n} = \frac{\partial \mathbf{U}}{\partial t} + \sum_{n=1}^3 \mathbf{J}_n \frac{\partial \mathbf{U}}{\partial x_n} = 0 \quad (2.3)$$

where  $\mathbf{F}_n$  is the  $n$ -th column of matrix  $\mathbf{F}$  and  $\mathbf{J}_i$  is the *Jacobian matrix*, defined as:  $\mathbf{J}_i \equiv \partial \mathbf{F}_i(\mathbf{U}) / \partial \mathbf{U}$ . The definition of hyperbolic PDEs requires matrix  $\mathbf{J}_n$  to have  $m$  real eigenvalues  $\lambda_i$  and a complete set of linearly independent eigenvectors. The eigenvalues of the Jacobian matrix for the Euler equations are  $\lambda^+ = u_i + c_s$ ,  $\lambda^0 = u_i$  and  $\lambda^- = u_i - c_s$ , where  $c_s$  is the sound speed of the fluid and  $u_i$  its velocity along

direction  $i$ . Equation 2.3, locally assumes the form of a decoupled system of wave equations, with respective propagation speeds given by the eigenvalues  $\lambda_i$ . Due to the non linearity of Euler equations however, the interaction between waves may lead to the formation of discontinuous solutions, with propagation speeds different from the eigenvalues, such as *shock waves* and *tangential* (and in particular *contact*) discontinuities<sup>1</sup>.

Many hydrodynamical codes use the fact that the Euler equations are an hyperbolic set of PDEs in order to solve them. In general, the solution of a system of PDEs is performed upon the introduction of Initial Conditions (IC) for the conservative variables; the system of equations containing both PDEs and ICs is called Initial Value Problem (IVP).

## 2.2 ENZO's Hydro solvers

In order to solve the Euler equations, four different methods are implemented in ENZO:

- Direct Eulerian Piecewise Parabolic Method (**DE-PPM**, Colella & Woodward (1984)), lately extended to cosmology by Bryan et al. (1995). This method is an explicit, higher-order version of Godunov's methods for ideal gas dynamics, only at use in pure hydrodynamical problems. It has at its disposal a spatially third-order accurate piecewise parabolic monotonic interpolation as well as a nonlinear Riemann solver for shock capturing. This scheme accurately represents both smooth gradients and discontinuities over linear interpolation;
- ZEUS: a finite-difference method alternative to the Godunov's approach developed by Stone & Norman (1992a,b). The equations are solved by definition of two staggered grids, one of which containing cell-centered quantities (density and total energy) while the other, velocity (the main difference between previous methods is indeed the face-centered definition of velocity).

---

<sup>1</sup>The former consists in a jump in all the fluid's variables except the tangential velocity component and the latter in density and tangential component of velocity only (just density in a contact discontinuity).

The algorithm is divided into two steps: the *Source step* updates momentum and energy values taking into account pressure gradients and gravity forces; the *Transport step* solves advection equation for conserved quantities across cells' boundaries.

- Godunov MUSCL, only HD (LeVeque 2002; Toro 1997), with Dedner divergence cleaning as an extension to MHD (Dedner et al. 2002)(HD / MHD);
- Godunov MHD with Constrained Transport (MHD-CT): Second-order in time and space, preserves the divergence constraint,  $\nabla \cdot B$ , to machine precision through the Constrained Transport (CT) methods described by Balsara & Spicer (1999); Gardiner & Stone (2005).

In each simulation performed in this work, the **DE-PPM** method is used. A detailed description of this method can be found in Colella & Woodward (1984), but we chose to outline the main features here for completeness.

The Euler equations are solved on a three-dimensional Cartesian grid. The continuous coordinates  $x$ ,  $y$  and  $z$  are discretized in  $N_x$ ,  $N_y$  and  $N_z$  cells within a finite computational domain of size  $L_x$ ,  $L_y$  and  $L_z$ . In the case of a uniform grid, the size of each cell on the  $x$ -,  $y$ - and  $z$ -directions are  $\Delta x = L_x/N_x$ ,  $\Delta y = L_y/N_y$  and  $\Delta z = L_z/N_z$  respectively, while the respective indices are  $i$ ,  $j$  and  $k$ . The boundaries of each  $(x_i, y_j, z_k)$  cell are then:  $([x_{i-1/2}, x_{i+1/2}], [y_{j-1/2}, y_{j+1/2}], [z_{k-1/2}, z_{k+1/2}])$ , with a spatial separation  $\Delta x$ ,  $\Delta y$  and  $\Delta z$  respectively. The vector  $\mathbf{U}$  containing the conserved continuous variables can then be discretized assigning at each cell its volume weighted average value between the cell's boundaries:

$$\mathbf{U}_{i,j,k}^n = \frac{1}{\Delta x \Delta y \Delta z} \int_{x_{i-1/2}}^{x_{i+1/2}} \int_{y_{j-1/2}}^{y_{j+1/2}} \int_{z_{k-1/2}}^{z_{k+1/2}} \mathbf{U}_n(x, y, z, t) dx dy dz \quad (2.4)$$

Equation 2.3 can be rewritten in order to explicit the fluxes through a cell's face along each direction:

$$\frac{\partial \mathbf{U}}{\partial t} = \frac{\partial \mathbf{K}}{\partial x} + \frac{\partial \mathbf{G}}{\partial y} + \frac{\partial \mathbf{H}}{\partial z} \quad (2.5)$$

$\mathbf{K}$ ,  $\mathbf{G}$  and  $\mathbf{H}$  being the fluxes along  $x$ -,  $y$ - and  $z$ -directions. In this formulation, using the divergence theorem, the Euler equations can be solved in their integral

form:

$$\frac{d}{dt} \iiint_V \mathbf{U} dV + \iint_{A_x} \mathbf{K} \cdot \mathbf{n} dA_x + \iint_{A_y} \mathbf{G} \cdot \mathbf{n} dA_y + \iint_{A_z} \mathbf{H} \cdot \mathbf{n} dA_z = 0 \quad (2.6)$$

Where  $V$  is the volume of the fluid element,  $A_x$ ,  $A_y$  and  $A_z$  the areas enclosing the volume (surface boundary) on each direction and  $dA_x$ ,  $dA_y$  and  $dA_z$  the corresponding area elements, while  $\mathbf{n}$  is the normal versor to each  $dA_i$ . Equation 2.6 states that the change rate over time of the conserved variables in  $\mathbf{U}$  depends only on the total flux of those variables through the surface of the control volume.

ENZO works by discretization of equation 2.6 over a finite timestep  $\Delta t$ :

$$\begin{aligned} \mathbf{U}_{i,j,k}^{n+1} = \mathbf{U}_{i,j,k}^n &- \frac{\Delta t}{\Delta x} (\mathbf{F}_{i+1/2,j,k}^{n+1/2} - \mathbf{F}_{i-1/2,j,k}^{n+1/2}) \\ &- \frac{\Delta t}{\Delta y} (\mathbf{G}_{i,j+1/2,k}^{n+1/2} - \mathbf{G}_{i,j-1/2,k}^{n+1/2}) \\ &- \frac{\Delta t}{\Delta z} (\mathbf{H}_{i,j,k+1/2}^{n+1/2} - \mathbf{H}_{i,j,k-1/2}^{n+1/2}) \end{aligned} \quad (2.7)$$

Where  $t^{n+1} = t^n + \Delta t$  and  $\Delta t$  is computed by imposing the Courant-Friedrichs-Lewy condition (see sec. 2.3). The vectors of the time- and area-averaged fluxes are:

$$\mathbf{F}_{i-1/2,j,k}^{n+1/2} = \frac{1}{\Delta V} \int_{t^n}^{t^{n+1}} \iint_{A_x} \mathbf{F}(x_{i-1/2}, y, z, t) dA_x dt \quad (2.8a)$$

$$\mathbf{G}_{i,j-1/2,k}^{n+1/2} = \frac{1}{\Delta V} \int_{t^n}^{t^{n+1}} \iint_{A_y} \mathbf{G}(x, y_{j-1/2}, z, t) dA_y dt \quad (2.8b)$$

$$\mathbf{H}_{i,j,k-1/2}^{n+1/2} = \frac{1}{\Delta V} \int_{t^n}^{t^{n+1}} \iint_{A_z} \mathbf{H}(x, y, z_{k-1/2}, t) dA_z dt \quad (2.8c)$$

From eq. 2.8 the solution is shown to depend on the values of the fluxes at the cells' boundaries, so that an accurate computation of the fluxes is needed. These in return, depend on the values of the hydrodynamical variables at the cells' boundaries. However, the hydrodynamical variables are cell-centered, so that an interpolation is needed in order to compute them at the cells' boundaries. The precision of these values is strictly related to the method used for interpolation. In this work a Piecewise Parabolic Method (PPM) is used.

At first, monotonic piecewise parabolic (third-order) interpolations in one dimen-

sion are computed for  $p$ ,  $\rho$ , and  $\mathbf{u}$ . The pressure is determined by inversion of the equation of state:

$$e = \frac{p}{(\gamma - 1)} \quad (2.9)$$

The interpolation formula for some variable  $q$  is given by:

$$q_j(x) = q_{L,j} + \tilde{x}[\Delta q_j + q_{6,j}(1 - \tilde{x})] \quad (2.10a)$$

$$\tilde{x} \equiv \frac{x - x_{j-1/2}}{\Delta x_j}, \quad x_{j-1/2} \leq x \leq x_{j+1/2} \quad (2.10b)$$

$q_{L,j}$  is the value of  $q$  at the left edge of zone  $j$ , while  $\Delta q_j$  and  $q_{6,j}$  are analogous to the slope and first-order correction to the slope of  $q$  (Colella & Woodward 1984):

$$\Delta q_j \equiv q_{R,j} - q_{L,j}, \quad q_{6,j} \equiv 6[q_j - 1/2(q_{L,j} + q_{R,j})] \quad (2.11)$$

Thus, the problem has been reduced to finding  $q_{L,j}$  and  $q_{R,j}$ . The resulting formulae are complicated and are not reproduced here, but for a detailed analysis, see Equations 1.7 to 1.10 of Colella & Woodward (1984).

Once the left and right states are found for each cell, we need to compute the average of the fluxes over time. However, due to the discretization previously described, a discontinuity is generated and a Riemann problem has to be solved. A Riemann problem is a special case of Initial Value Problem (IVP), where the IC is a discontinuity between two different constant states, one left ( $\mathbf{U}_L$ ) and one right ( $\mathbf{U}_R$ ). Analytical solutions to such problems exist, but they would be too expensive in terms of computational resources. This is the reason why hydrodynamical codes use approximate Riemann solvers.

### 2.2.1 Riemann solvers

The Riemann problem to be solved has as solution a system of three waves propagating away from the initial discontinuity: the central contact discontinuity and two waves travelling one left and one right that could be either shocks or rarefaction fans. Four different combinations of the left and the right shocks and rarefactions are possible, but only one of these can be fully consistent with a chosen initial condition. Once determined the correct physical state, the problem can be solved

by resolution of an algebraic equation, thus using a series of approximate Riemann solvers. Four different Riemann solvers have been implemented in ENZO:

- Two-shock (Toro 1997);
- Harten-Lax-Van Leer (HLL, Toro (1997));
- Harten-Lax-Van Leer with a contact discontinuity (HLLC, Toro (1997) );
- Harten-Lax-Van Leer with multiple discontinuities (HLLD, Miyoshi & Kusano (2005)).

Two-shock is used only with the PPM method, and will be used in all the simulations performed in this work. HLL and HLLC are used with PPM, MUSCL (both with and without MHD) and MHD-CT. HLLD instead, is exclusively an MHD solver, and works with both the MUSCL and MHD-CT methods. The two-shock approximation is the assumption that both left and right waves are shocks, the HLL method instead requires no central contact discontinuity and computes the signal speed in the central region as an average over the two waves. HLLC modifies the previous method by including the third central wave in the computation. For the MHD case, four more waves need to be treated (increasing the total number to 7), but as HLL and HLLC can be modified in order to consider this increase, HLLD only accounts for two of the additional waves. While the fastest Riemann solver here described is HLL, it is also the most dissipative one, followed, in order, by two-shock and HLLD.

## 2.3 Structured Adaptive Mesh Refinement

ENZO is an Eulerian, magneto-hydrodynamic, Adaptive Mesh Refinement (AMR) code (Bryan et al. 2014). The code is multi-dimensional and parallelized using the MPI (Message Passing Interface) library. The AMR grid patches are its main data structure and each grid is solved as an independent computational fluid dynamic problem with boundary conditions stored in the ghost zones (a layer of cells surrounding the computational domain). The idea behind the Structured Adaptive Mesh Refinement is the overlap of rectangular patches at different resolutions.

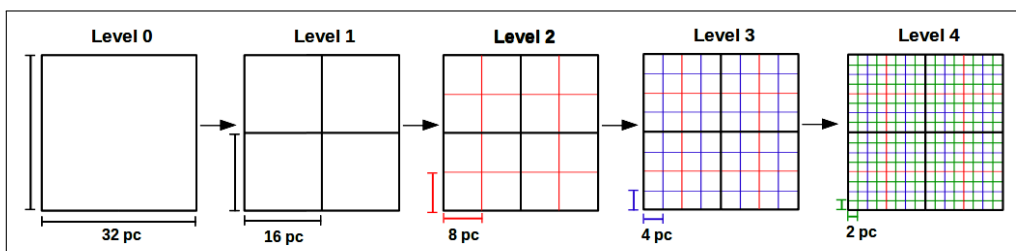


Figure 2.2: Refinement procedure for a cell at initial resolution  $32 \text{ pc} \times 32 \text{ pc}$ . Level 1 has 4 cells of  $16 \text{ pc} \times 16 \text{ pc}$  resolution (black line), level 2 has 16 cells of  $8 \text{ pc} \times 8 \text{ pc}$  (red), level 3 has 64 cells of  $4 \text{ pc} \times 4 \text{ pc}$  (blue) and level 4 contains 256 cells with size  $2 \text{ pc} \times 2 \text{ pc}$  (green).

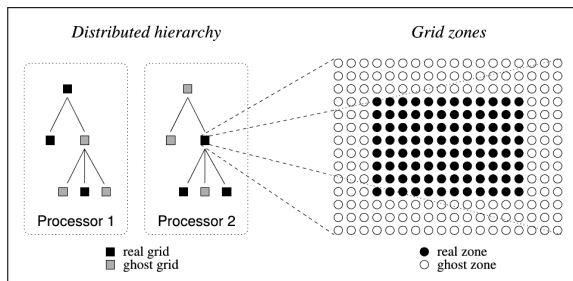


Figure 2.3: The left panel shows a simple 3-level hierarchy tree representation distributed on 2 processors. The right panel shows a grid cells distribution (Bryan et al. 2014).

The coarsest grid (also called *root* grid) covers the whole computational domain and its nodes identify the linking points for smaller grids at higher resolutions (see fig. 2.2). This mechanism can be iterated indefinitely and thus creates a tree of dependant grids. For each grid at given resolution, the parent grids are the grids at lower resolution, while the child grids are the grids at higher resolution. The grid at the lowest resolution can only be a parent grid, while the grid at the highest resolution can only be a child grid. All the grids at the same resolution belong to the same *level*; the higher the level, the higher the resolution. The ratio between the sizes of parents

and children is constant. The ratio between the sizes of parents

and child grids cells is called *refinement parameter* and here on it is referred to as  $r$ .

The enumeration in ENZO is 0-based, so that the first level, containing only the coarsest grid, is identified by the number 0 while the second one by 1, and so on. Fig. 2.2 shows a schematic representation of the overlap between grids at different levels in 2D (in the figure, at each level is associated a colour, note that the center of an inferior level's cell is the fixing point for a higher level one).

Every grid has a kernel of “*real*” cells surrounded by a layer of “*ghost*” cells (fig.2.3). The real cells are the ones in which the actual storage of all variables takes place. The ghost cells instead, are used as an interface between adjacent grids and/or parent and child grids. All the values stored in the ghost cells at every timestep are due to interpolations or are needed by the hydrodynamics solvers. Thus, they will not be considered in the analysis phase.

Fig. 2.3 shows an example of tree structure for a 2D AMR hierarchy, composed of 6 grids at three different levels (1 at level 0, 2 at level 1 and 3 at level 2). The left panel shows how real and ghost cells are distributed on different processors: on each processor a grid is a *real* grid if its data is allocated to that specific processor, and it is a *ghost* grid if its data is allocate an a different processor. Each grid then, is a real grid on exactly one processor, and a ghost one on all the others. Communication between processors for transfer of a mesh or of data is performed via MPI. The right panel shows the distribution of real and ghost cells over a single grid.

### Temporal Refinement

The only imposition upon the computation of the timestep is the satisfaction of the Courant-Friedrichs-Lewy (CFL) condition. This condition requires the timestep to be smaller than the sound-crossing time over a given cell so that, in the one-dimensional case:

$$\Delta t_x = \min \left( k_{\text{CFL}} \frac{\Delta x}{c_s + |v_x|} \right)_L \quad (2.12)$$

where  $k_{\text{CFL}}$  is usually referred to as the CFL-parameter and must be:  $0 < k_{\text{CFL}} \leq 1$ ,  $c_s$  is the sound speed and  $v_x$  the peculiar velocity on the x-direction. The  $\min(\dots)_L$  formalism means that this value is computed for each cell on a given level  $L$

and the minimum overall value is taken as the timestep. In the three-dimensional generalization, the total timestep is a harmonic average of the minimum timesteps on each direction:

$$\Delta t_{\text{CFL}} = \min \left( \frac{1}{1/\Delta t_x + 1/\Delta t_y + 1/\Delta t_z} \right)_L \quad (2.13)$$

Thus, given the linear dependence between the timestep and the size of a cell, in ENZO timesteps are evaluated on each level. As for the evolution of the solution, the hierarchy is advanced in a level-by-level basis on a W-cycle, as shown in fig. 2.4.

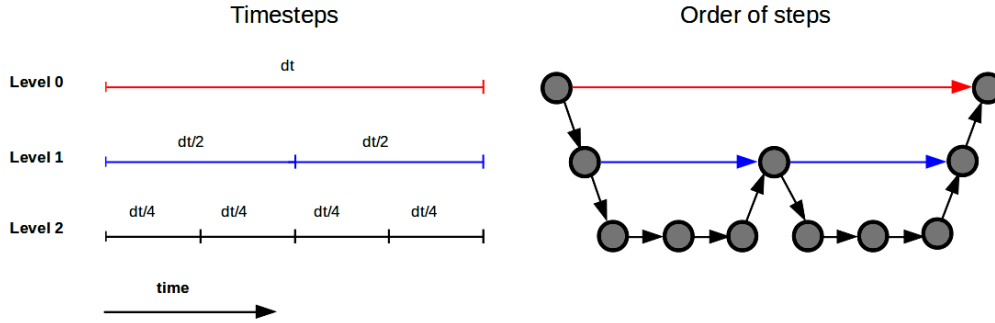


Figure 2.4: Left panel shows the proportionality between timesteps at different levels. Right panel shows the timestep evolution implementation in ENZO: a W-cycle (Adapted from Bryan et al. (2014)). In the figure, the ratio between two adjacent levels is 2, but there is no restriction on the proportionality of timesteps between different levels. We chose to use this ratio here for pure graphical convenience.

Once the timestep  $dt$  of the coarsest level has been fixed, the timestep of the levels at higher resolution will be  $dt/r^l$ , where  $r$  is the refinement parameter and  $l$  is the level number. Initially, the entirety of the grids belonging to the coarsest level  $l$  are advanced of a timestep  $dt$  (in fig. 2.4 indicated by the red line). Then all grids at level  $l + 1$  are advanced (blue line) and so on until the highest level is reached. The latter is advanced for as many timesteps,  $dt/r^{l_{\text{MAX}}}$ , needed in order to catch up with the solution at the level immediately above ( $l_{\text{MAX}} - 1$ ). After the synchronization of these two levels, the above one is advanced of a proper step, leading once again to the previous iteration. At the end of every timestep, the ghost zones of each grid are updated with data from neighboring sibling grids (if

any exist) and/or interpolated from a parent grid.

### Boundary conditions and AMR consistency

The boundary conditions are external to the computational domain both for the grid at the lowest level and for all the grids at highest levels located at the edges of the computational domain. Instead the boundary conditions are internal for siblings grids (child grids originated from the same parent grid). In both cases, the code allows four choices:

- Reflecting, every conserved variable stored in the ghost zones equals its value in the computational domain, except for velocity:  $v_x(-x) = -v_x(x)$ ;
- Outflow, the solution at the edge of the computational domain is duplicated ( $q(-x) = q(0)$ );
- Inflow, boundary values are fixed by a certain function:  $q(-x) = q_0(-x, t)$ ;
- Periodic, boundary solution is copied by the other side of the domain:  $q(-x) = q(x_{max} - x)$ .

In this work, the Outflow condition is always applied, because it guarantees the isolation of the cloud for the grids at the edges of the domain.

A refined region is simulated with at least two resolutions, thus a same volume has multiple solutions. In order to maintain consistency, the quantities of the coarser grids need to be updated with the finer values. This is done in the *projection step*, using a volume-weighted average of the conserved variables:

$$q^{coarse} = r^{-d} \sum_{i,j,k=1}^d q_{i,j,k}^{fine} \quad (2.14)$$

Where  $r$  is the refinement factor: the ratio of the widths of two adjacent levels' cells,  $d$  is the weight and it is the dimensionality, dimensionality  $-1$  and  $1$  for cell-centered, face-centered and node-centered quantities respectively. The sum is done over all the finer cells covering a coarse one along each direction. The projection step perturbs the Flux-conservative properties of the code (preferred in order to maintain conserved quantities at machine resolution) since, at the boundary of a

refined region, both coarse and fine cells are updated with different estimates of the flux across the boundary (from coarse grid evolution and from the fine grid average solution). Flux conservation is then restored in the *Flux correction step* by correcting all the coarse cells lying outside the boundary of a fine region with the difference between the fine and coarse estimates for the fluxes across the boundary, and precisely:

$$q^{coarse} = \tilde{q}^{coarse} - \Delta t \left( \mathbf{F}^{coarse} - \sum_{j,k=1}^d q_{j,k}^{fine} \right). \quad (2.15)$$

Here,  $\mathbf{F}^{coarse}$  is the Flux of the quantity  $q_i$  across the  $i$ -direction,  $\tilde{q}^{coarse}$  is the uncorrected quantity in the coarse cell and the sum is over the  $r^{d-1}$  fine cells in the perpendicular directions sharing a face with the coarse cell. As afore mentioned, the solution of Euler equations on a multi-resolution, multi-grid setup is achieved by solving the same equations on each grid separately. The convergence of different levels' solutions is imposed in the *projection* and *Flux correction* steps here explained.

### 2.3.1 Refinement Criteria

The revolutionary feature in ENZO is its automated refinement. The three main parameters regulating the refinement in ENZO are `RefineBy`, `CellFlagginMethod` and `MaximumRefinementLevel`. `RefineBy` is the refinement factor  $r$ . As per definition of  $r$ , from a coarser cell, a number of  $r^d$  cells are obtained with a resolution  $r$ -times larger, where  $\mathbf{d}$  is the dimensionality of the problem. In general, this parameter must be an integer and, for most simulations, is set to 2, so that for a 2-D setup a refined cell produces 4 cells, each one at double resolution (half size) with respect to the parent one (fig. 2.2). `MaximumRefinementLevel` sets the maximum level at which grids can be created, while `CellFlagginMethod` identifies the criterion to be used for the refinement.

There are 13 different criteria for refinement: each criterion corresponds to an integer number. In this Thesis, we investigated three of these criteria (tab. 2.1). In the following, a review of the adopted criteria is reported, but for more details, please refer to Bryan et al. (2014).

CellFlaggingMethod	Description
1	<i>Refine by Slope</i>
2	<i>Refine by Baryon Mass</i>
15	<i>Refine by SecondDerivative</i>

Table 2.1: Four principal parameters used in this study.

## Slope

The *Refine By slope* criterion analyzes the normalized slope of a given thermodynamical variable on adjacent cells. If this slope is greater than a specified value, then the cells will be flagged and refined.

By indicating with  $\mathbf{q}$  the chosen field and with the index  $i$  the cell's position, the slope  $\mathbf{s}$  is defined as:

$$s = \frac{q_{i+1} + q_{i-1}}{2q_i} \quad (2.16)$$

This refinement criterion is regulated by two parameters: `SlopeFlaggingFields` and `MinimumSlopeForRefinement`. The first one identifies the correct field to be considered while the second one specifies the  $\mathbf{s}$  value above which a cell must be flagged.

## Baryon Mass

*Refine by Baryon Mass* (here on called *over-density* criterion) is a criterion designed to mimic a Lagrangian method, meaning that it tries to keep a fixed mass resolution. A certain cell is refined if the baryonic mass contained within it is larger than an upper limit value. The condition for refinement is:

$$M_g > \rho_{flag} (\Delta x_{root})^d r^{\epsilon_l} \quad (2.17)$$

where  $M_g = \rho(\Delta x)^d$ , is the mass within each cell,  $\rho$  the density,  $\Delta x$  its size,  $d$  the dimension of the problem and  $\Delta x_{root}$  the size of the root grid's cell. It takes into account the increase in density for each level (here indicated by the letter  $l$ ). The quantity  $\rho_{flag}$  is essentially the density that each level cell must have in order to be flagged and then refined: this value is the product between the limit

density of the root grid ( $\rho_0$ ) and the factor  $r^{d*l}$ . Therefore, the limit density of each level increases with the order of the level, so that the last level has highest spatial resolution and higher values of density. In the code,  $\rho_0$  is identified by the parameter `MinimumOverDensityForRefinement`. Formula 2.17 can thus be rewritten in a much more explicit way:

$$M_g > \rho_0(\Delta x_{root})^{d_r l^{*(d+\epsilon_l)}}. \quad (2.18)$$

Here  $\epsilon_l$  is a parameter that can modify the “aggressiveness” of the refinement by assuming any real number. In the code it is identified by the parameter `MinimumMassForRefinementLevelExponent`. Setting it to negative the refinement will be super-Lagrangian, so that each level has less gas mass per cell on average than the coarser level above it. Setting it positive will lead to a sub-Lagrangian behaviour, meaning that the refinement will be less aggressive than the Lagrangian case. By default this parameter is set to 0 but it can assume any real value. In particular, in the following it has been used to shrink the density limit interval between two subsequent levels. Let us consider a 2D, 3 level hierarchy dataset refined using the over-density criterion and a refinement factor  $r = 2$ . Adopting a default value of 5 (in code units) for the `OverDensity` parameter, implies that a 0 level cell is refined when the density reaches a value larger than 5. If  $\epsilon_l = 0$ , (default value) the next refinement is obtained, on a level 1 cell, at a density threshold equal to  $OD_1 = 5 * 2^{d*(l=1)} = 20$ , and again on level 2 the threshold moves to  $OD_2 = 5 * 2^{d*(l=2)} = 80$ . The ratio between the highest and lowest density values is then:  $OD_2/OD_0 = 16$ . Instead, if  $\epsilon_l$  is a negative value, such as  $-1$ ,  $OD_1 = 5 * 2^{l(d+\epsilon_l)} = 5 * 2 = 10$  and  $OD_2 = 5 * 2^{2(2-1)} = 5 * 4 = 20$ . The density ratio between highest and lowest levels is now:  $OD_2/OD_0 = 4$ . Using this new setup, all densities above 20 will have the highest level spatial resolution.

## Second Derivative

The last criterion of refinement that we used, *Refine by SecondDerivative*, is based upon the evaluation of a normalized second derivative of a given field on each cell. We present here the reference formula, but for an exhaustive treatment we recommend the reading of Löhner et al. (1987) and in particular, the documentation of FLASH4<sup>2</sup>. The main idea behind this criterion is that if the normalized second derivative of a certain field, is greater than a specified treshold in a certain cell, then that cell must be flagged and refined. The treshold in 2D is defined as follows:

$$S = \left\{ \frac{\sum_{ij} \left( \frac{\partial^2 f}{\partial x_i \partial x_j} \right)^2}{\sum_{ij} \left[ \frac{1}{2\Delta x_j} \left( \left| \frac{\partial f}{\partial x_i} \right|_{x_i - \Delta x_i} + \left| \frac{\partial f}{\partial x_i} \right|_{x_i + \Delta x_i} \right) + \epsilon \frac{|f_{ij}|}{\Delta x_i \Delta x_j} \right]^2} \right\}^{1/2} \quad (2.19)$$

Where  $f$  is the field (Density, Total Energy, x-velocity, y-velocity...), selected in the code by defining the parameter `SecondDerivativeFlaggingFields` and  $|f_{ij}|$  is an average of  $f$  over adjacent cells in all directions (i and j in 2D). The term  $\epsilon$  provides a method of ignoring small fluctuations and is set by default to  $10^{-2}$ . The larger is this number, the more relevant are the fluctuations from the spatial average. In the code, this value is identified by the parameter `SecondDerivativeEpsilon`.  $S$  is the appointed treshold and can vary in the interval  $[0, 1]$ , usually a value between 0.3 and 0.8 is recommended; in the code, the associated parameter is `MinimumSecondDerivativeForRefinement`.

## 2.4 Modifications to ENZO

In order to reproduce with ENZO the same simulations performed by Marinacci et al. (2010) and Armillotta et al. (2016), we need to adopt the same assumptions of these authors. In particular, we must use the same cooling function, taken from Sutherland & Dopita (1993).

---

<sup>2</sup> [http://flash.uchicago.edu/site/flashcode/user\\_support/flash4\\_ug/](http://flash.uchicago.edu/site/flashcode/user_support/flash4_ug/)

### 2.4.1 Radiative cooling

In our work, we have included the possibility for the gas to radiate, thus losing internal energy via radiative cooling. This is done by the introduction of an energy loss term in the Energy conservation equation, so that equation 2.1c becomes:

$$\frac{\partial e}{\partial t} + \nabla \cdot [(e + P)\mathbf{u}] = -\rho^2 \Lambda(T, Z) \quad (2.20)$$

Where  $\Lambda$  is the energy lost by the gas via radiative cooling normalized to the square of the total gas density ( $[\text{erg cm}^3 \text{ s}^{-1}]$ ) and  $\rho\Lambda$  is the energy loss rate, per unit volume, due to radiative cooling. The cooling rates adopted, are computed under the assumption of Collisional Ionization Equilibrium (CIE), so they do not depend on the hydrogen number density  $n_{\text{H}}$ . They however do depend on temperature and metallicity.

In ENZO, cooling rates can be calculated using different methods. We decided to use the algorithm that reads the cooling rate values from a lookup table. By default, ENZO uses the Temperature dependant cooling function derived by Sarazin & White (1987), but in order to compare our simulations with previous works, we adopted the cooling function described in Sutherland & Dopita (1993). However, while Armillotta et al. (2016) studied a multi-metallicity case of the problem, we considered gas at metallicity  $[Fe/H] = -0.5$ . The cooling function for this case is shown in fig. 2.5. The temperature interval ranges between  $10^4 \text{ K}$  and  $10^{8.5} \text{ K} \simeq 3 \times 10^8 \text{ K}$ .

The peak at  $T = 15.000 \text{ K}$  is due to collisional recombination of H, while the double peak at temperatures  $10^4 \text{ K} < T < 10^5 \text{ K}$  is primarily due to recombination of He and to forbidden lines of highly ionized metals (OVII, OVIII, CIV, CV, NIV, NV...). At  $T \sim 10^6 \text{ K}$  recombinations of other highly ionized elements contribute to the cooling rates, such as NeVI–NeIX, FeXII–FeXX, SiVIII–SiX... At temperatures  $T > 10^7 \text{ K}$  the only state a gas can be found is in full ionization, meaning that electrons and ions can only interact via free-free transitions. Thus, the fully ionized regime is governed by Bremsstrahlung emissivity.

The strong dependence of the cooling function on the temperature leads to the necessity of computing, at each timestep, the temperature of each fluid element, in order to obtain the corresponding cooling rate. The evolution of temperature

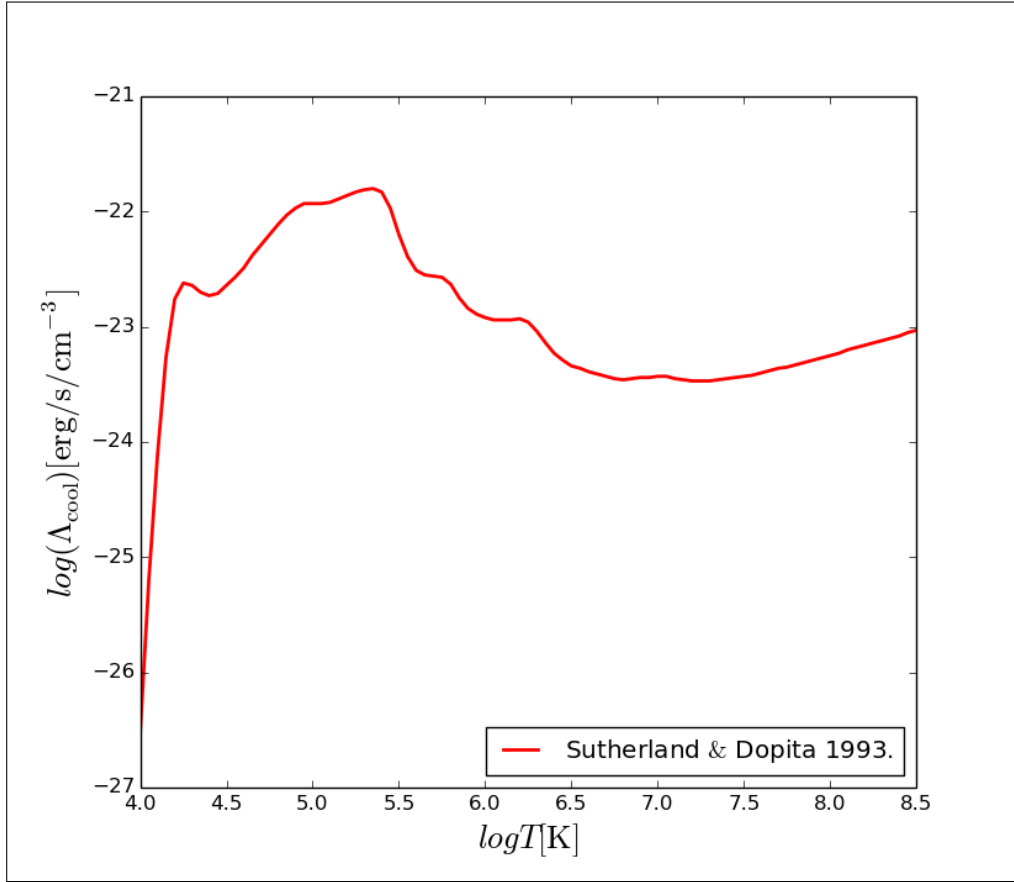


Figure 2.5: Cooling function at  $[\text{Fe}/\text{H}] = -0.5$ , obtained by Sutherland & Dopita (1993)

as a function of mean molecular weight and metallicity is based upon the solution of equation (2.9) rearranged as:

$$\frac{P}{\rho} - \frac{kT}{\mu(T, Z)} = 0 \quad (2.21)$$

where  $k$  is the Boltzmann constant,  $Z$  the metallicity and  $\mu$  is the mean molecular weight. The mean molecular weight is a function of temperature, and it is interpolated on the same table containing the cooling rates, via an iterative method: the secant method.

The cooling rates tabulated in Sutherland & Dopita (1993), that we call  $\Lambda_{\text{SD}}$ , are normalized by the product  $n_t n_e$ , where  $n_t = \sum_i^{\text{ions}} n_i$  is the total number density of ions and  $n_e$  is the number density of electrons. However, in our simulations, only

the total number density of the gas is known, so we need to rearrange this parameter in a way that it is normalized to the total number density:  $N = (n_t + n_e)$ . In order to do so, a simple algebraic manipulation is performed, obtaining:

$$\Lambda = \Lambda_{\text{SD}} \frac{n_t n_e}{(n_t + n_e)^2 \mu^2} \quad (2.22)$$

All these rates are tabulated and read by the code at every timestep. Furthermore, when the computed temperature does not coincide with any of the tabulated values, but is included in a temperature interval between two of them, a linear interpolation (in logarithmic base) is performed in order to get an approximated cooling rate. The density decomposition of the logarithmic temperature interval  $4.0 < \log T < 8.5$ , in 93 uniformly distributed points, defines a constant interval of uncertainty  $\Delta \log T = 0.05$ . The variation of the logarithmic cooling rates is shallow enough to allow a good approximation in this interval.



# Chapter 3

## Adiabatic simulations of fountain clouds

This chapter is devoted to the study of the interaction between galactic fountain clouds and the hot corona when no radiative cooling is permitted. In particular, section 3.1 contains all information regarding the initial setup of simulations while sections 3.2 and 3.3 show the results obtained when AMR is turned off and on respectively. All simulations presented here are carried out with the ENZO code.

### 3.1 Setup of the simulations

The study of the galactic fountain phenomenon is here performed following previous works by Marinacci et al. (2010) and Armillotta et al. (2016). The overall setup of the prototype simulation is that of a spherical, cold ( $\sim 1 \times 10^4$  K) gas cloud of 100 pc radius moving along the x-axis with a velocity of 75 km/s. This is the estimated velocity at which a cloud should be ejected from the disc in order to reach heights of a few kiloparsecs. In this chapter we study the motion of the cloud when no radiative cooling is considered. A complete model of the motion of a fountain cloud through the corona, should take into account its interaction with the gravitational potential of the galactic disc. A ballistic trajectory is expected, where the ejected cloud orbits over the disc and falls back onto it in  $\sim 100$  Myrs (Fraternali & Binney 2006). However, in these simulations we neglect the gravi-

tational acceleration. This is justified because, during their orbits, the clouds do not change significantly their distance from the galactic disc, reaching at most heights of a few kpc. Also, their distances from the Galaxy center vary by less than 30% (Fraternali & Binney 2006; Marasco et al. 2012). Furthermore, if the corona is in hydrostatic equilibrium with the gravitational potential, the coronal density is not expected to vary much and we can neglect its variation along the clouds trajectories. We chose a radius of 100 pc because this is the typical radius for a cloud in order to survive evaporation (due to ablation from the coronal gas and mixing between the two fluids) long enough to fall back onto the disc (Marnacci et al. 2010). Also, this radius produces similar masses as those observed by Wakker et al. (2008) for Intermediate Velocity Clouds (IVCs).

The total particle density of the corona is set to  $n = 10^{-3} \text{ cm}^{-3}$  and assuming pressure equilibrium between the cloud and the coronal gas, a density of  $2 \times 10^{-1} \text{ cm}^{-3}$  is found for the cloud. This value for coronal density implies  $n_e \simeq 0.5 \times 10^{-3} \text{ cm}^{-3}$ , that is lower than the density  $n_e \simeq 2.6 \times 10^{-3} \text{ cm}^{-3}$  found in Fukugita & Peebles (2006) at  $r = 10 \text{ kpc}$  for a very massive corona but it is comparable to  $n = 4 \times 10^{-4} \text{ cm}^{-3}$  at  $r = 10 \text{ kpc}$  above the plane adopted by Heitsch & Putman (2009). In order to smooth the density gradient at the cloud-corona interface, an annulus of 10 pc width is introduced around the cloud, where the density decreases exponentially. This annulus allows the density transition from the high value at the interior of the cloud to the rarefied values of the coronal gas, and its spatial width is indicated by the parameter  $\Delta = 10 \text{ pc}$ . The coronal temperature is fixed at  $2 \times 10^6 \text{ K}$ , as estimated observationally by Miller & Bregman (2015), while the cloud temperature is initially set to  $10^4 \text{ K}$ . We analysed the evolution of gas at temperatures below  $T = 2 \times 10^4 \text{ K}$  as a tracer for H I<sup>1</sup>. Given the high temperatures, the coronal gas is fully ionized, while the cold gas cloud is assumed completely neutral.

---

<sup>1</sup>Assuming Collisional Ionization Equilibrium (CIE), the gas at temperatures below  $2 \times 10^4 \text{ K}$  should be less than 50% ionized.

	Cloud	Corona
Temperature [ K]	$1 \times 10^4$	$2 \times 10^6$
Density [ $\text{cm}^{-3}$ ]	$2 \times 10^{-1\dagger}$	$1 \times 10^{-3}$
X Velocity [ km/s]	75	0
Y velocity [ km/s]	0	0
Atomic weight*	2.069	0.998

† This value has been obtained by assuming pressure equilibrium and specifying coronal density and temperature and cloud temperature:  $n_c = \frac{T_h}{T_c} n_h$ .

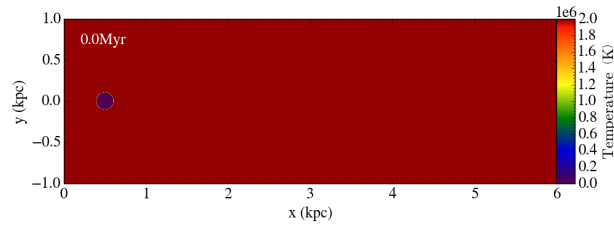
\* The Atomic weight is multiplied by the factor  $\frac{m_H}{10^{-24}} = 1.67$ , where  $m_H$  is the hydrogen mass.

Table 3.1: Initialization of the parameters for the implementation of the galactic fountain simulation.

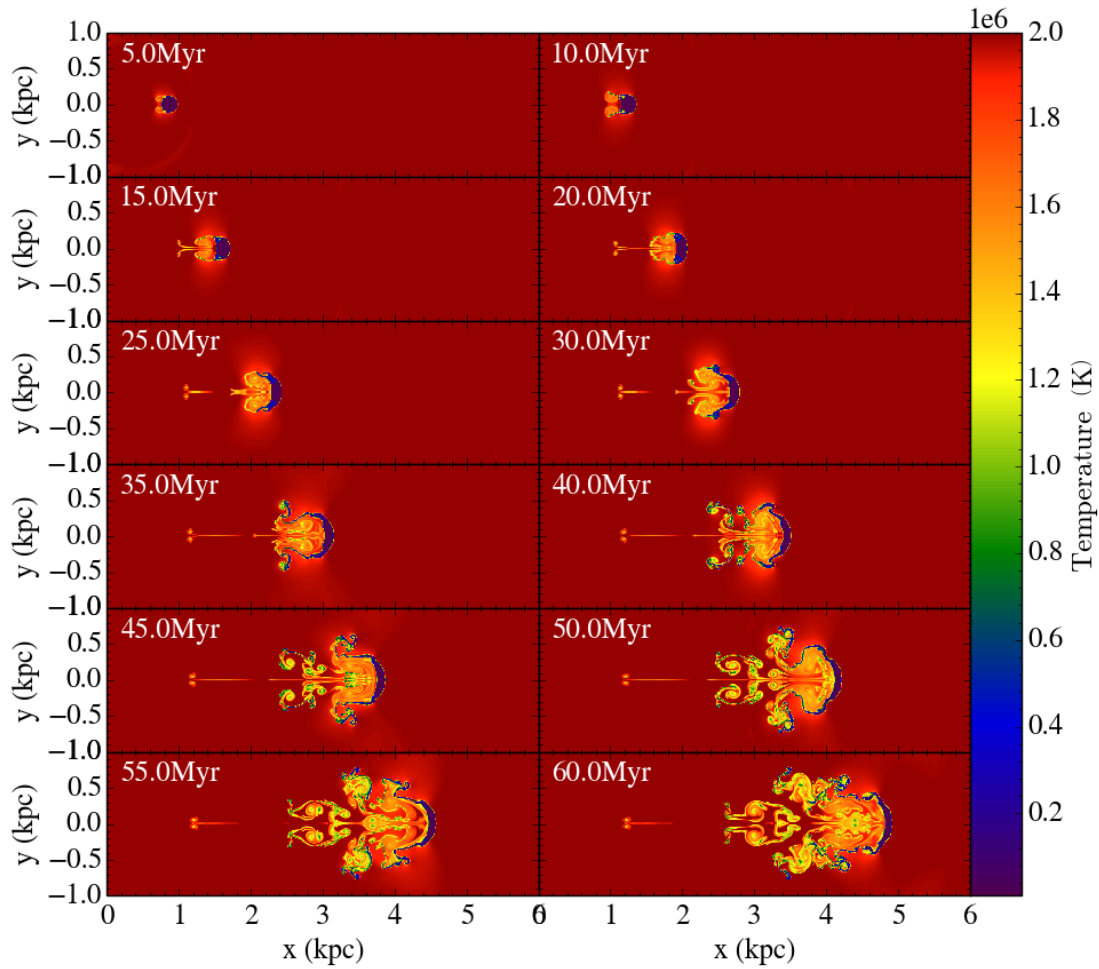
## 3.2 Non-AMR implementation

Starting from Marinacci et al. (2010), a number of simulations of galactic fountain’s clouds have been performed over the last few years. The main goal has been the estimation of the amount of hot gas accreted through the interaction between the cloud and the corona, and the identification of a constraint on gas accretion in Milky Way-type galaxies. The main follow-up of such studies is the work by Armillotta et al. (2016), where thermal conduction is taken into account together with radiative cooling. However, the greatest limitation of the previous analysis is that only 2D simulations have been performed. This was due to the fixed-grid that made the extension to a 3D geometry prohibitive. In particular the fixed-grid codes: ECHO++ (Marinacci et al. 2010) and ATHENA (Armillotta et al. 2016) have been used. Thus, an AMR implementation of the problem is required in order to speed up the computation and open to the possibility of performing 3D simulations of the problem.

In order to estimate the main differences with the other codes, we first performed fixed-grid simulations of the galactic fountain model, using ENZO. The first step of our investigation is to estimate the differences between the codes when radiative cooling is switched off and ENZO is treated as a fixed-grid code. Once an agreement with ATHENA is found in this case, then the same setup is used in the AMR simulations.



(a)



(b)

Figure 3.1: Initial setup of the temperature distribution in our adiabatic simulation with ENZO fixed-grid ( $4 \text{ pc} \times 4 \text{ pc}$ ): the AMR is switched off. b) The temporal evolution of the cloud is shown with temperature snapshots at different times (upper left corners).

Not including radiative cooling in ENZO, the interaction between the cloud and the coronal gas is uniquely the Kelvin - Helmholtz (KH) instability generated on the interface between the two gases. The cloud, during its motion, is progressively flattened perpendicularly to its motion by ram pressure, meanwhile its outer layers get detached from the main body, forming a wake of turbulent gas in the opposite direction to the cloud's trajectory. The wake is the locus of mixing between the two gases. Here, the creation of vortexes magnifies the contact surface between hot and cold gas, enhancing the efficiency of mixing. The main effect of the lacking of a radiative cooling function is the heating up of the cold material, so that the cloud is constantly deprived of its constituents and faces a gradual evaporation. Temperature snapshots of the system at fixed timesteps are presented in figure 3.1b. A perfect horizontal symmetry can be seen as well as the turbulent structure of the wake. The head of the cloud is not completely disrupted, suggesting that the time for complete evaporation could be much longer.

The temperature threshold for gas is  $T = 2 \times 10^4$  K, only gas temperatures below this value are considered. All simulations are performed in a 2D geometry, by suppression of the dimension perpendicular to the cloud velocity. This overall setup implies that the cloud is indeed an infinite cylinder, travelling perpendicularly to its long axis, with initial circular cross-section radius  $R_{cl} = 100$  pc. The masses obtained with these simulations are therefore quantities per unit length of the cylinder. In order to relate these to the masses relative to an initially spherical cloud of radius  $R_{cl}$ , we need to multiply them by the length  $4R_{cl}/3$  within which the mass of the cylinder equals that of the spherical cloud.

The cold gas mass is obtained by summing mass densities over all cells satisfying the condition  $T_{i,j} < 2 \times 10^4$  K, where subscripts "i" and "j" indicate the cell's position in the domain. This sum is then multiplied by the geometry correcting factor, obtaining equation 3.1:

$$M = \frac{4}{3} R_{cl} \sum_{i=1}^m \sum_{j=1}^n \rho_{i,j} (T < 2 \times 10^4 \text{ K}) A_{i,j} \quad (3.1)$$

The mass - weighted velocity of the cold gas is instead calculated as follows:

$$\langle v \rangle = \frac{\sum_{i=1}^{N_x} \sum_{j=1}^{N_y} \rho_{i,j}(T < 2 \times 10^4 \text{ K}) v_{i,j}(T < 2 \times 10^4 \text{ K})}{\sum_{i=1}^{N_x} \sum_{j=1}^{N_y} \rho_{i,j}(T < 2 \times 10^4 \text{ K})} \quad (3.2)$$

Here,  $N_x$  and  $N_y$  correspond to the numbers of cells on the x and y directions of the domain respectively. As a preliminary analysis, a comparison between the two codes not using AMR on ENZO has been performed. The, constant in time, resolution is everywhere in the domain fixed at  $4 \text{ pc} \times 4 \text{ pc}$  (as shown in figures 3.1). After the analysis, a temporal evolution curve for cold gas mass and mean velocity is obtained, as shown in fig: 3.2. Here the red curve with triangles is the one obtained with ENZO, while the green one with squares, with ATHENA.

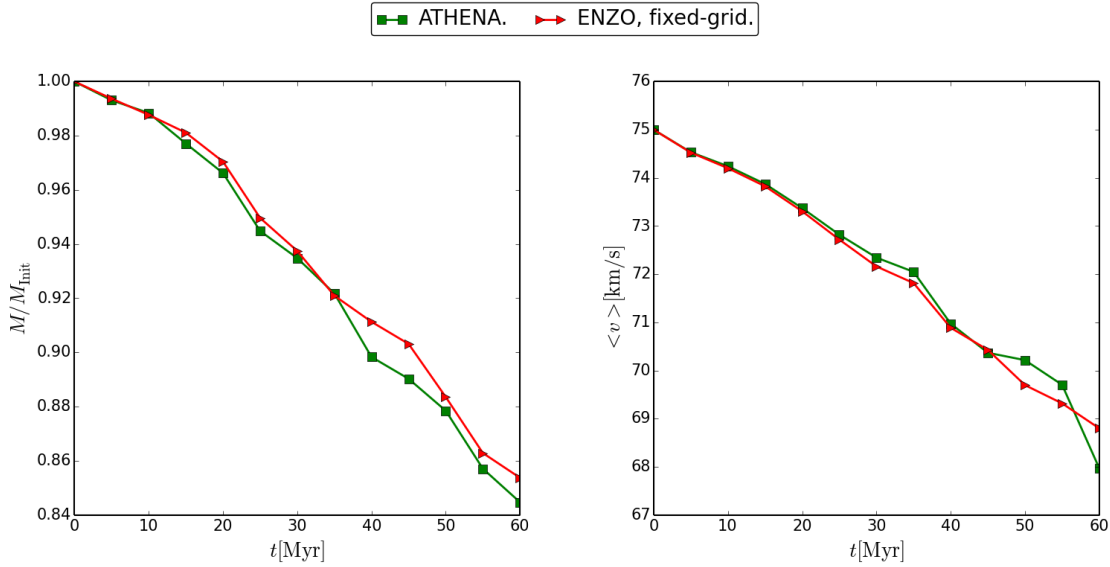


Figure 3.2: Cold gas mass and mean velocity temporal evolutions. The red curve with triangles is obtained with ENZO, the green one with squares, with ATHENA.  $M_{\text{Init}}$  is the cold gas initial mass.

From fig. 3.2 (left panel) we can obtain a first, rough estimate of the amount of evaporated mass. The initial cold ( $T < 2 \times 10^4 \text{ K}$ ) gas mass is  $M_{\text{Init}} = 2.32 \times 10^4 M_{\odot}$ , while at the end of the evolution it has been reduced to  $1.98 \times 10^4 M_{\odot}$ , thus a 15% decrease. In an initial phase, lasting up to 10 Myrs, the simulations performed with ENZO and ATHENA behave exactly in the same way, due to the fact that the instability has not yet developed. Later on, as the wake gets more and more extended and the gas state more and more turbulent, the cold gas mass

estimated by ENZO is slightly higher with respect to ATHENA. As shown in fig. 3.2 (left), this trend is more or less maintained over the whole evolution, up to 60 Myrs from the beginning. However the discrepancy between the two results, at 60 Myrs, is less than 1% over the initial mass and not much higher at 40 and 45 Myrs where it reaches a maximum. As for the velocity, the two behaviours are alike over the whole simulation time, except for the last point, where a 1.3% divergence can be estimated. The conclusion of this initial analysis is that there is an overall convergence for adiabatic simulations between the two codes if ENZO is used as fixed grid (no AMR).

### 3.3 Introduction of the AMR

In this section we are going to explain how the introduction of AMR changes the above results. The computational domain is initially divided into  $150 \times 50$  cells with resolution  $40 \text{ pc} \times 40 \text{ pc}$ . We initially studied the behaviour of ENZO when the over-density criterion (see section 2.3.1) is used for refinement, allowing for a high resolution to be reached in the most refined cells of  $2.5 \text{ pc} \times 2.5 \text{ pc}$ . Once a set of appropriate values is found for this criterion, in order to speed up the computation, we decrease the resolution of the most refined cells to  $4 \text{ pc} \times 4 \text{ pc}$  (section 3.3.2). In section 3.3.4 we discuss the necessity of a different initialization of the problem and we conclude by comparing the results obtained with different refinement criteria.

#### 3.3.1 Over-density refining criterion

We considered the most used criterion for refinement (Regan et al. 2007; Iaconi et al. 2016; Luo et al. 2016; Kim et al. 2016) and looked for an agreement with non-AMR data. The mentioned criterion is the *Refinement By Barion Mass* (see chapter 2.3.1 for an accurate description), here on referred to as over-density. In particular, by leaving the parameter `MinimumMassForRefinementLevelExponent` to the default value of 0, a convergence of the results to a common value is requested for different values of the parameter `MinimumOverDensityForRefinement`, in order to identify the best suited to the problem. We set the lowest resolution to  $40 \text{ pc} \times$

40 pc, the highest level to 4 and the refinement factor to 2 (for a detailed description of these parameters see chapter 2) and we performed 4 different simulations by simply varying this density treshold. Given this setup, the highest resolution reached is  $40 \text{ pc}/2^4 = 2.5 \text{ pc}$  in the densest regions, while resolutions in levels 1, 2, and 3 are respectively:  $20 \text{ pc} \times 20 \text{ pc}$ ,  $10 \text{ pc} \times 10 \text{ pc}$  and  $5 \text{ pc} \times 5 \text{ pc}$ . The purpose of this initial phase is to understand if a treshold in density exists that can guarantee convergence. In tab 3.2 we show, for each initial overdensity for refinement, the obtained densities relative to every level of refinement, computed by replacing appropriate values into equation 2.18 (using the default value for  $\epsilon_l = 0$ ).

$\rho_{min}$	8.350	0.418	0.167	0.017
Lev 1	33.4	1.672	0.668	0.069
Lev 2	133.6	6.688	2.672	0.267
Lev 3	533.4	26.752	10.688	1.07
Lev 4	2137.6	107.008	42.752	34.28

Densities are in  $10^{-26} \text{ g/cm}^3$ .

Table 3.2: Adopted values for Minimum over-densities and density tresholds at each level.  $\rho_{min}$  is the density treshold of level 0 grids in physical units. From left to righth, they correspond to the over-densities  $OD = 5, 0.25, 0.1$  and  $0.01$ , whose gas temperature distributions are shown in fig. 3.3.

The main goal in this first step is to identify the appropriate set of parameters that properly resolve the wake of the cloud, during its whole evolution. The region including the wake is the most important one in order to study the interaction between the two fluids. Here, the development of a turbulent regime and the creation of vortexes enhance the efficiency of mixing (as seen in fig. 3.1). In order to maintain the advantage of an AMR code with respect to a fixed-grid, an appropriate setting of refinement criteria and corresponding parameters has to be done. If a criterion is verified at different levels in a large portion of the domain, that whole portion is refined and the computational advantage of using an AMR code would be negligible. In fig. 3.3 temperature snapshots at time 60 Myrs are shown for the different choices of the `MinimumOverDensityForRefinement` (here on, over-density) parameter. On top of the temperature maps the grids computed

by ENZO are outlined, in gray scale: a darker gray implies a higher level, thus a region computed at higher resolution.

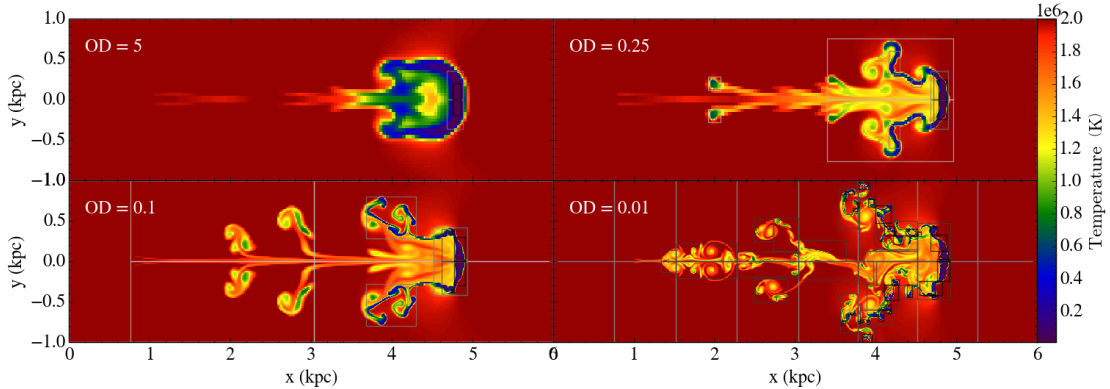


Figure 3.3: Temperature snapshots of the cloud in its final stage after 60 Myrs, for 4 different cases of initial overdensity (shown in the upper left of each panel). The morphology of the wake is heavily dependant on this parameter.

The top left panel of figure 3.3 shows a grid distribution limited to the densest region of the cloud, when the over-density parameter is set to 5. With this distribution the wake and the coronal gas are left at resolution  $40 \text{ pc} \times 40 \text{ pc}$ , with dramatic consequences for the evolution of the system. Furthermore, the value here adopted is suggested on ENZO’s online documentation<sup>2</sup> and on the reference paper (Bryan et al. 2014). The situation changes when we decrease the over-density parameter: for a value of 0.25 (top right panel) not only the cloud itself, but also part of the wake is included in the first refinement grid; however this grid is only resolved at  $20 \text{ pc} \times 20 \text{ pc}$ . A further decrease in the over-density parameter leads to a better inclusion of the wake. If the over-density parameter is set to 0.1, the whole wake is well included in a  $20 \text{ pc}$  resolution grid, while vortexes at  $\sim 4 \text{ kpc}$  are resolved at  $10 \text{ pc}$ .

The last simulation that we present has been carried out by setting the over-density parameter to a fine-tuned very low value. This value has been determined in a backward way: by assuming an overdensity  $3.328 \times 10^{-26} \text{ g/cm}^3$  to be resolved with a  $2.5 \text{ pc} \times 2.5 \text{ pc}$  resolution grid and dividing by the factor  $2^{d \cdot l} = 2^{2 \cdot 4} = 256$ , where  $l$  and  $d$  are the level and the dimensionality of the problem respectively. The

<sup>2</sup><http://enzo.readthedocs.io/en/latest/parameters/hierarchy.html>

grid refinement is far more extended over the whole domain, covering it with grids at much higher resolutions than in the previous cases. The simulation's domain is indeed all resolved at  $10 \text{ pc} \times 10 \text{ pc}$  resolution, while for exceeding values of density, levels 3 and 4 are created (reaching resolutions  $5 \text{ pc} \times 5 \text{ pc}$  and  $2.5 \text{ pc} \times 2.5 \text{ pc}$  respectively). Even if this coverage assures a good resolution for the cloud's evolution, it partially neutralizes the advantages of working with an AMR code, because the increase in resolution implies an increase in the overall number of cells, and consequently in computational time. In this case the computational time is almost 2 h on 4 CPUs while for the previous simulations it was of a few minutes. As for the fixed-grid simulation at resolution  $4 \text{ pc} \times 4 \text{ pc}$ , the computational time needed on the same architecture is  $\sim 8\text{h}$ .

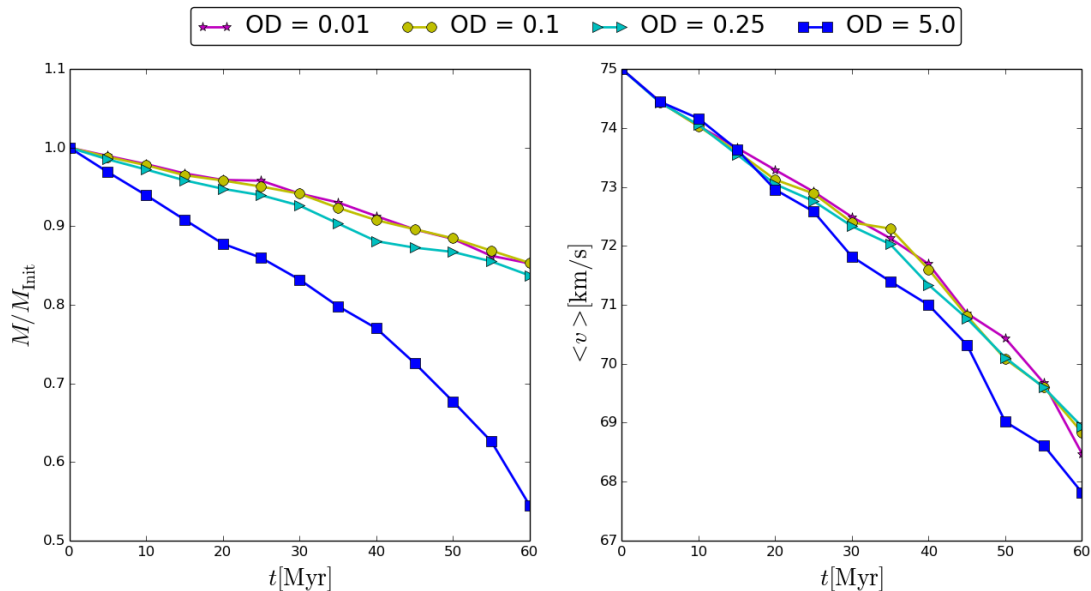


Figure 3.4: Cold gas mass and mean velocity of the cold ( $T < 2 \times 10^4 \text{ K}$ ) gas as a function of time obtained with ENZO using AMR for different values of the over-density parameter.

The trends of the cold gas mass and velocity, shown in fig. 3.4, are self-explanatory. As expected, the most divergent result is the one obtained by setting the over-density parameter to 5. Here the temporal curve is completely different from the others. In this case, the result is biased by the dominant effect of nu-

merical diffusion. In the Eulerian theory a cell must be big enough to represent a statistically significant amount of gas with overall similar properties. The implication of this consideration is that gradients in fluid’s properties must be resolved with an appropriate amount of adjacent cells, because each cell cannot represent two states of the gas at the same time. Equivalently, any significative substructure must be resolved by an appropriate number of adjacent cells. When this does not happen, so that a single cell is overposed to a gradient or a substructure, the physical quantity stored in the cell does not return a realistic value for the underlying gas, but a spatial mean instead. Furthermore, by testing this criterion with intermediate values between 5 and 0.01, we found that an overall convergence is found if the over-density parameter is below 0.12. Despite this “statistical” evidence, figure 3.3 shows how the structures formed using different over-density parameters clearly have different morphologies.

Figure 3.5 shows a zoomed region of the wake, first resolved at  $2.5 \text{ pc} \times 2.5 \text{ pc}$  (left) and then at  $40 \text{ pc} \times 40 \text{ pc}$ . The distribution of cold gas is greatly different in the two cases. All the substructures in the highly resolved case are not distinguishable at low resolution. This difference has the effect of dramatically smoothing the gradients in the gas properties and potentially invalidate the final results. Numerical diffusion is typical of eulerian codes and of course is not completely avoidable, due to the limited cell’s size definition of this type of codes. For static grid codes, the maximum resolution is reached everywhere in the domain, so that only gradients on smaller scales will not be resolved. For AMR codes instead, there is a much higher risk of numerical diffusion at every level if the refinement criterion performance is not well monitored. This is exactly what happens when, in this problem case, the over-density parameter is set to 5. Here, numerical diffusion is dominant (fig. 3.3 top left panel), leading to a massive overestimation of evaporation of the cloud gas (fig. 3.4, blue line with squares).

The problem of numerical diffusion can be limited by increasing the resolution, thus resolving structures with a sufficient number of cells.

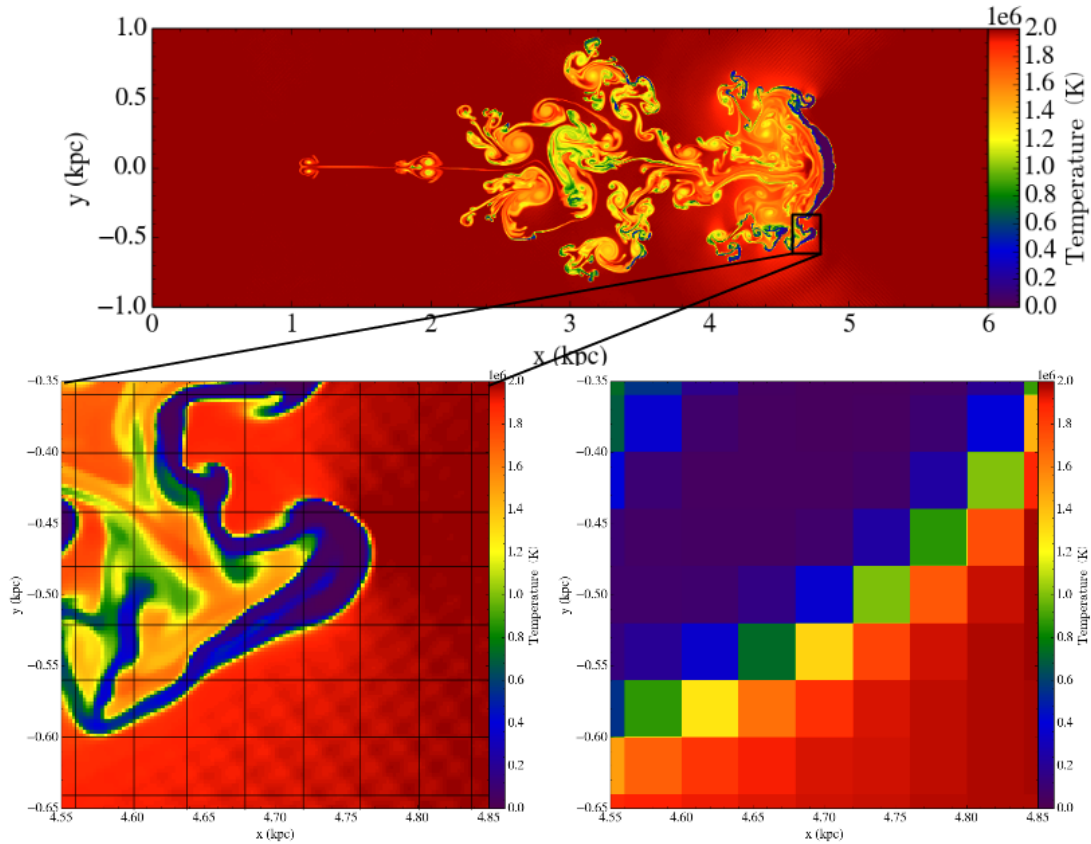


Figure 3.5: Zooming over a typical structure in the  $2.5 \text{ pc} \times 2.5 \text{ pc}$  fixed resolution simulation with ENZO. Overplotted cells in the left panel have dimensions  $40 \text{ pc} \times 40 \text{ pc}$  and represent the size of the initial (lowest) resolution of the AMR setup. Right panel shows the configuration of the same region reached by the simulation with  $40 \text{ pc} \times 40 \text{ pc}$  cells.

### 3.3.2 Matching the fixed-grid results

Once established the best choice for this parameter, another set of tests has been run, in order to compare the AMR to the static grid results obtained with ENZO. The domain has been divided into  $188 \times 62$  cells of initial resolution  $32 \text{ pc} \times 32 \text{ pc}$  each. By setting the Refinement parameter to 2 and the highest generable level to 3, the simulation is designed to reach, in the domain's densest regions, a  $4 \text{ pc} \times 4 \text{ pc}$  resolution. This is the same resolution adopted in the fixed-grid, adiabatic simulations obtained with ATHENA and ENZO. Four different values have been selected for the overdensity parameter, starting from previous analysis'

best compromise between number of grids and accuracy (0.1) towards the minimum one used (0.0078125). The results are shown in fig. 3.6 and are definitely not that reassuring.

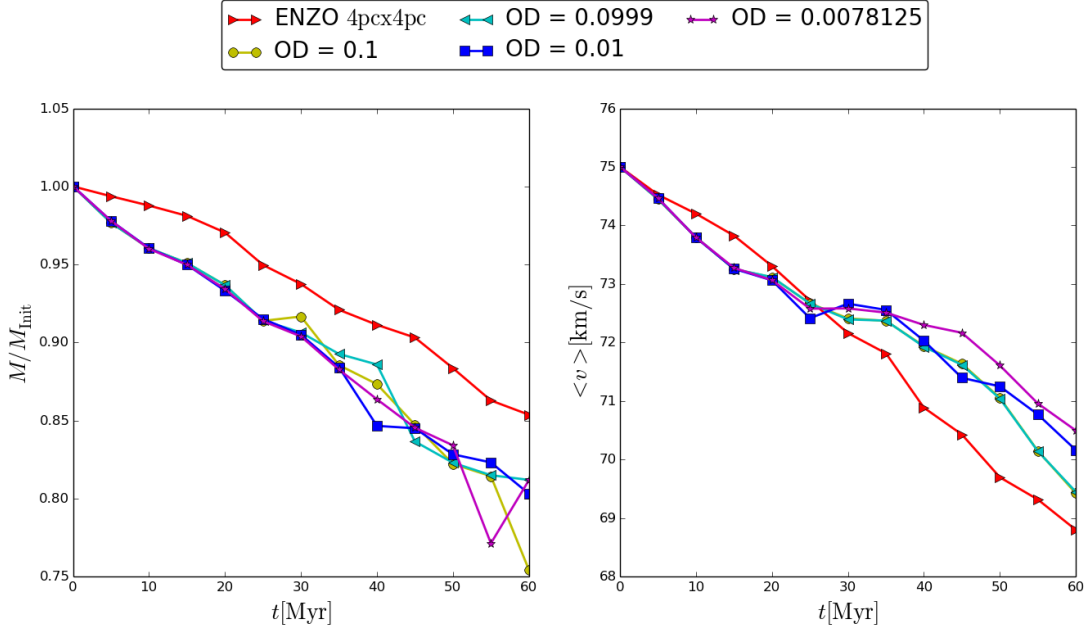


Figure 3.6: Cold gas mass and mean velocity temporal evolution for different initial overdensities. Lowest resolution:  $32 \text{ pc} \times 32 \text{ pc}$ ; highest resolution:  $4 \text{ pc} \times 4 \text{ pc}$ .

$\rho_{\text{min}}$	0.167	0.167	0.017	0.013
Lev 1	0.668	0.667	0.067	0.052
Lev 2	2.672	2.645	0.267	0.209
Lev 3	10.688	10.581	1.069	0.835

Densities are in  $10^{-26} \text{ g/cm}^3$ .

Table 3.3: Adopted values for Minimum over-densities and density thresholds at each level.  $\rho_{\text{min}}$  is the density threshold of level 0 grids in physical units. From left to right, they correspond to the over-densities  $OD = 0.1, 0.0999, 0.01$  and  $0.0078125$ , whose results are shown in fig. 3.6.

Even if, as for the previous analysis, a convergence for solutions in AMR implementations is reached, it seems that a discrepancy with the static grid results exists: AMR systematically overestimates the evaporation of the cloud (the de-

crease of cold gas due to heating up by the coronal gas). This discrepancy is of about 10% during the whole evolution, meaning that this treatment for refinement is not completely accurate. Also, velocities show a divergence starting from 30 Myrs, up till the end of the simulation. For completeness, tab. 3.3 shows the new values for initial over-densities adopted and the density tresholds for each level.

### 3.3.3 Fine tuning of the overdensity parameters

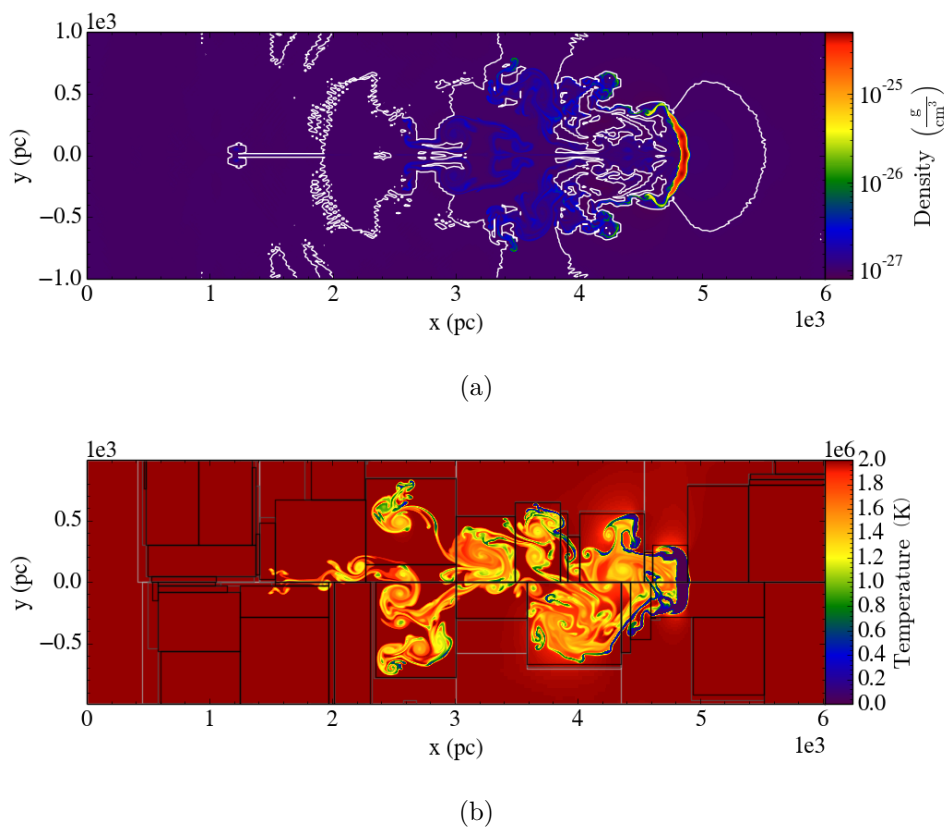


Figure 3.7: Contours at  $\rho = 1. \times 10^{-27} \text{ g/cm}^3$  on a density snapshot obtained from the fixed-grid simulation after 60 Myrs (3.7a) and temperature profile, at the same time, for our fine-tuned overdensity simulation (see text) with overplotted refinement grids (3.7b).

The last attempt of finding convergence between non-AMR and AMR codes, using the criterion before mentioned is performed on the basis of an “a posteriori” analysis. We tried to select by hand the regions that we wished to be computed

at high resolution by displaying density contours on ENZO 4 pc  $\times$  4 pc resolution static grid's output. Then we determined a set of parameters for the over-density criterion that let us impose the highest resolution upon the desired regions. A contour at density  $1 \times 10^{-27}$  g/cm<sup>3</sup> (corresponding to 0.1 in code units) has been selected (fig. 3.7a). This choice is made in order to cover the wide area including both wake and cloud throughout the whole evolution of the system.

There are two possible ways to reach the highest resolution at these densities. The first one is to set the initial over-density to  $\rho_{\text{flag}} = \rho(l=3)/2^{3*d} = 0.1/2^6 = 0.0016$ , but the first analysis showed that for a value below 0.1 the refinement is too intensive, and a large part of the whole domain is refined, slowing down enormously the simulation. The second one is to take an initial overdensity slightly larger than the coronal density (in code units: 0.0998) and modify the exponent of equation 2.18 (`MinimumMassForRefinementLevelExponent`,  $\epsilon_1$ ), obtained by inversion of equation 2.18, and precisely:

$$\epsilon_1 = \frac{1}{l} \log_r \left[ \frac{\rho(l)}{\rho_{\text{init}}} \right] - d \quad (3.3)$$

Where  $l$  is the level,  $\rho(l)$  and  $\rho_{\text{init}}$  are the density thresholds at level  $l$  and 0 respectively and  $r$  is the refinement parameter.

Level ( $l$ ), Resolution	1, 16 pc	2, 8 pc	3, 4 pc
$\rho(l)$ , $\epsilon_1 = -1.99952$	0.16688	0.16695	0.16700
$\rho(l)$ , $\epsilon_1 = 0$	0.667	2.669	10.677

Densities are in  $10^{-26}$  g/cm<sup>3</sup>.

Table 3.4: Adopted fine-tuned values for Minimum overdensities and densitie thresholds at each level in the case of  $\epsilon_1 = 0$  (default) and the adopted value. The over-density parameter at the coarsest level (32 pc) is  $0.16683 \times 10^{-26}$  g/cm<sup>3</sup>.

Using  $\epsilon_1$  (by default  $\epsilon_1 = 0$ ), a modification to the density thresholds for each level is possible to perform. We want to create 3 levels (composed of grids at resolutions 16 pc  $\times$  16 pc, 8 pc  $\times$  8 pc and 4 pc  $\times$  4 pc respectively) in a way that the higher one resolves densities of  $1 \times 10^{-27}$  g/cm<sup>3</sup>. Following this second method, the value  $-1.99952$  is found for  $\epsilon_1$ . In this way the gap in density between each

level is drastically reduced, as shown in tab. 3.4, and the desired density is reached at the maximum spatial resolution  $4 \text{ pc} \times 4 \text{ pc}$ . Results for this last attempt are shown in fig. 3.8. There is no appreciable improvement with respect to the other cases, moreover the computational time is much longer.

The overall distribution of the best resolution grids follows the contours outlined in fig. 3.7a quite well, as one may see in fig. 3.7b. The discrepancy between AMR and non-AMR codes is still up to 10%. Another important feature showed in fig. 3.7b is the distortion in gas spatial distribution with respect to the horizontal axis. If in static grid codes there is a perfect horizontal symmetry, in the AMR case, especially the last one analysed, we see no preferential axis of symmetry.

By comparing with the static grid  $4 \text{ pc} \times 4 \text{ pc}$  resolution simulation obtained with ENZO (see fig. 3.1), the difference is quite striking and could open to an interesting questioning about morphologies in AMR simulations. However, in order to proceed with the further examination of the physical problem treated, we do not explore the causes and the consequences of this spatial deformation here.

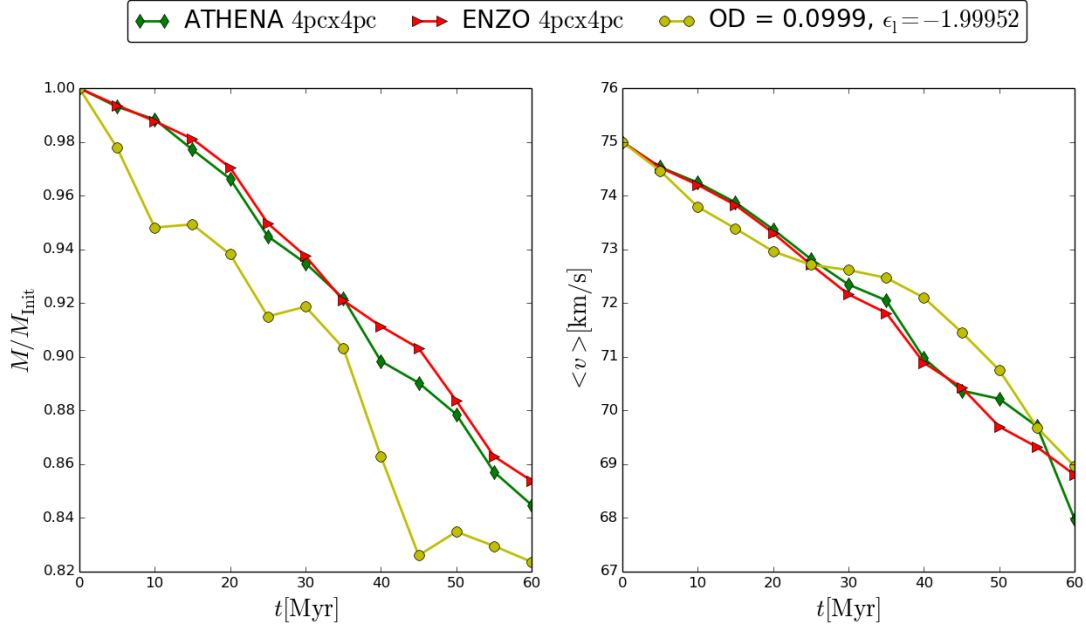


Figure 3.8: Cold gas mass and mean velocity temporal evolution for different initial overdensities. Lowest resolution:  $32 \text{ pc} \times 32 \text{ pc}$ ; highest resolution:  $4 \text{ pc} \times 4 \text{ pc}$ . Comparison of non-AMR and AMR treatments.

### 3.3.4 Initial high-resolution box

In the AMR experiments performed so far the full simulation box starts with constant resolution and only after the first time step the refinement criteria are applied. Here we consider the case in which the cloud is initially enveloped in a grid at maximum resolution ( $4 \text{ pc} \times 4 \text{ pc}$ ). The domain's setup can be seen in figure 3.9.

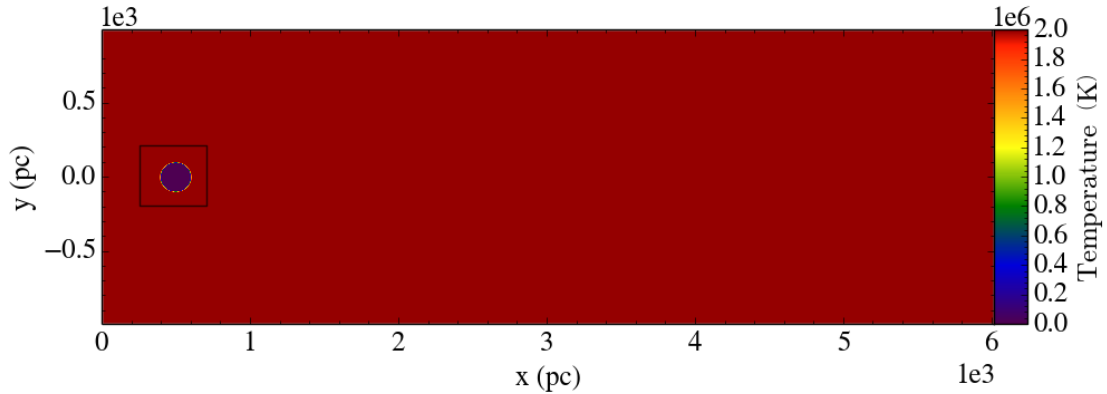


Figure 3.9: The cloud is initially enveloped in a  $4 \text{ pc} \times 4 \text{ pc}$  grid, while the rest of domain is at  $32 \text{ pc} \times 32 \text{ pc}$ .

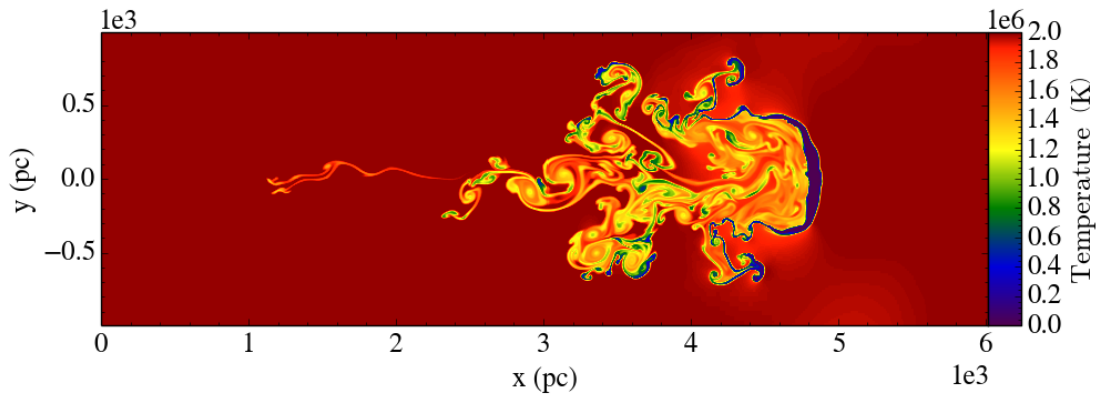


Figure 3.10: 60 Myrs temperature snapshot of AMR simulation with the initial configuration (high resolution box over the cloud) shown in fig. 3.9.

The evolution of the cloud with this initial configuration is much more similar to the one obtained at fixed resolutions, at least for what concerns the temporal evolution of the cold gas mass and velocity. Results are shown in figure 3.11.

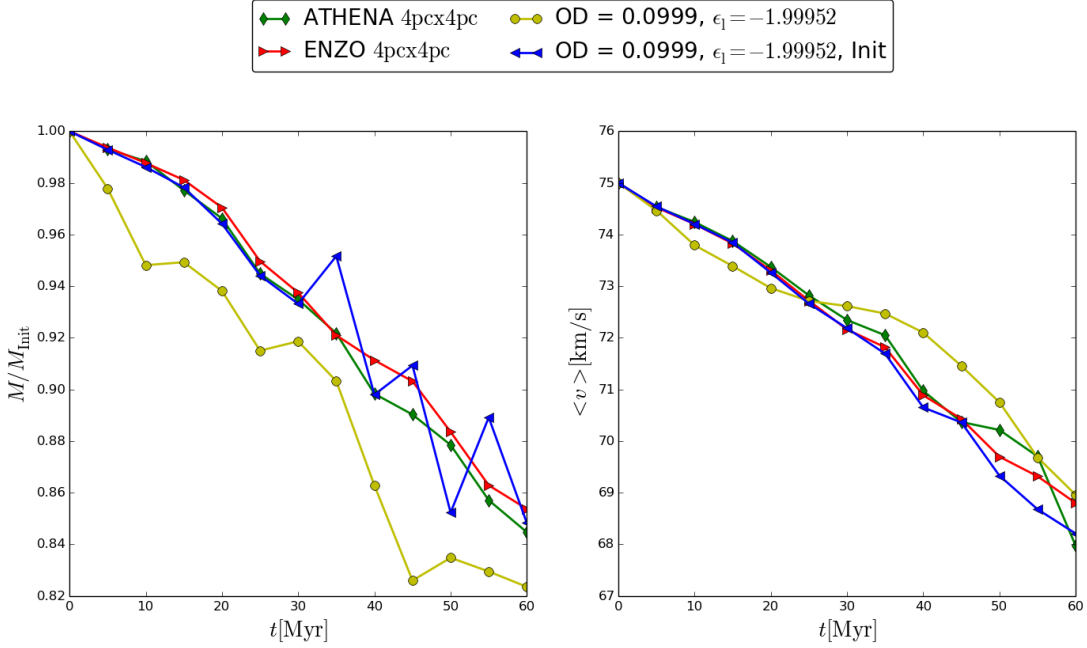


Figure 3.11: The blue line is obtained with the initial configuration described in the text. Overplotted are the evolution for the best of the previous cases and fixed grid ENZO and ATHENA results.

The overall agreement is much better than in the cases previously analysed, except for strong oscillations in the mass that do seem to have a counterpart in the velocity after 30 Myrs. At 60 Myrs a convergence is found. Also, a better morphological reproduction of the non-AMR simulation is observed, as one may see in fig. 3.10, even if an overall asymmetry is present. In fig. 3.12 and fig. 3.14 we report the temporal evolution of cold gas mass and velocity respectively, obtained with values for the over-density parameter already tested without the initial box setting. Every value for the over-density parameter (with  $\epsilon_1 = 0$ ), now well reproduces the results obtained with the fixed-grid simulations, exception made for  $OD = 5$ . However, despite this agreement, the gas distribution is very different from case to case (as shown in fig. 3.13) and the coverage of the grids at high resolution resembles the one obtained without the Initial Box setting.

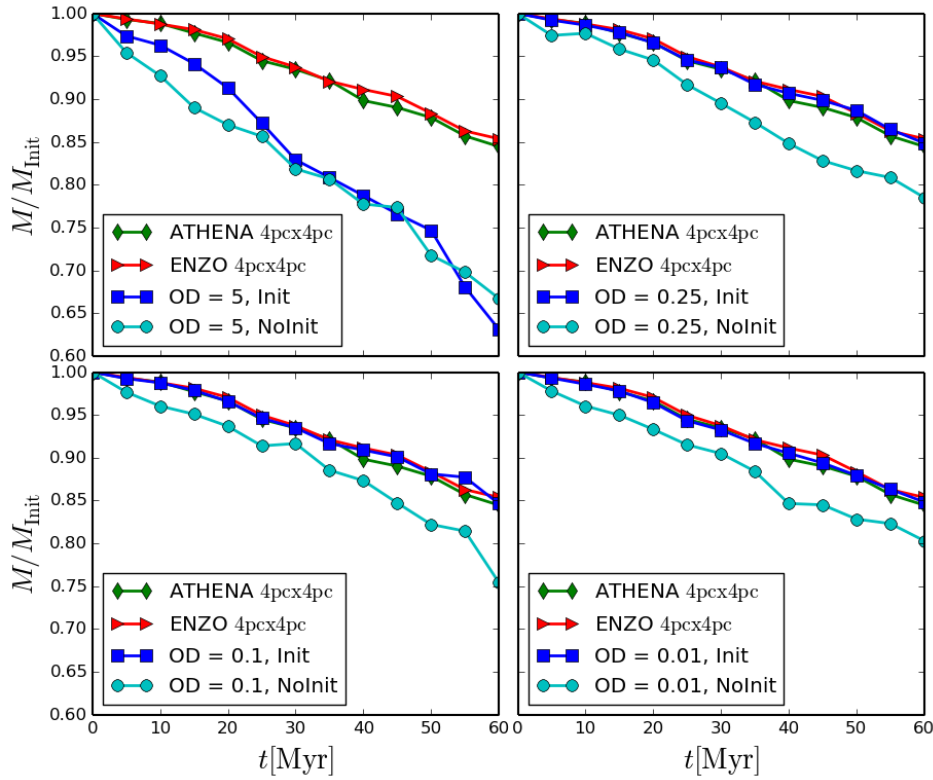


Figure 3.12: Comparison of cold gas mass temporal evolution as obtained with different values for the over-density parameter. In every box, the blue squares refer to simulations with the initial box configuration, while the cyan dots to the simulations with coarse initial resolution (section 3.3).

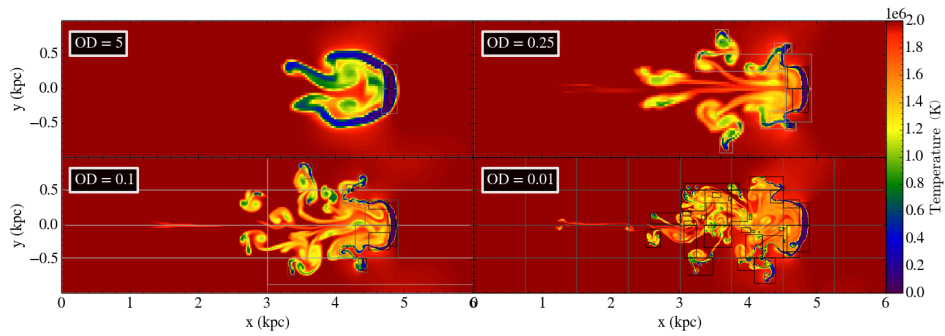


Figure 3.13: Temperature snapshots of the cloud in its final stage after 60 Myrs, for the same 4 cases of initial overdensity (shown in the upper left of each panel), whose results are shown in fig. 3.12 and 3.14

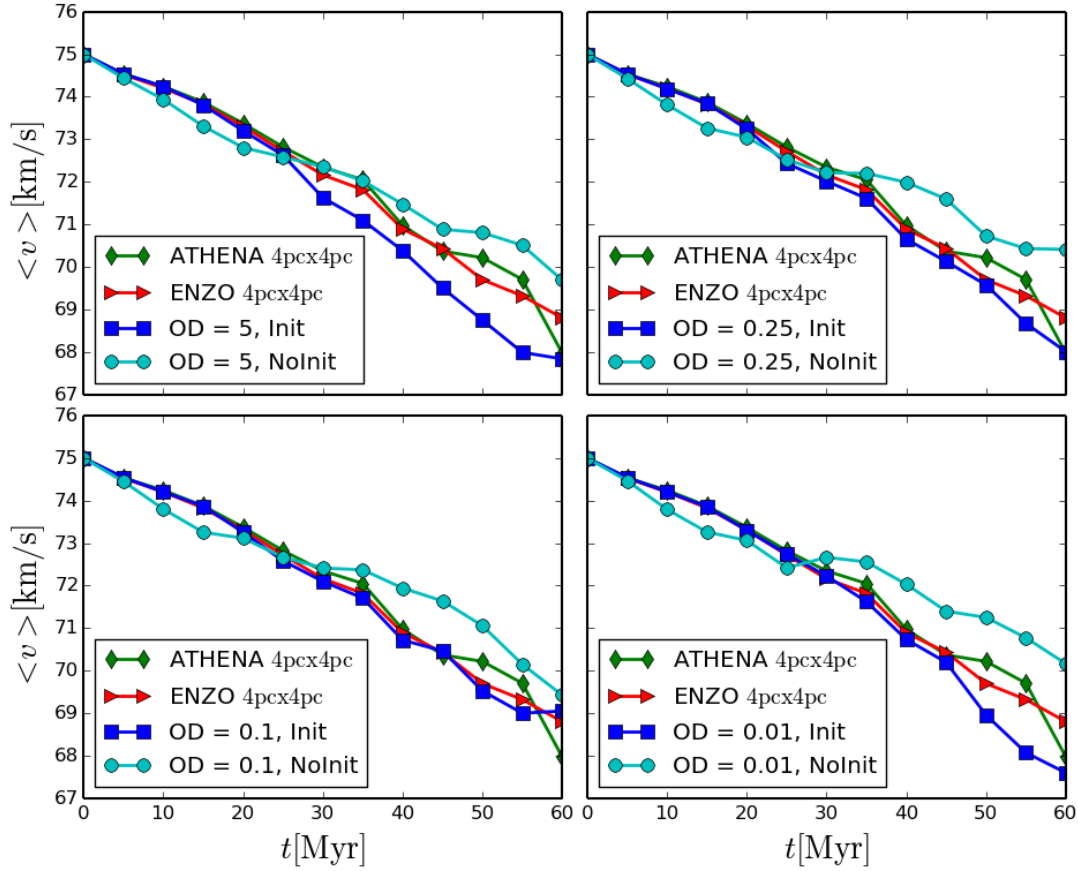


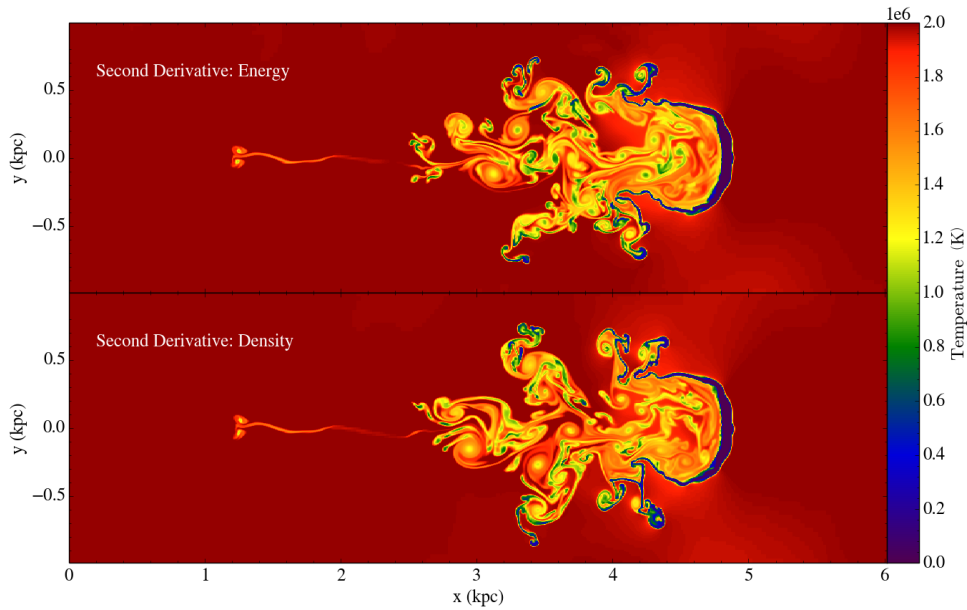
Figure 3.14: Comparison of cold gas velocity temporal evolution as obtained with the values for the over-density parameter shown in 3.12. In every box, the blue squares refer to simulations with the initial box configuration, while the cyan dots to the simulations with coarse initial resolution (section 3.3).

As previously mentioned, the over-density is the most used criterion for refinement in AMR simulations. This is why this chapter has been focussed on the exploration of the whole parameter-spectrum for this criterion. We can conclude that, at least for the study of turbulent mixing between different gas phases one needs to adopt the following precautions: i) an initial refinement of the region of interest (region at high density), ii) use very low values of the over-density parameter, ideally two orders of magnitude lower than the default value in ENZO. This makes the use of this criterion rather impractical and in the following we explore the possibility of employing different refinement criteria.

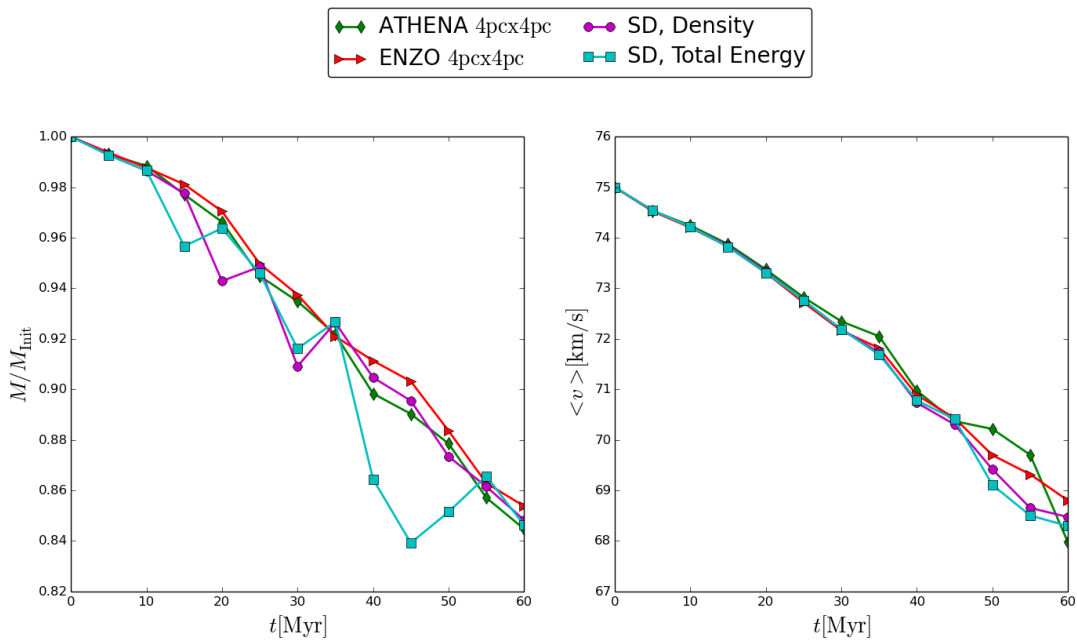
### 3.3.5 Other refinement criteria

Using the same initial setup, two more criteria for refinement have been adopted in two separate runs. The two cited criteria are the Refinement for Second Derivative and the Refinement By Slope, both described in chapter 2. The former has been taken into account as applied to two different fields: density and total energy. In each case, the associated parameters are fixed to the same values and precisely: `MinimumSecondDerivativeForRefinement` = 0.3, and `SecondDerivativeEpsilon` = 0.01. The first one is the threshold that a cell needs to exceed in order for it to be refined. The second is a parameter used to avoid refining around oscillations of the field with respect to the mean value. The higher the value, the more it will filter out. Both these values are default. A comparison of these two tests is shown in fig. 3.15b. At first glance one can immediately realize that this criterion performs better than the overdensity. An overall agreement with respect to the fixed-grid simulations is present throughout the all evolution. In particular, at this point in analysis, this criterion seems to provide the best results out of all the previous cases, both for its convergence to the Non-AMR case and for the spatial distribution of the gas (see fig. 3.15). Furthermore, from figure 3.15b, a better convergence is found if this criterion is applied to density, instead of total energy. As one may notice from figure 3.16, we reach a convergence within 3% for mass and 0.9% for mean velocity.

The last criterion used is the Refinement By Slope. Similarly to the Second Derivative criterion, this method refers to a spatial gradient of a certain field (selected by the user) as a discriminating property for refinement. If, in a given cell, this value is greater than a threshold (imposed by the user), the cell is refined. By using the default value for the parameter `MinimumSlopeForRefinement` (the threshold), while still adopting the initial setup, we found that this criterion grants the best reproduction of the fixed-grid data, with an overall discrepancy of less than 1% during the whole evolution except for the time 40 Myrs where the divergence reaches a maximum of 4%. A comparison between the best criteria for the adiabatic case is shown in figure 3.16.



(a) Morphological comparison of both of SecondDerivative tests.



(b) Cold gas mass and velocity temporal evolution for two tests.

Figure 3.15: A morphological (fig. 3.15a) and quantitative comparison (fig. 3.15b) between the same criterion (Second Derivative) applied to two different fields: Density and Total Energy.

Tab. 3.5 shows the time performances of all the best cases for each criterion used, compared to the computational time needed by the fixed-grid simulation at resolution  $4 \text{ pc} \times 4 \text{ pc}$ . All simulations have been performed on a 8 CPUs architecture.

	Fixed-grid	OD	SD	Slope
<b>Computational time</b>	$\sim 8\text{h}$	$\sim 3\text{h}$	$\sim 34\text{min}$	$\sim 18\text{min}$

Table 3.5: Computational time needed for fixed-grid and AMR simulations using the described Refinement Criteria. OD indicates the Over-density criterion with fine-tuning; SD the Second Derivative applied to density and Slope is applied to density too.

In conclusion, we identify the SecondDerivative and the Slope criteria applied to density as the best suited for this problem, the latter being the fastest.

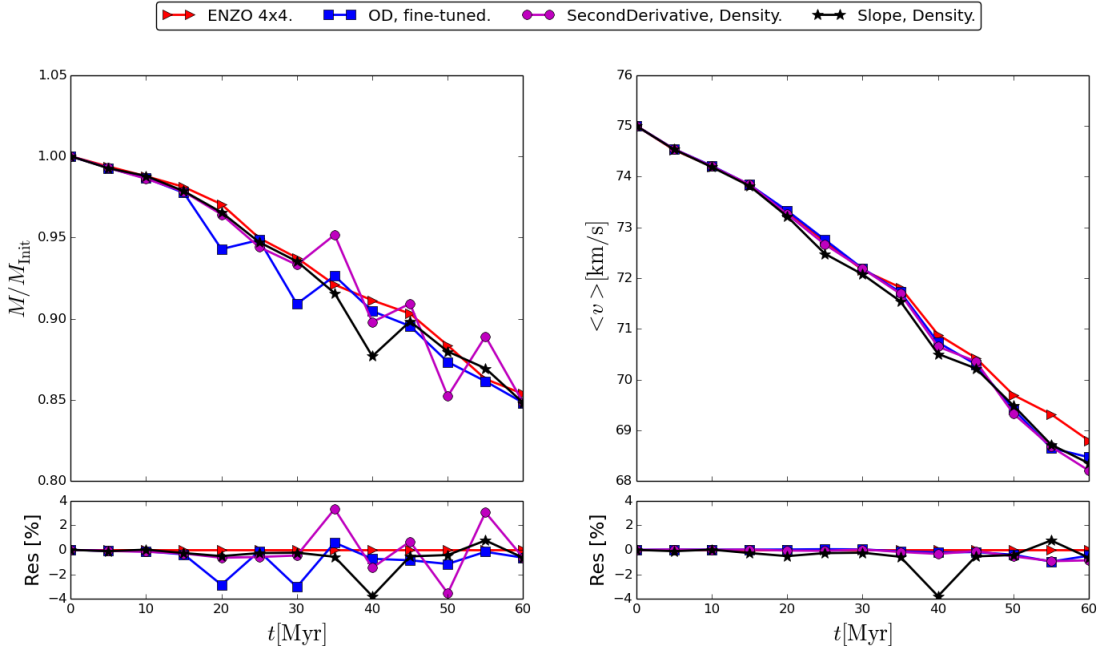


Figure 3.16: Comparison in cold gas mass and velocity for the adiabatic case. The two most accurate criteria are compared with a percentage scatter with respect to the ENZO simulation at fixed resolution  $4 \text{ pc} \times 4 \text{ pc}$ .

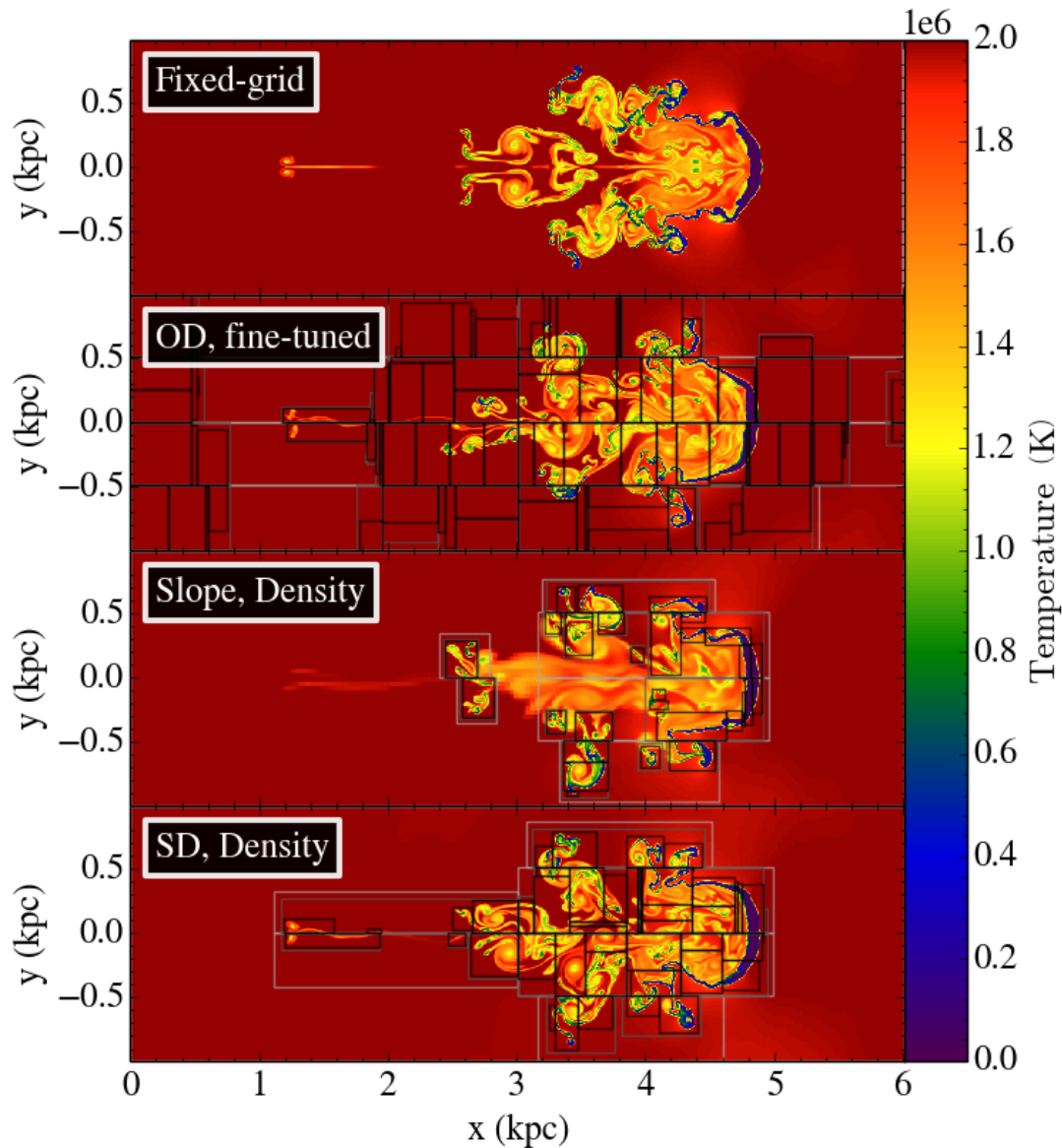


Figure 3.17: Temperature snapshots after 60 Myrs obtained with the best simulations for the adiabatic case of the Galactic Fountain mechanism.

With respect to the over-density they do not require a fine-tuning of the parameters and produce the best results in less computational time. It is thus reasonable to use the Slope criterion applied to density as our first choice, followed by SecondDerivative (applied to density) and over-density (fine-tuned). By looking at the temperature snapshots in fig. 3.17, a good follow-up of the evolution of the

cloud is visible for all the three criteria used. However, a large portion of the entire domain is resolved at the highest resolution for the over-density case, causing the simulation to slow down considerably with respect to the other two shown. Both the SecondDerivative and the Slope instead, guarantee an efficient coverage of the domain, resolving at the highest resolution only the necessary regions, thus exploiting the true strength of AMR techniques. Furthermore, as afore mentioned, the definition of an initial box resolving the cloud at the highest resolution is essential in order to have a good match between the results.



# Chapter 4

## Simulations with Radiative Cooling

In the previous chapter we found the best refinement criterion for adiabatic AMR simulations using the ENZO code. In this chapter we consider a more realistic treatment by including radiative cooling in the calculation. Our implementation of radiative cooling is based on previous works by Marinacci et al. (2010) and Armillotta et al. (2016), where the adopted cooling function is taken from Sutherland & Dopita (1993) and implemented in ENZO as explained in section 2.4.1.

As previously described in chapter 3, during the motion of the cold fountain cloud through the hot coronal gas, a turbulent wake develops behind the cloud where the two gas components mix at an intermediate temperature. If this mixture can radiatively cool, part of this gas can condense within the wake. Both Marinacci et al. (2010) and Armillotta et al. (2016) used fixed-grid codes.

In this chapter, we try to understand how the introduction of the AMR treatment affects the results obtained via fixed-grid codes and how the results depend on the different refinement criteria. The fixed-grid results are hereby considered the most accurate, and all the AMR simulations performed are compared to these ones. In the next sections we use the expression *accuracy* relatively to AMR simulations, to indicate their accordance with the fixed-grid results.

## 4.1 Comparison with adiabatic simulations

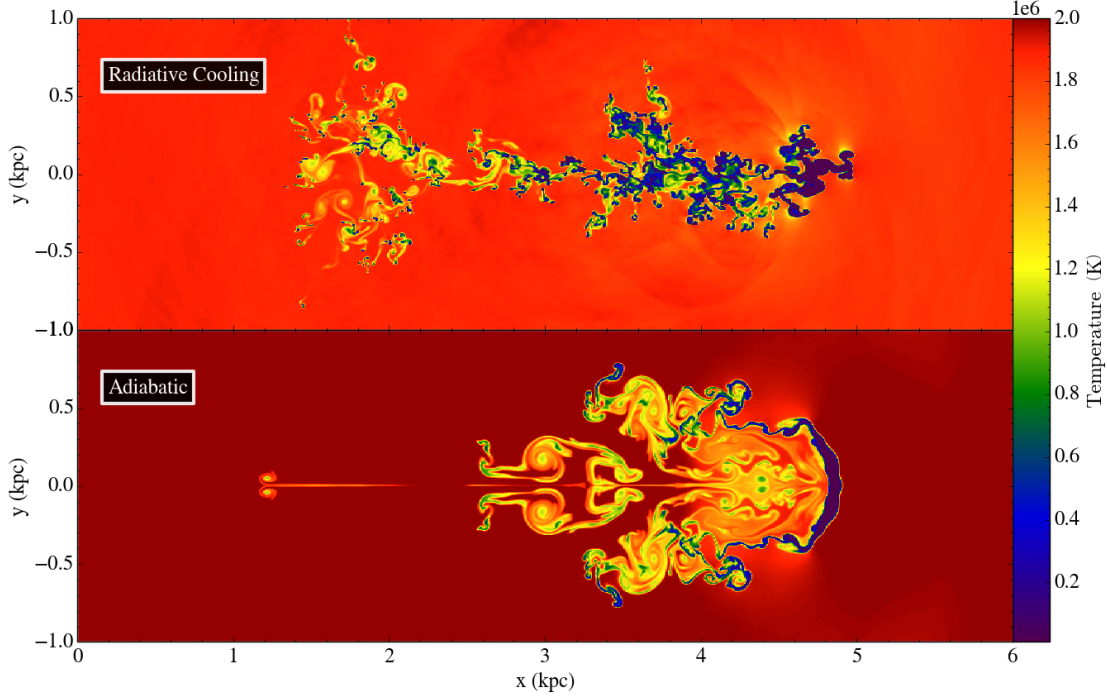


Figure 4.1: Temperature snapshots after 60 Myrs of a cold ( $T = 10^4$  K) cloud moving through the hot ( $T = 2 \times 10^6$  K) coronal gas. The top panel is obtained when radiative cooling is included in the code, while the bottom panel shows the adiabatic case studied in the previous chapter. Both the simulations are performed using ENZO as a fixed-grid code at resolution  $2 \text{ pc} \times 2 \text{ pc}$ .

The introduction of radiative cooling, greatly modifies the characteristics of the wake behind the head of the cloud. In fig. 4.1 we show the temperature snapshots of the system after 60 Myrs from the beginning of the cloud's motion through the hot ( $2 \times 10^6$  K) coronal gas. Both the simulations are performed using ENZO as a fixed-grid code at resolution  $2 \text{ pc} \times 2 \text{ pc}$ , but the top panel is obtained when radiative cooling is permitted, while the bottom panel shows the adiabatic case studied in the previous chapter (chapter 3). First of all, the wake is far less extended along the  $y$ -direction in the simulations with radiative cooling. The initially spherical cloud is largely disrupted at the end of the simulation with radiative cooling, while it is symmetrically flattened in the perpendicular direction of the motion in the adiabatic case. Also, the wake is much cooler than in the adia-

batic case where the development of turbulence and vortexes limits the presence of cold gas in the external regions. The motion is almost laminar there and cold gas can survive without mixing. The gas inside the wake is at temperature between  $1 \times 10^4$  K and  $2 \times 10^6$  K, but it is on average higher in the adiabatic case than in the cooling case. The cold cloudlets populating the wake in the radiative cooling case, cannot be seen in the adiabatic case, meaning that they can be formed only assuming a combination of both turbulence and cooling. The interaction between the corona and the cloud triggers the condensation of the hot gas onto the cloud's wake, enhancing the amount of cold gas during the evolution of the system. When radiative cooling is permitted, cold gas is detectable also at large distances from the head, leaving a trace of the cloud's motion during its whole evolution. This behaviour is completely absent in the adiabatic case, where the warm gas in the back of the wake is re-heated through the mixing with the coronal gas. Finally, after 60 Myrs, the coronal temperature decreases from  $T = 2 \times 10^6$  K to  $T \simeq 1.8 \times 10^6$  K, due to the introduction of radiative cooling.

## 4.2 Temporal resolution

In order to find the best compromise between computational time and accuracy a set of four fixed-grid different simulations at increasing resolutions have been performed with ENZO (fig. 4.2). At  $20 \text{ pc} \times 20 \text{ pc}$  and  $10 \text{ pc} \times 10 \text{ pc}$  resolutions the results are greatly affected by numerical diffusion: the cloud maintains its shape throughout the whole evolution and mixing is not efficient. As we move to higher resolutions, the cloud is more and more disrupted, producing a long wake of turbulent gas only in the  $4 \text{ pc} \times 4 \text{ pc}$  case.

We report the temporal evolution of cold gas mass and velocity in fig. 4.3. Note that the condensation increases with increasing resolution. Increasing the resolution is the general solution to the problem of numerical diffusion, as mentioned in chapter 3. Reducing the effect of numerical diffusion leads to a better representation of mixing between the coronal and the cloud gas, because structures where the mixing is dominant are resolved with a sufficient amount of cells. For the following test suite, we chose to work at the resolution  $4 \text{ pc} \times 4 \text{ pc}$ .

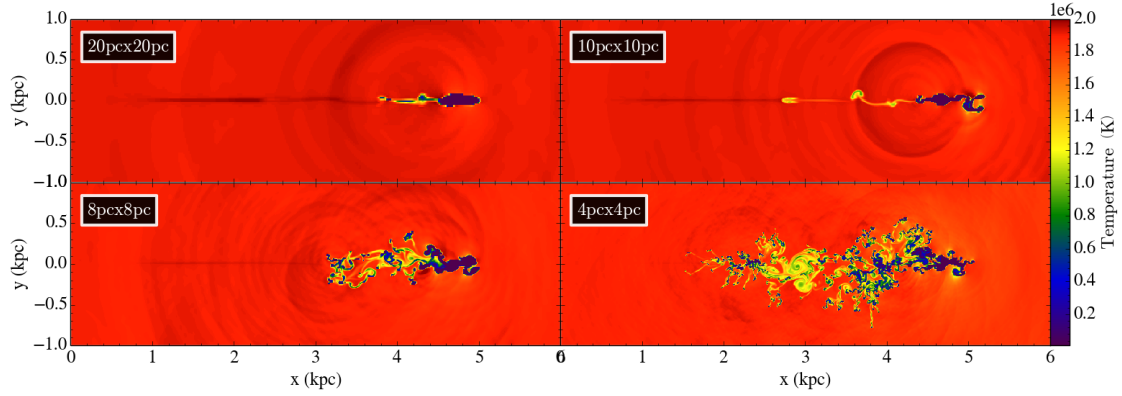


Figure 4.2: A comparison of the four simulations cited in the text is shown here: 20 pc  $\times$  20 pc, 10 pc  $\times$  10 pc, 8 pc  $\times$  8 pc and 4 pc  $\times$  4 pc. Each panel shows a temperature snapshot of the simulations after 60 Myrs.

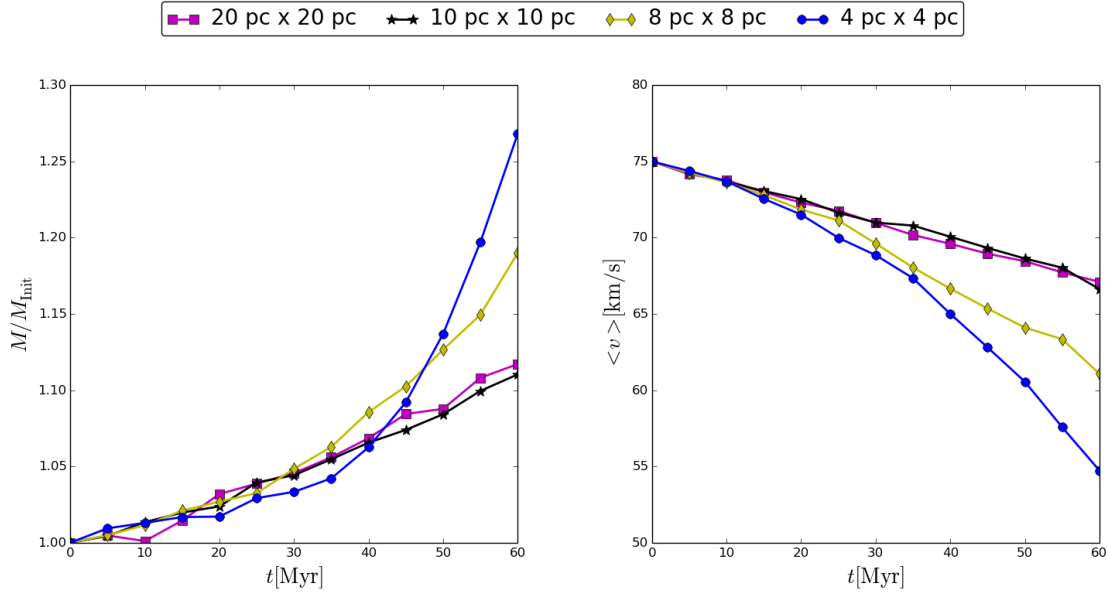


Figure 4.3: A comparison of cold ( $T < 2 \times 10^4$  K) gas mass and mean velocity temporal evolution is shown for four simulations obtained with ENZO, fixed-grid at different resolutions.

As we outlined in the previous chapter, fixed-grid simulations at 4 pc  $\times$  4 pc performed with ENZO (when AMR is not active) and ATHENA, reach a good agreement in the estimation of the cold gas mass during the whole evolution of the system. How radiative cooling perturbs this agreement depends largely on

its implementation in both the codes. If we consider ENZO as a fixed-grid code, no level hierarchy is present, thus the timestep is computed on the only existing grid, covering the entire domain. Furthermore, the absence of gravitational and magnetic fields implies that the only condition on the determination of timestep is the *Courant-Friedrichs-Lewy* (CFL) condition for accuracy and stability of an explicit finite difference discretization of the Euler equations. In particular, ENZO imposes the effective timestep to be the minimum between all the timesteps computed for every cell of the computational domain. Thus, in a one-dimensional representation:

$$\Delta t_x = \min \left( k_{\text{CFL}} \frac{\Delta x}{c_s + |v_x|} \right) \quad (4.1)$$

Where  $\Delta x$  is the dimension of the cell,  $c_s$  is the sound speed of the gas in that cell and for an ideal fluid is  $c_s = (\gamma P / \rho)^{1/2}$  ( $\gamma$  being the ratio of specific heats,  $P$  the pressure and  $\rho$  the density of the cell).  $v_x$  is the velocity of the gas in the cell along  $x$ -direction and  $k_{\text{CFL}}$  is a dimensionless, numerical constant with value  $0 < k_{\text{CFL}} \leq 1$  that ensures that the CFL condition is always met. This one-dimensional formulation is extended to a multi-dimensional geometry using the harmonic average of the timestep found along each of the coordinate axes. So letting  $\Delta t_x$ ,  $\Delta t_y$  and  $\Delta t_z$  be the analogous of equation 4.1 along the  $x$ ,  $y$  and  $z$  axes we have:

$$\Delta t_{\text{CFL}} = \min \left( \frac{k_{\text{CFL}}}{1/\Delta t_x + 1/\Delta t_y + 1/\Delta t_z} \right) \quad (4.2)$$

A typical value for the CFL parameter is  $k_{\text{CFL}} \sim 0.3-0.5$  (Bryan et al. 2014). When radiative cooling is considered, a further constraint on the timestep is used only for the energy update, in order to include energy losses due to radiative cooling. In particular, the cooling timestep is not permitted to exceed 10% of the minimum cooling time. Thus, while the hydrodynamical timestep is limited by the CFL condition, the cooling process is sub-cycled with a cooling timestep resolution. When an adiabatic simulation is performed with ATHENA, the timestep is also limited by the CFL condition. However, when a cooling function is implemented the whole hydrodynamics is resolved with a timestep equal to the 10% of the smallest cooling time.

In order to compare the results obtained with the two codes, we need first to find

an agreement between the timesteps computed at every time by each one. Using ENZO as a fixed-grid code (without AMR), we performed three simulations at three different CFL parameters: 0.4, 0.1, 0.05 and compared the outcomes with the results obtained with ATHENA at the same resolution ( $4 \text{ pc} \times 4 \text{ pc}$ ). This comparison is shown in fig. 4.4.

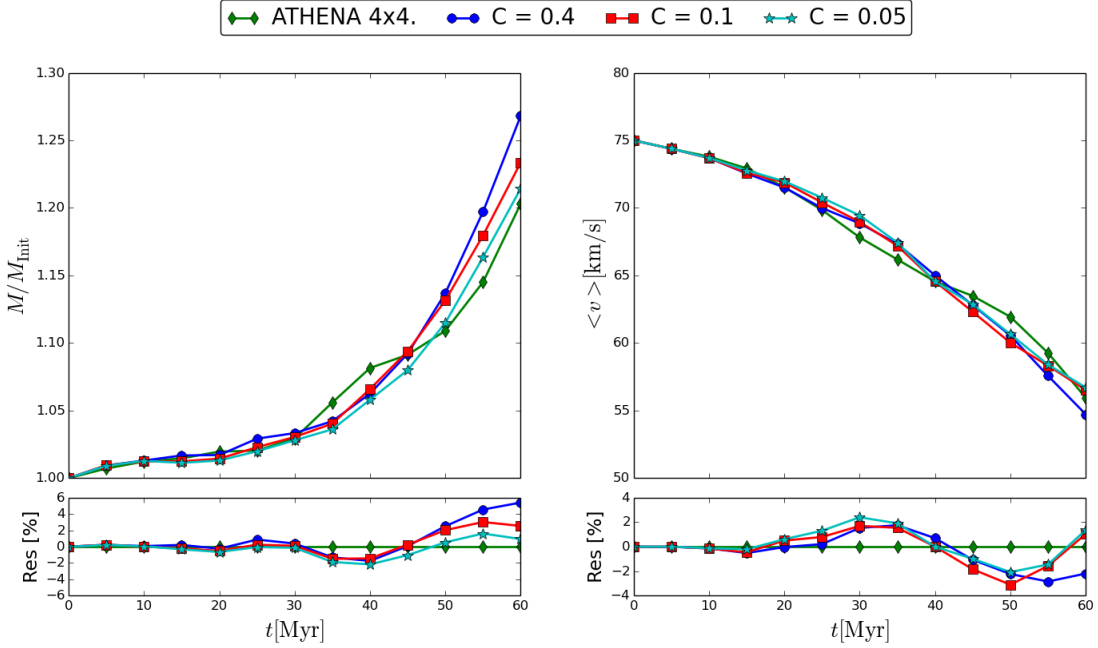


Figure 4.4: Cold gas mass and velocity temporal evolution for three simulations with different CFL parameter obtained with ENZO, compared to ATHENA. Below each panel the residuals with respect to ATHENA results are shown.

We notice that the cold gas mass decreases with decreasing CFL parameter, thus the timestep. The smallest deviation from ATHENA’s results is obtained with a CFL parameter equal to 0.05, while for a standard value (i.e. 0.4) the divergence is non-negligible at the end of the simulation. Given the relatively small difference between the cases with 0.1 and 0.05 (at most one percentage point in the condensation), we choose to adopt, for the following simulations, a CFL parameter equal to 0.1 in order to maintain a low computational cost.

In Armillotta et al. (2016), simulations have been performed at a fixed resolution of  $2 \text{ pc} \times 2 \text{ pc}$ , while the timestep is imposed to be 10% of the cooling time, in order to temporally resolve the radiative cooling. Once the best CFL parameter

has been found, we enhanced by a factor 2 the resolution in our simulations, in order to compare the results obtained at  $2 \text{ pc} \times 2 \text{ pc}$ . Also, we extended the time of computation to 80 Myrs in order to cover a greater fraction of the typical orbital time of a fountain cloud (Fraternali & Binney 2006). The initial setup of the simulations here described is the same used in the previous chapter (see tab. 3.1 in section 3.1): the coronal temperature and number density are  $T = 2 \times 10^6 \text{ K}$  and  $n = 1 \times 10^{-3} \text{ cm}^{-3}$ , while the temperature of the cloud's gas is  $T = 10^4 \text{ K}$  and the number density is obtained assuming pressure equilibrium with the hot medium, finding  $n = 1 \times 10^{-1} \text{ cm}^{-3}$ . Both fluids have metallicity  $[Fe/H] = 0.5$ .

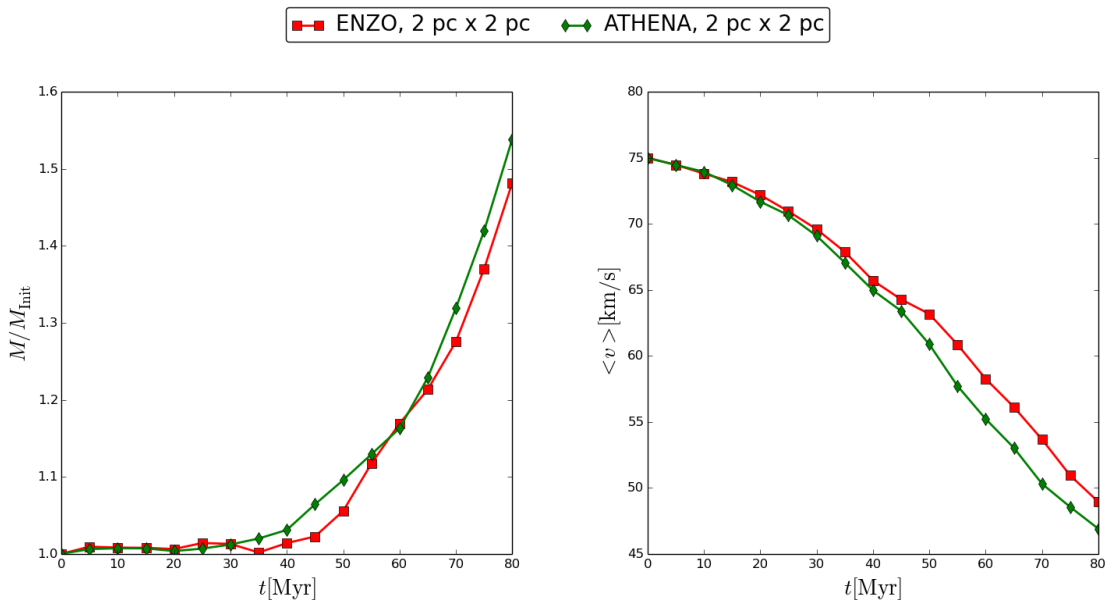


Figure 4.5: Comparison of cold gas mass and velocity temporal evolution between ATHENA and ENZO with no AMR at fixed resolution  $2 \text{ pc} \times 2 \text{ pc}$ .

The comparison between the results is shown in fig. 4.5. A general agreement between the two codes is evident, but deviations of ENZO with respect to ATHENA are clear at any time. In particular, at 80 Myrs ENZO underestimates the condensation found with ATHENA by  $\sim 10\%$ , while the cold gas mean velocity is of order 7% overestimated. Therefore, it appears that mixing between the two phases of the gas is slightly less efficient using ENZO. In Fig. 4.6 we present the fixed-grid simulation obtained with ENZO at the resolution  $2 \text{ pc} \times 2 \text{ pc}$ .

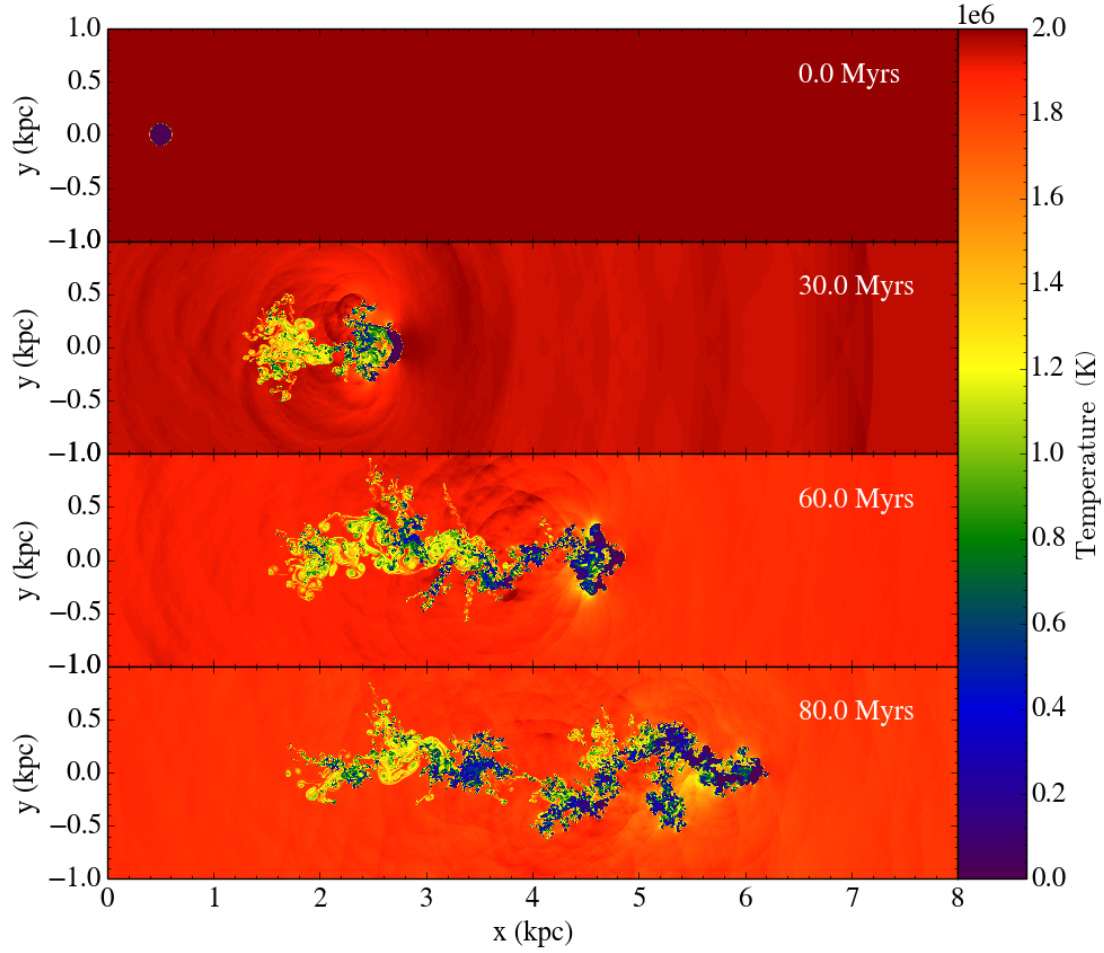


Figure 4.6: Temperature snapshots of the gas at different times (upper right corners) from the start of the fixed-grid simulation at resolution  $2 \text{ pc} \times 2 \text{ pc}$  obtained with ENZO.

### 4.3 AMR simulations

In this section we describe the results obtained with ENZO once the AMR is active. We based our analysis on the criteria described in chapter 2 and searched for a convergence with the fixed-grid simulations, obtained with ENZO and ATHENA. In chapter 3 we pointed out how the introduction of a high resolution box enveloping the cloud in the initial configuration is essential for the outcome of this kind of simulations. We also considered three different refinement criteria in order to find the most suited for our case, identifying the Slope refinement criterion as the fastest and the most accurate. The same criteria are used in these simulations.

Moreover, we increased the number of levels from 3 to 4 with a refinement factor  $r = 2$ . Thus, while the root (coarsest) grid has a resolution  $32 \text{ pc} \times 32 \text{ pc}$ , the resolution on level 4 is  $2 \text{ pc} \times 2 \text{ pc}$ .

### 4.3.1 Over-density criterion

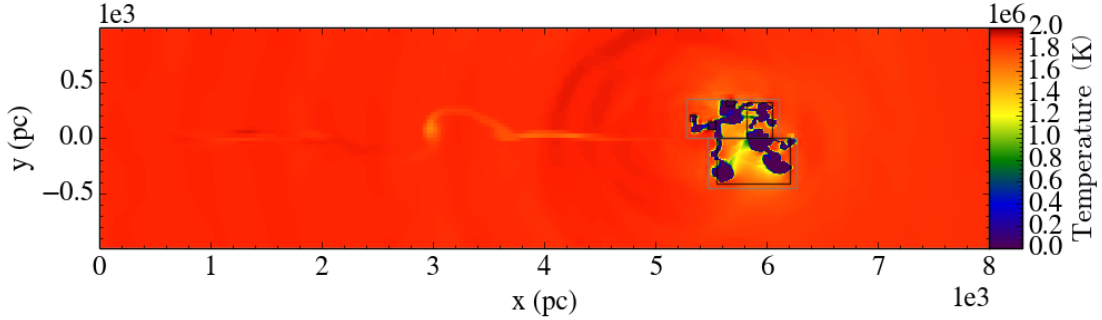


Figure 4.7: Temperature snapshot of the cloud after 80 Myrs, using the over-density criterion for refinement and a density threshold for level 0  $OD = 4$ . The overall resolution is too low for the Kelvin-Helmholtz instability to fully develop. The distribution of the boxes at the highest resolution ( $2 \text{ pc} \times 2 \text{ pc}$ ) is barely sufficient to cover the head of the cloud throughout the evolution. Due to this behaviour, the wake is completely absent.

In chapter 3 we found that the values suggested in Bryan et al. (2014) for the over-density parameters are not well suited for this problem. We tested this result also in the case with radiative cooling turned on by performing a single simulation using a threshold in density  $OD = 4$  for level 0 and  $\epsilon_1 = 0$  (see eq. 2.18). The gas temperature distribution after 80 Myrs is shown in Fig. 4.7. The resolution is not high enough for the Kelvin-Helmholtz instability to fully develop and despite its disruption the cloud walks through the hot medium without mixing efficiently. As expected from the previous analysis of this criterion, a better tuning of the parameters is needed in order to describe efficiently the mixing between the two phases. As in chapter 3 we gradually decreased the initial threshold, looking for a convergence of the cold gas temporal evolution. Having established that for the adiabatic simulations a convergence is found for density thresholds below  $OD = 0.1$ , we used this value to perform the first AMR simulation with radiative cooling. It is however important to stress that this density threshold is very impractical: it can only be used in these idealized condition and cannot be applied to other problems,

since it is a slightly higher value than the coronal density in code units.

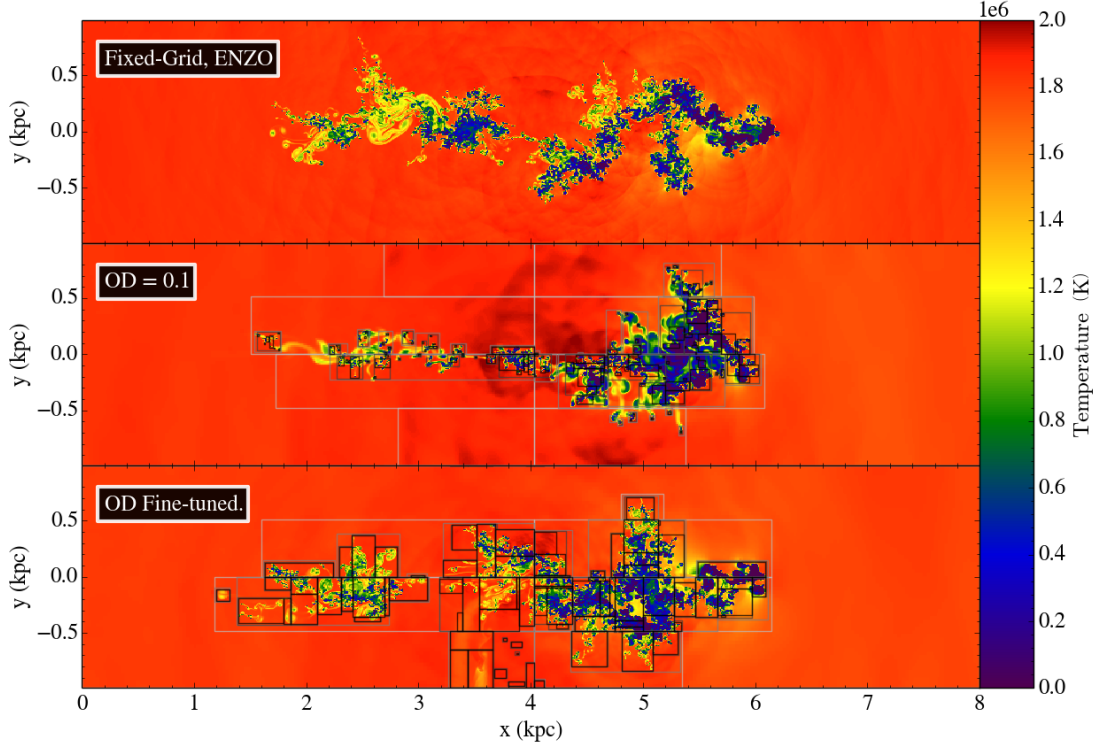


Figure 4.8: Temperature snapshot of the gas distribution after 80 Myrs using the overdensity criterion, compared to the fixed-grid simulation. The upper panel shows the fixed-grid simulation, the one in the middle is the case with overdensity = 0.1, while the label "OD, fine-tuned" refers to the use of the parameter  $\epsilon_1$  (see description in the text).

The next step in the identification of the best set of parameters for the overdensity criterion is the “a posteriori” approach adopted previously for the adiabatic simulations. This method is explained in section 3.3.3, but here we used ATHENA’s density outputs instead of ENZO’s. At any time, the regions we need to describe at high resolution are the head of the cloud and the whole wake that develops during its evolution. As mentioned in section 3.3.3 we determined the density contour that includes such regions from the fixed-grid simulations performed with ATHENA. The selected density value is  $1 \times 10^{-27} \text{ g/cm}^3$  (0.1 in code units). We need to reach the resolution  $2 \text{ pc} \times 2 \text{ pc}$  on those regions of the domain

where the density is higher than  $1 \times 10^{-27} \text{ g/cm}^3$ . Using equation 3.3 we found:  $\epsilon_1 = -1.9996$ . Once we insert this value in equation 2.18, we find, for each level, the corresponding density threshold. The difference between the density thresholds for the highest and the coarsest levels is the same as in section 3.3.3, however one more level is introduced here. This implies that the spread between two density thresholds belonging to two consecutive levels is shortened with respect to the adiabatic case.

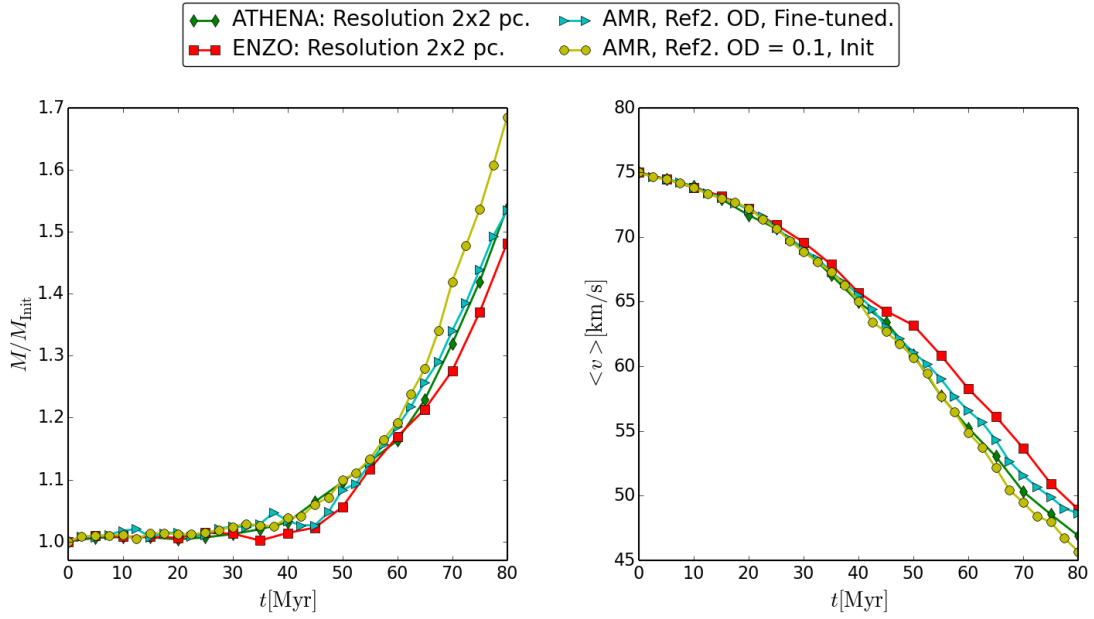


Figure 4.9: Temporal evolution of cold gas mass and mean velocity, for the two implementations of the over-density criterion described in the text.

In fig. 4.8 it is possible to appreciate the great difference in the distribution of grids at different levels between these two implementations of the same criterion. When the over-density parameter is set to 0.1 the grids belonging to the highest level (black rectangles in the figure) cover a small (segmented) fraction of the domain. In particular, the cloud and its wake do not have a high enough resolution to limit numerical diffusion. Most of the wake is in fact at resolution  $16 \text{ pc} \times 16 \text{ pc}$  (white contours); even though small patches at higher resolution can be seen, they are not enough to cover all the relevant regions. The net effect of these

differences is shown in fig. 4.9, where the temporal evolution of the cold gas mass and mean velocity is reported. We can see how the amount of cold gas is always higher when the over-density parameter is set to 0.1, in particular at times later than 60 Myrs, while the mean velocity is systematically underestimated. The fine-tuned implementation instead, gives the overall better agreement with the fixed-grid results obtained with ATHENA. Also, every simulation produces different morphologies for the wake, with the fine-tuned simulation being more similar to the fixed-grid simulations.

As a concluding note in table 4.1, we point out the computational times needed to perform these simulations when they are run on a gnu platform with 8 CPUs. While the density treshold  $OD = 0.1$  helps reducing the overall computational time, the Fine-tuned treshold, following the above discussion, needs much more time to end and there is no real gain with respect to the fixed-grid.

	<b>Fixed-grid</b>	<b>OD = 0.1</b>	<b>OD, Fine-tuned</b>
<b>Computational time</b>	$\sim 100\text{h}$	$\sim 15\text{h}$	$\sim 71\text{h}$

Table 4.1: Computational time needed for fixed-grid and AMR simulations using the two implementations of the over-density criterion described in the text.

### 4.3.2 Other refinement criteria

We have seen that the over-density criterion in its fine-tuned version is effective in describing the evolution of cold gas mass and mean velocity over time. However, the amount of refined cells generated using this approach largely reduces the code performance. As a consequence, the loss in computational time expected by AMR simulations with respect to fixed-grid simulations is not significant enough to extend the analysis to a three-dimensional geometry. Moreover the ad-hoc choice of the treshold parameters makes this setup totally impractical for general purposes. Thus, we search for alternatives, by performing the same simulation with other refinement criteria. In particular, we use the following criteria: Refinement by Normalized Second Derivative and Slope.

## Second-Derivative Criterion

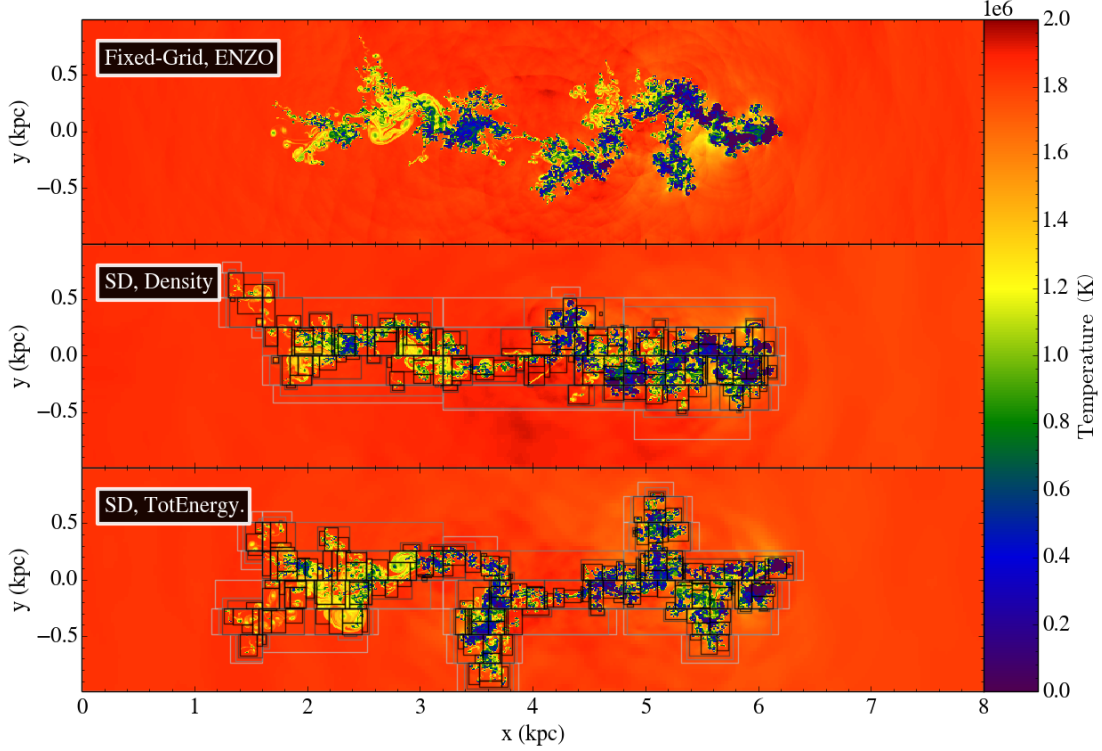


Figure 4.10: Temperature snapshots after 80 Myrs from the start of the simulations, obtained applying the Second Derivative Refinement criterion to Density (mid panel) and Total Energy (bottom panel). The black boxes at the highest resolution ( $2 \text{ pc} \times 2 \text{ pc}$ ) efficiently cover only the wake, while the rest of the domain is left at resolution  $32 \text{ pc} \times 32 \text{ pc}$ . The top panel shows the gas distribution obtained using ENZO as a fixed-grid code.

Following the discussion of this criterion performed in the adiabatic simulations (see section 3.3.5), we applied the Second Derivative Refinement Criterion both to Density and Total Energy, using the new hierarchy of levels adopted here. In fig. 4.10 a morphological comparison of the gas distribution in both cases is presented. The wake is well resolved at maximum resolution, while the rest of the domain is left at resolution  $32 \text{ pc} \times 32 \text{ pc}$ . We point out here, that the parameters used for these simulations are suggested in the online documentation<sup>1</sup>, hence no fine-tuning is required. In these cases too, the distribution of the gas is morphologically

<sup>1</sup><http://enzo.readthedocs.io/en/latest/parameters/hierarchy.html>

different from the fixed-grid simulation and from one another. For instance, when the criterion is applied to the Total Energy, the cold and warm gas is quite extended in the  $y$ -direction, with spurs reaching  $\sim 1$  kpc from the main body of the wake. When the field used for refinement is the density instead, the wake is more compact and confined within 1 kpc on the  $y$ -axis.

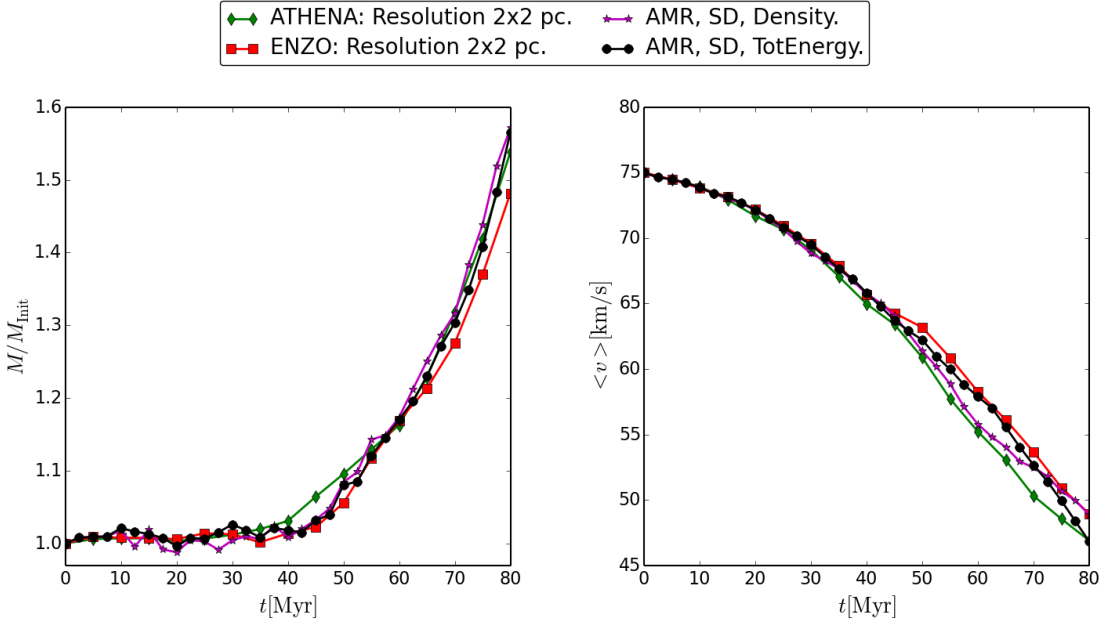


Figure 4.11: Temporal evolution of the cold gas mass and mean velocity as obtained applying the Second Derivative refinement criterion on density (magenta starred line) and Total Energy (black dotted line).

Figure 4.11 shows the temporal evolution of the mass and average velocity of the cold gas over 80 Myrs. Both methods well reproduce the trend obtained with the ATHENA code, while they slightly overestimate (underestimate) the amount of mass (the mean velocity) with respect to ENZO’s fixed-grid evolution.

Despite the high level of accuracy and concordance with the fixed-grid results, this method is unfortunately very expensive from a computational point of view. The computation of the Normalized Second Derivative on each cell of the domain at every timestep requires a long CPU time. In fact, on a 8 CPUs, gnu machine, both these simulations require a computational time  $\sim 70$  h. This is the main obstacle

to an efficient exploitation of the AMR potentialities.

### Slope Criterion

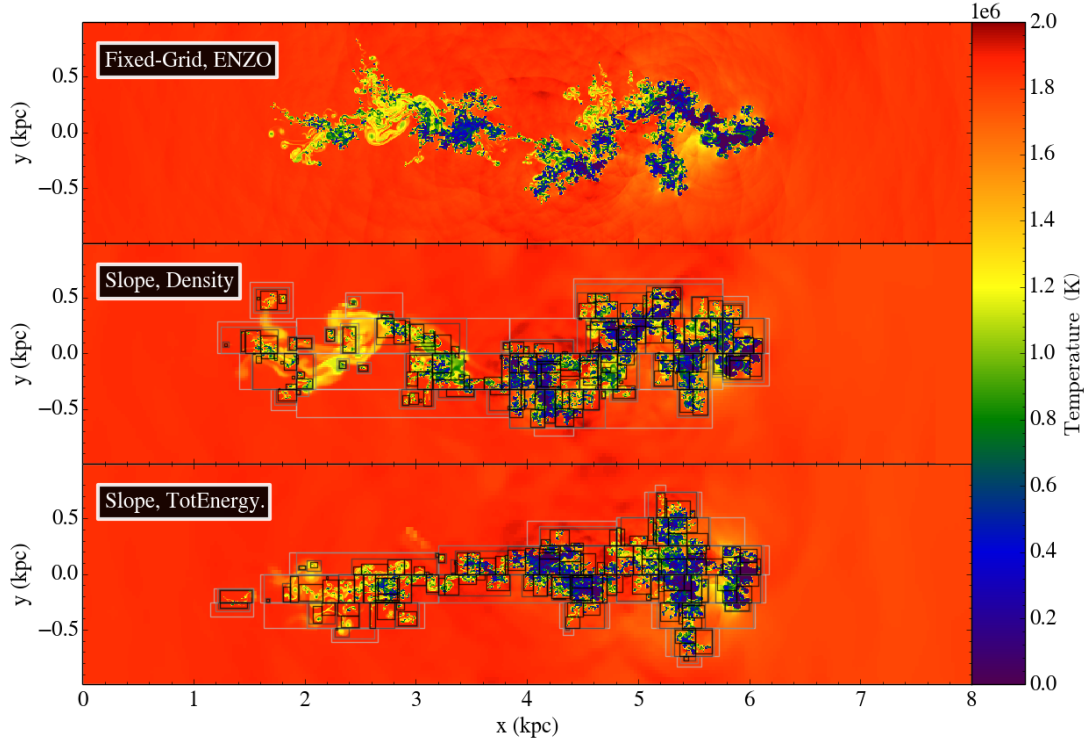


Figure 4.12: Temperature snapshots after 80 Myrs from the start of the simulations, obtained applying the Slope Refinement criterion to Density (mid panel) and Total Energy (bottom panel). The distribution of the high resolution (black) grids accurately covers the relevant regions of the wake, in particular if the Slope Criterion is applied to density. Top panel shows the gas distribution obtained using ENZO as a fixed-grid code.

The Slope criterion can be applied to different fields as well. We chose to follow the previous discussion and took into consideration the density and total energy fields, in order to compare the results obtained using this criterion with the ones found using the Second Derivative criterion. Fig. 4.12 shows a comparison of the gas distribution after 80 Myrs from the start of the simulations, using the density (middle panel) and the Total Energy (low panel) as assigned fields. In both cases, the high resolution ( $2 \text{ pc} \times 2 \text{ pc}$ ) grids are distributed all over the wake of the cloud, and the lower level ones envelope the whole system in a mid resolution patch. The

rest of the domain is left at the lowest resolution ( $32 \text{ pc} \times 32 \text{ pc}$ ).

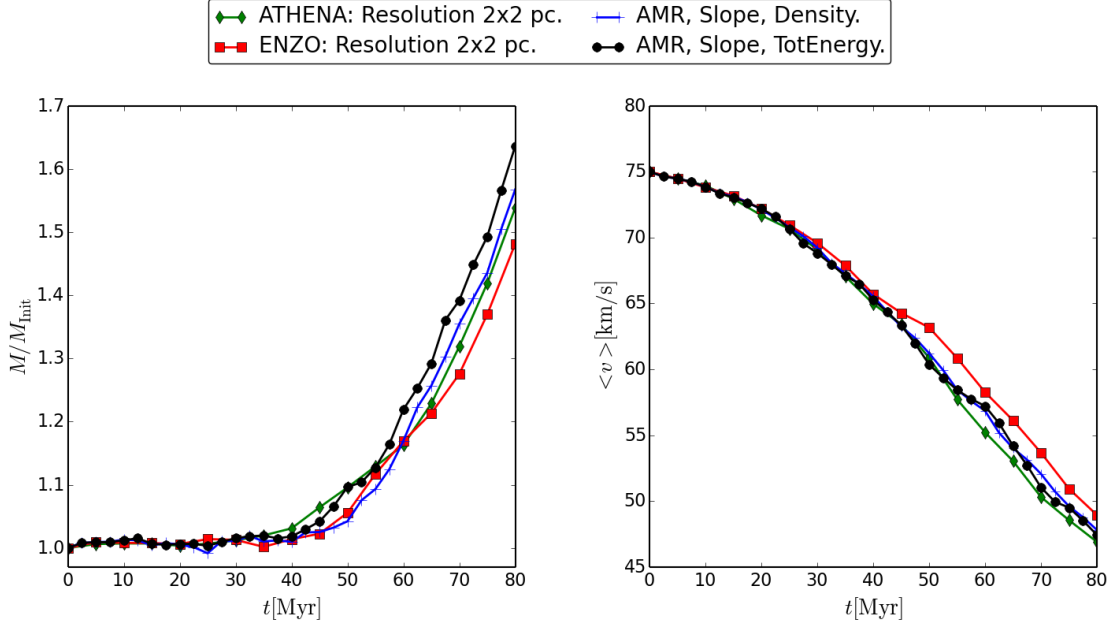


Figure 4.13: Temporal evolution of the cold gas mass and mean velocity as obtained applying the Slope refinement criterion on density (blue line, plus markers) and Total Energy (black dotted line) compared to fixed-grid simulations obtained with ENZO (red line with squares) and ATHENA (green line with diamonds).

A quantitative comparison can be performed by studying the temporal evolution of cold gas mass and velocity (fig. 4.13). When we apply the Slope criterion to the total energy, the cold gas mass is systematically overestimated during the whole evolution of the cloud, while its application to density guarantees a much better resemblance to the profile obtained with fixed-grid simulations. Both simulations require a computational time  $\sim 36\text{h}$  to complete.

### 4.3.3 Comparison between Refinement criteria

The results obtained in the previous sections can now be compared in order to find the criterion that more than any other guarantees a low computational cost and accuracy for our problem. As briefly pointed out previously, the morphology of the wake is very sensitive to changes in setup of the simulations. As an example, in fig.

4.14 we report the morphological comparison of the AMR simulations performed using the Slope criterion applied to density on two different computers, both using gnu libraries and compilers (different versions of the compilers are implemented on each machine).

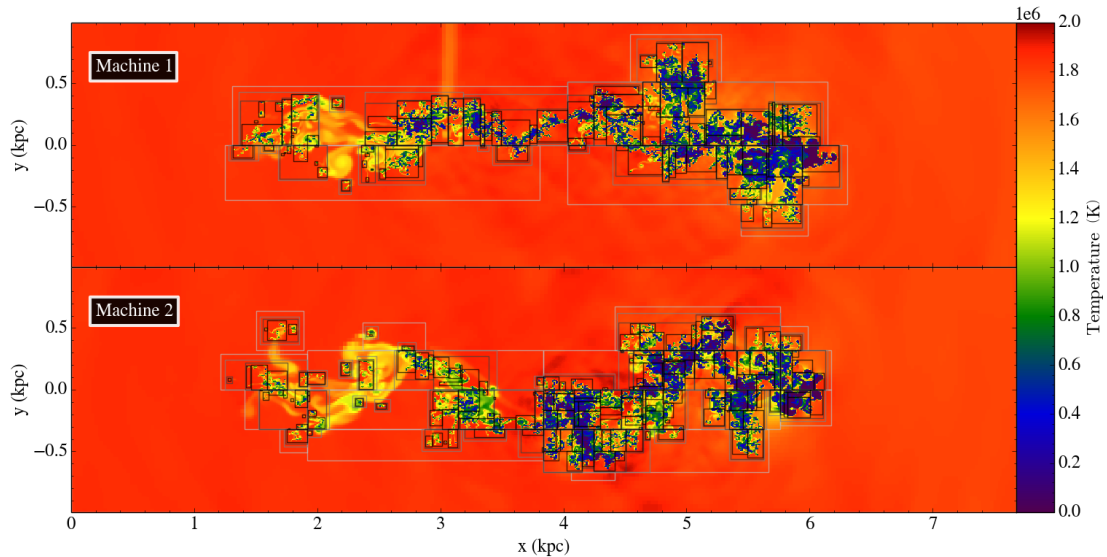


Figure 4.14: Temperature snapshot after 80 Myrs from the start of the simulation. Panels are obtained running the simulation on two different 8CPUs, gnu machines.

This result is also found when other refinement criteria are used. Due to this feature, we can not infer any constraint on the morphology of the wake. However, if we consider the evolution of the cold gas mass and velocity, performing the same simulation on different machines we can estimate the typical computational error in our simulations. The determination of this error gives a constraint on the uncertainties in the results obtained also with different criteria. In fig. 4.15 the temporal evolution of the mass and mean velocity of cold gas are shown for each refinement criterion. In particular, on each row the left panel shows the evolution of the cold gas mass, while the right panel shows its mean velocity, obtained using the criterion on two different machines (blue dotted and cyan starred lines). Both machines use gnu libraries and compilers (different versions of the compilers are implemented on each machine); the simulations are performed on 8 CPUs both on machine 1 and on machine 2.

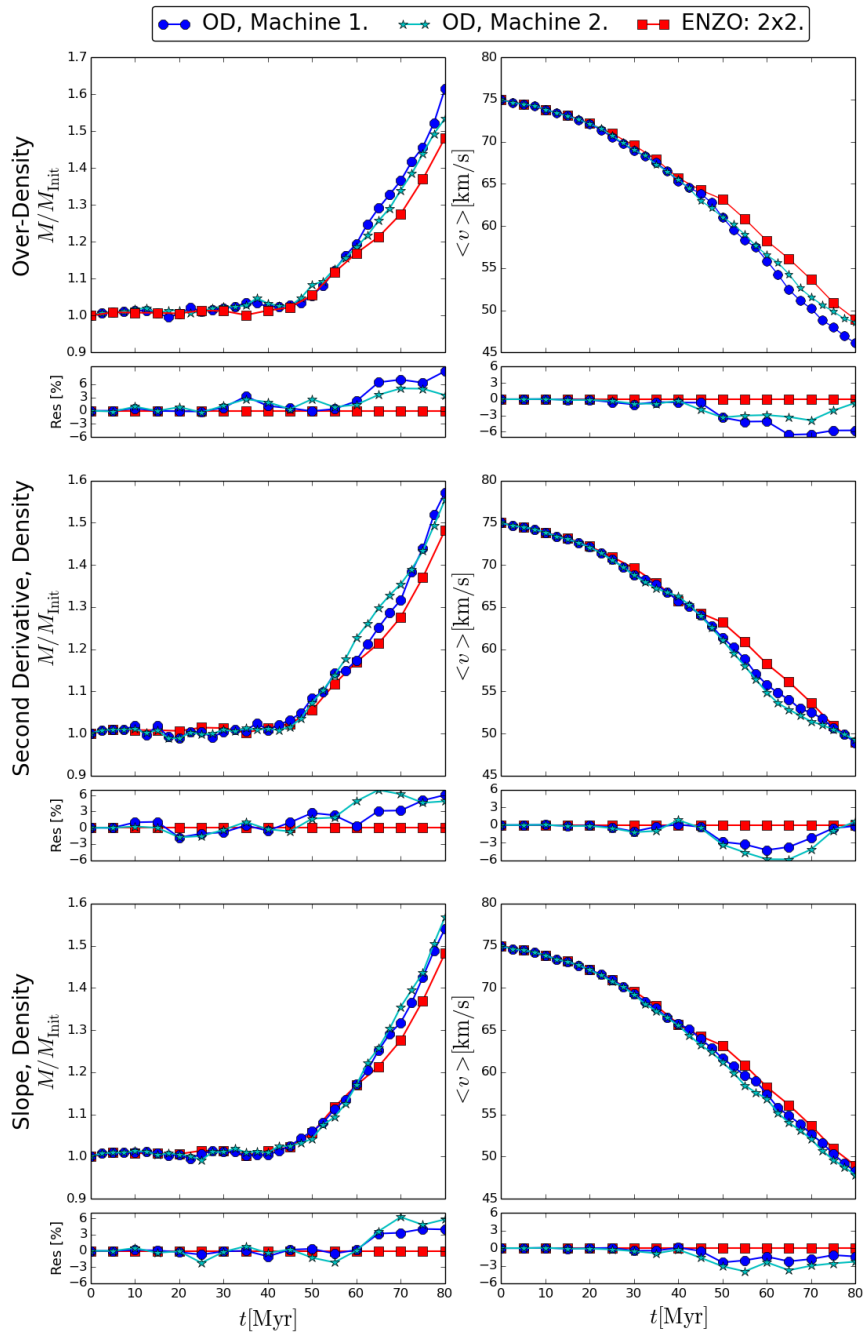


Figure 4.15: Results of the AMR simulations performed on two different machines using the OD Fine-tuned, the Second Derivative and the Slope criteria (from top to bottom); the red squares are the results obtained with ENZO fixed-grid. Both machines use 8 CPUs and gnu libraries and compilers. Below each panel we show the residuals of each simulation with respect to the fixed-grid one.

Below each left and right panel, in fig. 4.15 we plotted the residuals of these two simulations with respect to the fixed-grid one at resolution  $2 \text{ pc} \times 2 \text{ pc}$  obtained with ENZO (red line, squared markers). The first column shows the temporal evolution of the cold gas mass for the adopted criteria, using their best setup. The second column instead shows the temporal evolution of the cold gas mean velocity in each case. It is not possible to identify a common feature in the comparison between the simulations run on the two machines, thus we conclude that the spreads between the curves are due to random computational effects. The scatter between the AMR results is at most 5 percent. In the following we use this value as a measure of the intrinsic uncertainties of all simulations rms. Thus, AMR simulations diverging by less than 5% from the fixed-grid results will be accepted as a valid representation of the cloud evolution.

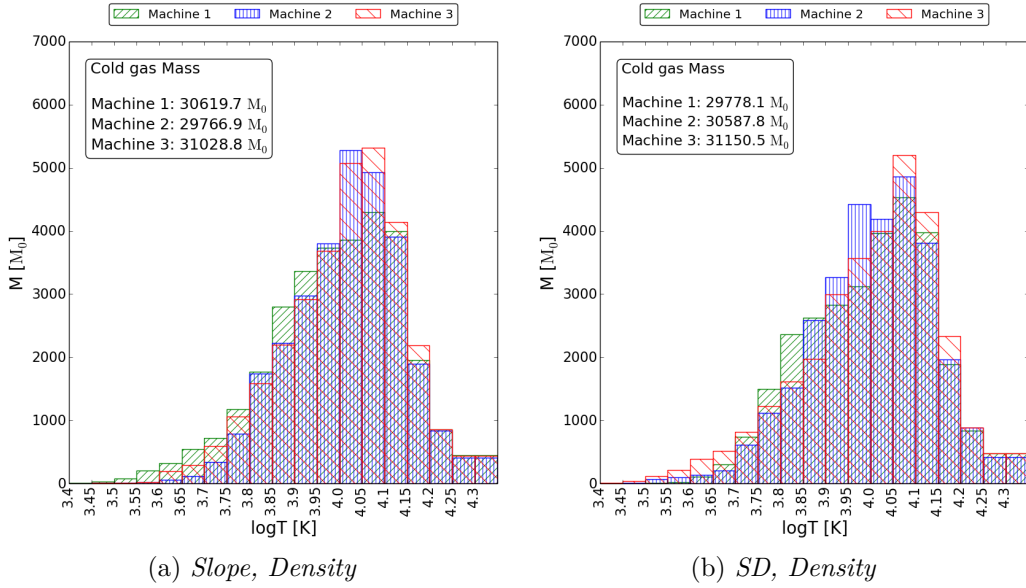


Figure 4.16: Cold gas mass distribution as a function of temperature for the AMR simulations obtained using the Slope (left panel) and Second Derivative (right panel) criteria, on different machines. All machines use different versions of gnu libraries and compilers. Simulations are run on 8 CPUs on machine 1 and 2, while on machine 3, 24 CPUs have been used. Machine 3 is the Intel OmniPath Cluster MARCONI, developed by CINECA and Lenovo, whose access has been granted after acceptance of a class C proposal (approved project: HP10CZMLU1).

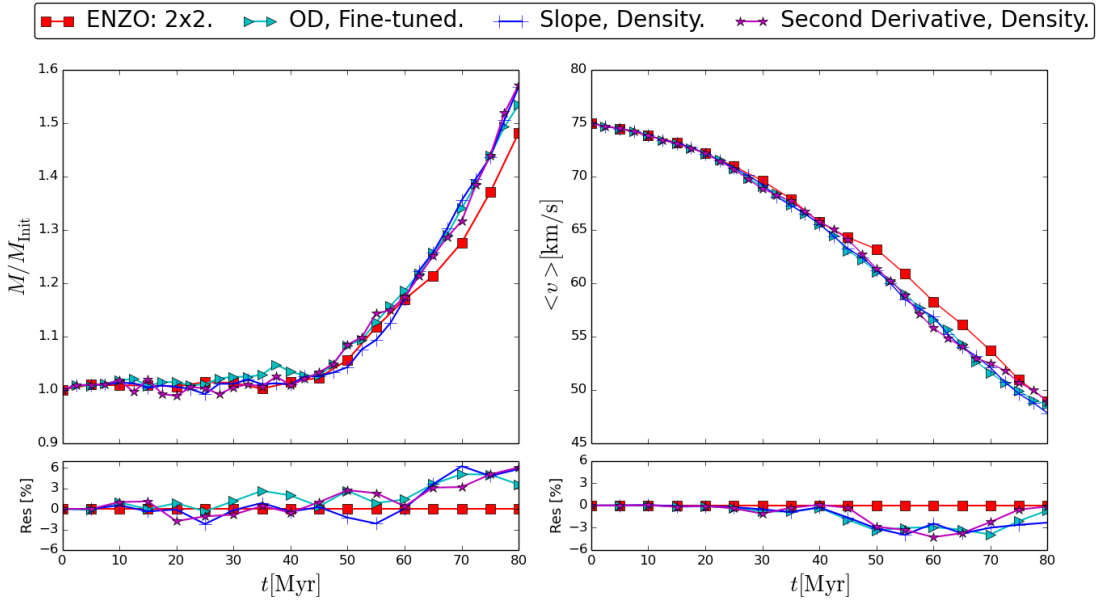


Figure 4.17: Cold gas mass and mean velocity temporal evolution obtained for each efficient refinement criterion described in this chapter. Below each panel the residuals with respect to the ENZO fixed-grid dimulation are shown.

Another evidence of the difference between same simulations when they are run on different machines is the cold gas mass distribution over temperature. Fig. 4.16 shows the mass distribution of the cold ( $T < 2 \times 10^4$  K) gas as a function of temperature with histograms, after 70 Myrs for the slope and second derivative criteria obtained with different machines. All machines use gnu libraries and different versions of compilers. In particular, machine 3 is the Intel OmniPath Cluster MARCONI<sup>2</sup>. On the top left corner, the cold gas mass is appointed (in solar masses) for each machine. After 70 Myrs the gas distribution is slightly different for each machine. In particular, for the Slope case, on machine 1 the cold gas mass distribution is less peaked at temperatures  $T \sim 10^4 - 10^{4.15}$  K, while the tail at lower temperatures is higher. This feature is present also in the Second Derivative case, even if less accentuated. The distribution of the cold gas mass on machines 2 and 3 is similar in both cases, even though the peak at  $T \sim 10^4$  K is wider on machine 2 when the Second Derivative criterion is used. At tempera-

<sup>2</sup>The access to this computer cluster has been granted by the CINECA facility through the submission and acceptance of the class C proposal HP10CZMLU1.

tures  $T > 10^{4.1}$  K (beyond the peak), machine 3 has a mass excess with respect to machines 1 and 2, independently on the criterion used.

Finally, from figure 4.17 the temporal evolution of the cold gas mass and mean velocity can be appreciated, as obtained using the best refinement criteria described in this chapter. Despite the usual overestimation of condensed gas with respect to the fixed-grid simulation obtained with ENZO, the discrepancy between the rms is roughly 5 %. Thus, each one of the simulations here shown can be considered equally valid to represent the cloud's evolution. In particular, given the low computational time needed by the Slope criterion with respect to the other criteria, we conclude that the density slope criterion is the best AMR setup for our problem.

## 4.4 3D simulation

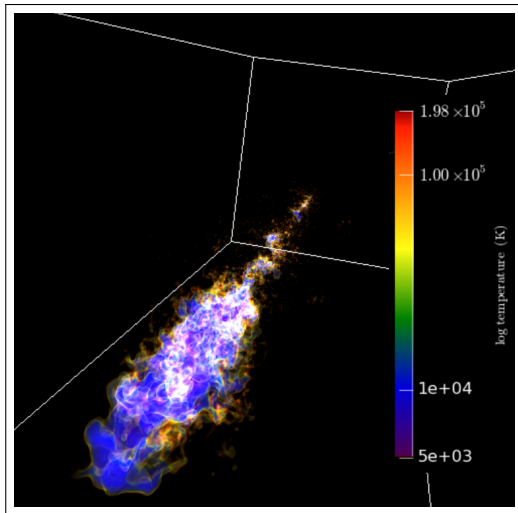


Figure 4.18: 3D prospective render of the distribution of gas at  $T < 5 \times 10^5$  K after 60 Myrs. The camera is set at the head (lower left) of the cloud pointing towards the wake.

Having found the best refinement criterion in terms of accuracy and speed, we extended the study of a fountain cloud moving through the MW's corona to a 3D geometry, in order to better understand the phenomenon in a more realistic environment. As for the 2D case, we set the coarsest resolution to  $(32 \text{ pc})^3$  and four levels of refinement are permitted, reaching the highest resolution at  $(2 \text{ pc})^3$ . As discussed in chapter 3, in a 2D geometry, the problem is studied as an infinite cylinder moving along the perpendicular direction to its major axis. The results are then related to a 3D geometry multiplying the mass by the factor  $4/3R_{cl}$ , where  $R_{cl}$  is the initial radius of the cloud. In the three-

dimensional representation the cloud is initially spherical and the mass of the cold gas is obtained at any time by multiplying each cell's density by its volume.

A larger contact surface between the cloud and the hot coronal gas in the 3D case

implies a faster development of KH instabilities. We expect that a quicker mixing between the two gas phases triggers a larger condensation of the coronal material. Fig. 4.18 shows a render visualization of the gas distribution after 60 Myrs from the start of the cloud motion. The whole structure is observed from the head of the cloud at the lower left of the image, looking back to the wake and we overplot the colormap. The wake is less extended along the  $y$ - and  $z$ - directions, with respect to the 2D case.

In fig. 4.19 and 4.20 we present the distribution of gas at different times for our 3D, AMR, high resolution simulation using the Slope criterion applied to density. Fig. 4.19 is obtained by slicing the temperature dataset at  $z = 0$ . Fig. 4.20 is instead a projection of the temperature field, for the only gas at temperature  $T < 2 \times 10^4$  K. The spatial distribution of the grids can be seen in fig. 4.19. Exception made for the downstream of the wake, the Slope criterion seems to accurately follow the evolution of the cloud during its motion through the hot coronal medium: the majority of the relevant regions are enveloped in grids at resolution  $(2 \text{ pc})^3$ . The spatial distribution of the warm and cold gas is much more limited, at any time, on the  $y$ -axis with respect to the 2D simulations, as previously noted on fig. 4.18 shows.

Fig. 4.20 shows a projection on the  $z$ -axis of the spatial distribution of the gas at  $T < 2 \times 10^4$  K. The clumpy nature of the cold gas in the wake can be seen, starting from 20 Myrs. In particular after 60 Myrs, when the cloud is almost completely disrupted, the wake seems to be populated with cold structures of sizes ranging from a few to tens of parsecs.

The quantitative results of the 3D simulation are shown in fig. 4.21 compared to the 2D fixed-grid simulations obtained with ENZO and ATHENA. As expected, the condensation of the coronal gas onto the wake of the cloud is extremely efficient, and the mass of cold gas increases over time much more than in the 2D case. After 60 Myrs, the cold gas has increased its mass of a 30% with respect to the initial cloud's mass, instead of the 17% found with the AMR, applying the Slope criterion to density, and the fixed-grid simulations performed with ENZO. As for the mean velocity, the 3D simulation lies between the profile determined with ATHENA and with ENZO. Thus, the mean velocity is not greatly sensitive to changes in the distribution and mass of the cold gas.

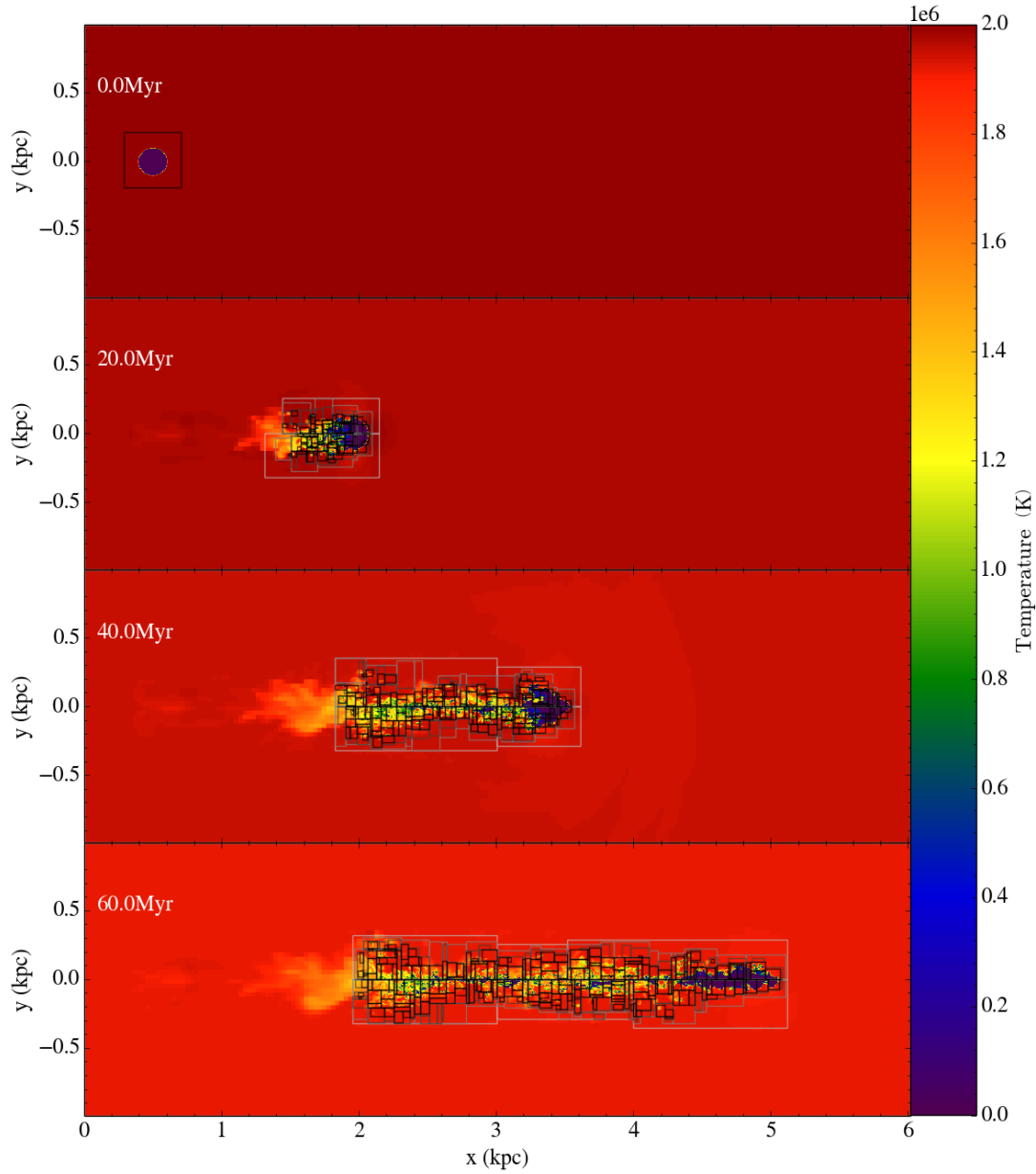


Figure 4.19: Slice at  $z = 0$  of the temperature field at different times obtained from a 3D simulation with ENZO, using the Slope criterion applied to density. We overplot the grids. The distribution of the high resolution (black) grids covers the whole wake except for the extreme left part at every time. Lower resolutions grids (lighter grey) envelope the whole system during its evolution.

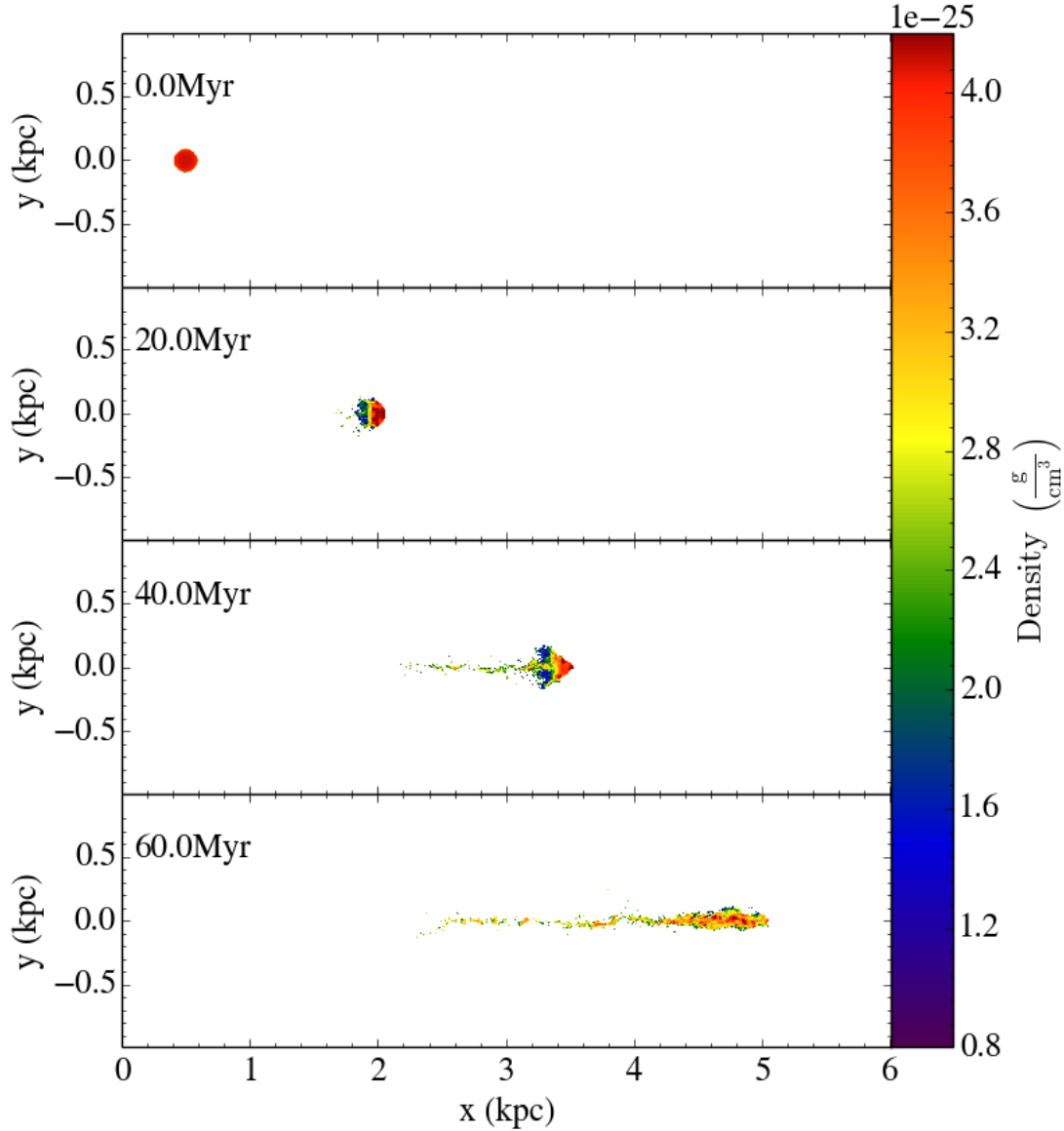


Figure 4.20: Projection on the  $z$ -axis of the density field at different times obtained from a 3D simulation with ENZO, using the Slope criterion applied to density. Only the cold ( $T < 2 \times 10^4$  K) gas density is shown here.

We conclude that, in order to study the mixing occurring within a two phases gas it is essential to perform three-dimensional simulations, only obtainable using AMR techniques. In particular we do find that, using the AMR code ENZO, the most convenient refinement criterion for such studies is the Slope criterion applied

to density, that guarantees both accuracy and computational speed.

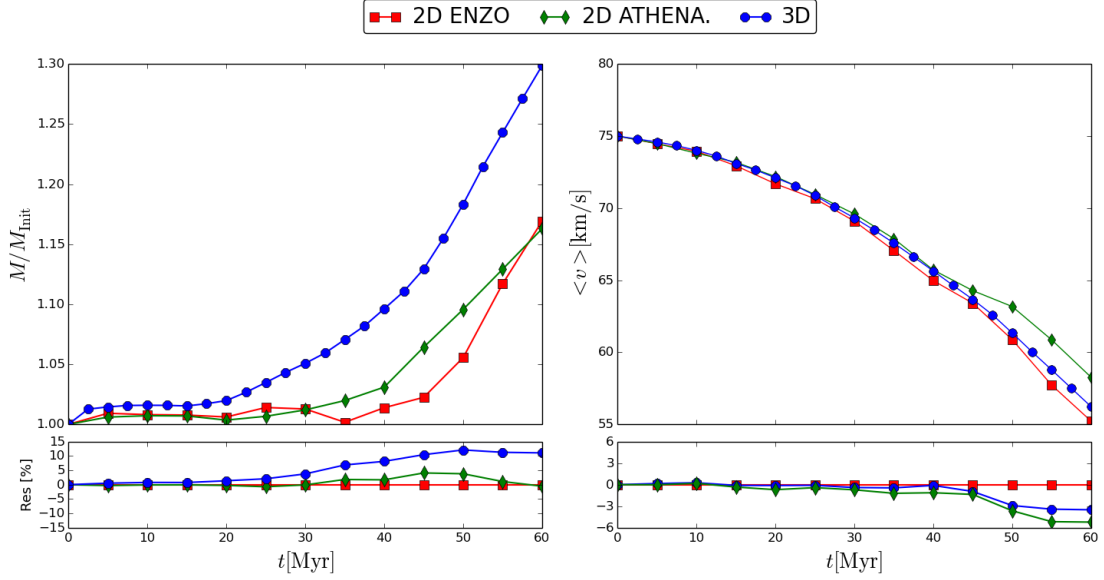


Figure 4.21: Temporal evolution of the cold gas mass and mean velocity obtained with the 3D simulation and compared to the 2D fixed-grid results. The condensation estimated using the 3D simulation is  $\sim 30\%$  the initial mass of the cloud, almost double with respect to the 2D simulations. For each panel, the residuals with respect to the ENZO, fixed-grid simulation at resolution  $2 \text{ pc} \times 2 \text{ pc}$  are shown.

The 3D simulation of a galactic fountain cloud moving through a MW’s corona, gives an estimate of condensation much higher than the one found using 2D fixed-grid and AMR simulations. The increase in the contact surface between the cloud and the coronal gas, enhances the interaction between the two fluids, fastening the development of the K-H instability, thus the efficiency of mixing. Our investigation showed that a cold cloud, of initial mass  $2 \times 10^4 M_{\odot}$  and radius 100 pc, in 60 Myrs, can accrete 30% of its mass, from the coronal gas via condensation, largely correcting the previous estimates of such phenomenon.



# Conclusions

The galactic fountain mechanism consists in the ejection of cold clouds from the galaxy discs as a consequence of stellar feedback and supernova explosions (e.g. Bregman (1980); Melioli et al. (2009)). Once ejected, the clouds move through the hot corona surrounding Milky Way-type galaxies, mixing and accreting mass from such medium. After a typical orbital time of 100 Myrs, the clouds fall back onto the disc, refurbishing it of cold gas to sustain its star formation. In the Milky Way, an observational evidence for this mechanism are the distribution of Intermediate Velocity Clouds (IVCs): cold, almost solar metallicity clouds (Wakker et al. 2004) and the kinematics of the extraplanar gas (Marasco et al. 2012; Fraternali et al. 2013).

In this Thesis we performed high resolution ( $2 \text{ pc} \times 2 \text{ pc}$ ) hydrodynamical simulations of cold ( $T = 10^4 \text{ K}$ ) galactic fountain clouds moving through a hot ( $T = 2 \times 10^6 \text{ K}$ ) corona, using a parallel, (magneto-) hydrodynamical, Adaptive-Mesh Refinement (AMR) code: ENZO (Bryan et al. 2014). Up until today, only simulations using fixed-grid codes had been performed and only in 2D, given that the computational time needed by such codes to perform 3D simulations would have been prohibitive. The advantage of using an AMR code resides in its automatic refinement of regions where certain desired criteria are satisfied and allows to cut down on computational times.

We performed two different sets of simulations:

- **Adiabatic simulations** (chapter 3). When radiative cooling is not included in the code, the interaction between the cloud and the coronal gas is purely a Kelvin-Helmholtz (KH) instability. The development of this instability generates a turbulent warm wake, behind the cloud, constituted of gas at

intermediate temperatures between those of the cloud and the corona. Due to this interaction, after 60 Myrs the cloud is partially evaporated, while its head is flattened perpendicularly to the cloud's motion, due to ram pressure. We studied the distribution of cold gas mass and average velocity as a function of time in simulations run with different refinement criteria. The comparison with results obtained with fixed-grid codes allowed us to identify the best suited criterion for our problem. We found that the widely used over-density criterion performs very poorly as it requires highly impractical values for the density threshold. The best criterion is the Slope applied to density, which is based on the evaluation of the spatial gradient of density along each adjacent cell. Moreover, we found that it is essential to define a high resolution ( $2 \text{ pc} \times 2 \text{ pc}$ ) grid covering the cloud as initial condition of the simulations.

- **Simulations with radiative cooling** (chapter 4). In order to compare the results on the condensation of the coronal gas onto the wake of the clouds obtained with fixed-grid simulations (Armillotta et al. 2016), the same implementation of radiative cooling has been introduced in the ENZO code (chapter 2). At every timestep, the cooling rates at a cell's temperature are read from an input table and the energy subtraction due to this phenomenon is performed in sub-cycles at temporal resolution  $\Delta t_{Cool} = 10\% \min(t_{Cool})$ , where the  $\min()$  is taken over all the cells. Due to the difference in the temporal resolution of the hydrodynamics with the code ATHENA (whose results are used for comparison) we looked for a Courant-Friedrichs-Lewy parameter that allowed a convergence, finding the best compromise for  $k_{CFL} = 0.1$ . This configuration has been used to perform AMR simulations (at highest resolution  $2 \text{ pc} \times 2 \text{ pc}$ ) using different refinement criteria. We confirmed that the Slope criterion is also in this case the best option for this kind of simulations. The agreement with previous works is solid out to 60 – 80 Myrs of evolution and a similar value for condensation has been found of  $\sim 20\%$  of the initial mass of the cloud. The computational times are reduced of a factor  $\sim 3$  with respect to fixed-grid simulations.

Finally, an AMR (reaching highest resolution  $2 \text{ pc} \times 2 \text{ pc}$ ), three-dimensional simulation has been performed using the Slope criterion for refinement applied to density, with an initial high resolution box enveloping the cloud. We found that in 3D the spatial distribution of the cold gas is far more limited on the y- and z-axes with respect to the 2D case. The clumpy structure of the cold gas in the wake is confirmed and a new, more realistic, value for the condensation has been found after 60 Myrs: 30% of the initial mass of the cloud is accreted through condensation of the coronal gas in the cloud's wake. This result may have important consequences in our understanding of the interaction between galactic discs and their surrounding environment and of the role of gas accretion in the evolution of spiral galaxies.

## Future perspective

The above discussion is affected by some simplifications. First of all, an average half-solar metallicity is assumed for both the fluids. The coronal gas, is expected to have low ( $0.1 - 0.3$  Solar) metallicity, while the typical metallicities of IVCs is almost solar. An implementation of a two-metallicity problem has been performed in the adiabatic case, but we did not extend this modification to the simulations including radiative cooling.

Moreover, the effect of heating due to photoionization is also not taken into account here. The two main sources of heating are the cosmological background and the photoionizing flux coming from the disc. This phenomenon is expected to partially neutralize the effect of condensation due to radiative cooling. A proper treatment of heating in this kind of simulations will be crucial to quantify the condensation at the disc-corona interface and investigate its role for gas accretion and the feeding of star formation in MW-type galaxies.



# Acknowledgments

Two people, more than anyone else, helped me walking through the development of this work.

First of all my supervisor Filippo Fraternali, who has given me the strength and motivation to sustain the different challenges occurred in this experience throughout the last year. His attention to details taught me the importance of accuracy and precision, while his contagious passion for astrophysics is a guiding light I will do my best not to lose sight. I am also very thankful to him for having given me the opportunity to participate to the *Crossing the Rubicon* conference in September as a LOC member: as a Master student it has been a unique and fascinating opportunity.

Secondly, this work wouldn't have been possible without the thoughtful assistance of my co-supervisor, Lucia Armillotta. Both her kindness and her knowledge, helped me greatly to overcome the recurrent technical issues of this project. Also, I am very thankful for the time she dedicated to the reading of this Thesis despite the great distance and the new experience she just started.



# A chi mi ha sopportato

Ho avuto la fortuna di nascere in un paese in cui l'istruzione è valorizzata ed incentivata, in cui la cultura ha un valore e la storia non viene dimenticata ma, checchè se ne dica, presa ad esempio per la costruzione di un futuro migliore. In questo contesto, la mia famiglia ha sempre fatto di tutto per concedermi l'onore di proseguire gli studi, non solo in ambito universitario, ma anche nel mondo musicale. Temo che senza il senso di dovere che i miei genitori hanno cercato di tramandarmi, questo lavoro non sarebbe stato possibile. Devo perciò ringraziarli per avermi permesso di arrivare al termine di questa avventura. Un grosso ringraziamento va anche ai miei fratelli, spesso usati come salvagente nelle situazioni più difficili.

Non posso non ringraziare il professor Marco Bellini per gli insegnamenti, non solo musicali, che mi ha trasmesso in questi anni di conservatorio, nonché la classe di tromba dell'Istituto Musicale "G. Lettimi" di Rimini con la quale ho condiviso la bellezza del suonare insieme.

Se sono stato in grado di vivere quest'esperienza come un'"avventura" lo devo essenzialmente allo scoutismo, fondamentale nella mia vita fino a questo momento. In particolare il merito è di tutte le persone al cui interno ho imparato a conoscere e ad amare e che hanno sempre creduto nelle mie potenzialità. Terrò sempre a cuore questi anni da capo, vissuti nella condivisione delle gioie e delle difficoltà. "Guida da te la tua canoa" diceva BP ed anche se questa magnifica esperienza è giunta al termine, spero che un giorno questo mio saluto si convertirà in un ritrovo, fino ad allora "Buona strada"!

Sebbene io sia un romagnolo DOC, la mia famiglia non ha limiti regionali e si estende ben al di là del legame genetico. Mi riferisco ai miei compagni di viaggio universitari, sui quali so di poter contare in ogni situazione, come è stato fino ad ora. In ciascuno di voi ho trovato un confidente e sebbene le nostre strade stiano lentamente divergendo le une dalle altre, so che non ci perderemo mai.

Dedico questo lavoro a te Alyx. A te che mi hai spronato a seguire i miei sogni ed a spendermi fino in fondo per raggiungerli. A te che mi hai insegnato a guardare oltre il mio piccolo mondo, mostrandomi strade che da solo avrei ritenuto impossibili da percorrere. A te che hai raccolto le mie delusioni e te ne sei fatta carico. *Truely. . . Deeply. . . Thank you.*



# List of Tables

2.1	CellFlaggingMethod parameter. . . . .	32
3.1	Parameters initialization. . . . .	41
3.2	Limit densities per level. . . . .	46
3.3	Adiabatic AMR 32 pc: Limit densities per level. . . . .	51
3.4	Adiabatic AMR 32 pc: Limit densities per level, bis. . . . .	53
3.5	Computational time . . . . .	61
4.1	Computational time . . . . .	76



# List of Figures

1.1	NGC1961 and NGC6753 X-Ray surface brightness . . . . .	8
1.2	NGC 891: H I emission . . . . .	9
1.3	HVCs spatial distribution . . . . .	12
1.4	Cold mode accretion simulations . . . . .	13
1.5	Galactic Fountain representation . . . . .	16
2.1	Eulerian vs. Lagrangian approach. . . . .	20
2.2	Refinement algorithm. . . . .	27
2.3	Hierarchy illustration. . . . .	27
2.4	Timestep evolution . . . . .	29
2.5	Cooling function . . . . .	36
3.1	NoAMR Adiabatic expansion. . . . .	42
3.2	NoAMR Adiabatic expansion's results. . . . .	44
3.3	Adiabatic overdensity test . . . . .	47
3.4	Adiabatic AMR 40 pc: cold gas mass and velocity curves. . . . .	48
3.5	NoAMR zoom. . . . .	50
3.6	Adiabatic AMR 32 pc: cold gas mass and velocity curves. . . . .	51
3.7	Adiabatic AMR 32 pc: contours. . . . .	52
3.8	Adiabatic AMR 32 pc: Cold gas mass and velocity curves, $\epsilon_t$ . . . . .	54
3.9	Adiabatic AMR, initial setup. . . . .	55
3.10	Adiabatic AMR, initial setup, 60 Myrs. . . . .	55
3.11	Adiabatic AMR, initial setup, Results. . . . .	56
3.12	AMR OD, initial setup: Mass . . . . .	57
3.13	Temperature snapshots, Initial Box . . . . .	57
3.14	AMR OD, initial setup: Velocity . . . . .	58
3.15	Results for both of SecondDerivative tests. . . . .	60
3.16	Adiabatic best criteria comparison . . . . .	61
3.17	Adiabatic best criteria morphological comparison . . . . .	62
4.1	Cooling and adiabatic morphologic comparison . . . . .	66

4.2	Comparison of four simulations at different resolutions. . . . .	68
4.3	Cold gas mass and velocity for simulations at different resolutions .	68
4.4	NoAMR Results, CFL parameter comparison . . . . .	70
4.5	NoAMR ENZO vs. ATHENA . . . . .	71
4.6	Temporal evolution of the system, Cooling case . . . . .	72
4.7	OD = 4, Cooling . . . . .	73
4.8	Over-density comparison, cooling . . . . .	74
4.9	Over-density, results . . . . .	75
4.10	Gas distribution comparison, Second Derivative . . . . .	77
4.11	Second Derivative Cold gas temporal evolution . . . . .	78
4.12	Gas distribution comparison, Slope . . . . .	79
4.13	[Slope, Cold gas temporal evolution . . . . .	80
4.14	Morphological comparison, Slope . . . . .	81
4.15	Results, Hardware comparison . . . . .	82
4.16	Cold gas mass distribution with temperature . . . . .	83
4.17	Reults best criteria . . . . .	84
4.18	3D simulation, 60 Myrs . . . . .	85
4.19	Temperature slice on z-axis of the 3D simulation . . . . .	87
4.20	Temperature projection of the 3D simulation . . . . .	88
4.21	Results 3D simulation . . . . .	89

# Bibliography

- Anderson, J. 1995, *Computational Fluid Dynamics, Computational Fluid Dynamics: The Basics with Applications* (McGraw-Hill Education)
- Anderson, M. E. & Bregman, J. N. 2010, *ApJ*, 714, 320
- Anderson, M. E. & Bregman, J. N. 2011, *ApJ*, 737, 22
- Armillotta, L., Fraternali, F., & Marinacci, F. 2016, *MNRAS*, 462, 4157
- Balsara, D. S. & Spicer, D. S. 1999, *Journal of Computational Physics*, 149,2, 270
- Bauermeister, A., Blitz, L., & Ma, C.-P. 2010, *ApJ*, 717, 323
- Binney, J. 1977, *ApJ*, 215, 483
- Binney, J., Nipoti, C., & Fraternali, F. 2009, *MNRAS*, 397, 1804
- Bogdán, Á., Forman, W. R., Kraft, R. P., & Jones, C. 2013a, *ApJ*, 772, 98
- Bogdán, Á., Forman, W. R., Vogelsberger, M., et al. 2013b, *ApJ*, 772, 97
- Boomsma, R., Oosterloo, T. A., Fraternali, F., van der Hulst, J. M., & Sancisi, R. 2008, *A&A*, 490, 555
- Bregman, J. N. 1980, *ApJ*, 236, 577
- Bregman, J. N. 2007, *ARA&A*, 45, 221
- Bregman, J. N., Alves, G. C., Miller, M. J., & Hodges-Kluck, E. 2015, *Journal of Astronomical Telescopes, Instruments, and Systems*, 1, 045003
- Bregman, J. N. & Lloyd-Davies, E. J. 2007, *ApJ*, 669, 990
- Brüns, C., Kerp, J., Kalberla, P. M. W., & Mebold, U. 2000, *A&Ap*, 357, 120
- Bryan, G., Norman, M. L., Stone, J. M., Cen, R., & Ostriker, J. P. 1995, *Computer Physics Communications*, 89,149

- Bryan, G. L., Norman, M. L., O'Shea, B. W., et al. 2014, *ApJS*, 211, 19
- Colella, P. & Woodward, P. R. 1984, *Journal of Computational Physics*, 54, 174
- Dedner, A., Kemm, F., Kröner, D., et al. 2002, *Journal of Computational Physics*, 175,2, 645
- Del Zanna, L., Zanotti, O., Bucciantini, N., & Londrillo, P. 2007, *A&A*, 473, 11
- Fraternali, F. & Binney, J. J. 2006, *MNRAS*, 366, 449
- Fraternali, F. & Binney, J. J. 2008, *MNRAS*, 386, 935
- Fraternali, F., Marasco, A., Armillotta, L., & Marinacci, F. 2015, *MNRAS*, 447, L70
- Fraternali, F., Marasco, A., Marinacci, F., & Binney, J. 2013, *ApJl*, 764, L21
- Fraternali, F., Oosterloo, T., Sancisi, R., & van Moorsel, G. 2001, *ApJl*, 562, L47
- Fraternali, F. & Tomassetti, M. 2012, *MNRAS*, 426, 2166
- Fraternali, F., van Moorsel, G., Sancisi, R., & Oosterloo, T. 2002, *Aj*, 123, 3124
- Fukugita, M. & Peebles, P. J. E. 2006, *ApJ*, 639, 590
- Gaensler, B. M., Madsen, G. J., Chatterjee, S., & Mao, S. A. 2008, *PASA*, 25, 184
- Gardiner, T. A. & Stone, J. M. 2005, *J. Comput. Phys.*, 205, 509
- Grcevich, J. & Putman, M. E. 2009, *ApJ*, 696, 385
- Gupta, A., Mathur, S., Krongold, Y., Nicastro, F., & Galeazzi, M. 2012, *ApJl*, 756, L8
- Heitsch, F. & Putman, M. E. 2009, *ApJ*, 698, 1485
- Hobbs, A., Read, J., Power, C., & Cole, D. 2013, *MNRAS*, 434, 1849
- Iaconi, R., Reichardt, T., Staff, J., et al. 2016, *MNRAS*
- Joung, M. R., Putman, M. E., Bryan, G. L., Fernández, X., & Peek, J. E. G. 2012, *ApJ*, 759, 137
- Kalberla, P. M. W., Burton, W. B., Hartmann, D., et al. 2005, *A&Ap*, 440, 775
- Kaufmann, T., Mayer, L., Wadsley, J., Stadel, J., & Moore, B. 2006, *MNRAS*, 370, 1612

- Kereš, D., Katz, N., Fardal, M., Davé, R., & Weinberg, D. H. 2009, *MNRAS*, 395, 160
- Kim, J.-h., Agertz, O., Teyssier, R., et al. 2016
- Komatsu, E., Dunkley, J., Nolta, M. R., et al. 2009, *ApJs*, 180, 330
- LeVeque, R. J. 2002, *Finite Volume Methods for Hyperbolic Problems* (Cambridge University Press)
- Lucero, D. M., Carignan, C., Elson, E. C., et al. 2015, *ArXiv e-prints*
- Luo, Y., Nagamine, K., & I. Shlosman. 2016, *MNRAS*, 459, 3217
- Löhner, R., Morgan, K., Peraire, J., & Vahdati, M. 1987, *International Journal for Numerical Methods in Fluids*, 7, 1093
- Marasco, A. & Fraternali, F. 2011, *A&Ap*, 525, A134
- Marasco, A., Fraternali, F., & Binney, J. J. 2012, *MNRAS*, 419, 1107
- Marasco, A., Marinacci, F., & Fraternali, F. 2013, *MNRAS*, 433, 1634
- Marinacci, F., Binney, J., Fraternali, F., et al. 2010, *MNRAS*, 404, 1464
- Marinacci, F., Fraternali, F., Nipoti, C., et al. 2011, *MNRAS*, 415, 1534
- Melioli, C., Brighenti, F., D’Ercole, A., & de Gouveia Dal Pino, E. M. 2008, *MNRAS*, 388, 573
- Melioli, C., Brighenti, F., D’Ercole, A., & de Gouveia Dal Pino, E. M. 2009, *MNRAS*, 399, 1089
- Miller, M. J. & Bregman, J. N. 2015, *ApJ*, 800, 14
- Miyoshi, T. & Kusano, K. 2005, *J. Comput. Phys.*, 208, 315
- Nipoti, C. & Posti, L. 2014, *ApJ*, 792, 21
- Norman, C. A. & Ikeuchi, S. 1989, *ApJ*, 345, 372
- Oort, J. H. 1966, *BAIN*, 18, 421
- Oosterloo, T., Fraternali, F., & Sancisi, R. 2007, *Aj*, 134, 1019
- Putman, M. E., Saul, D. R., & Mets, E. 2011, *MNRAS*, 418, 1575

- Rees, M. J. & Ostriker, J. P. 1977, MNRAS, 179, 541
- Regan, J. A., Haehnelt, M. G., & Viel, M. 2007, MNRAS, 374, 196
- Salem, M., Besla, G., Bryan, G., et al. 2015, ApJ, 815, 77
- Sancisi, R., Fraternali, F., Oosterloo, T., & van der Hulst, T. 2008, A&A, 15, 189
- Sarazin, C. L. & White, III, R. E. 1987, ApJ, 320, 32
- Sembach, K. R., Tripp, T. M., Savage, B. D., & Richter, P. 2004, ApJs, 155, 351
- Shapiro, P. R. & Field, G. B. 1976, ApJ, 205, 762
- Shu, F. 1991, The Physics of Astrophysics: Gas dynamics, Series of books in astronomy No. v. 2 (University Science Books)
- Spitzer, L. 1956, Physics of Fully Ionized Gases
- Stone, J. M., Gardiner, T. A., Teuben, P., Hawley, J.F., & Simon, J. B. 2008, ApJS, 178, 137
- Stone, J. M. & Norman, M. L. 1992a, ApJS, 80, 753
- Stone, J. M. & Norman, M. L. 1992b, ApJS, 80, 791
- Sutherland, R. S. & Dopita, M. A. 1993, ApJS, 88, 253
- Toro, E. F. 1997, Riemann solvers and numerical methods for fluid dynamics: a practical introduction (Berlin , New York: Springer)
- Wakker, B. P. 2001, ApJs, 136, 463
- Wakker, B. P., Savage, B. D., Sembach, K. R., Richter, P., & Fox, A. J. 2004, in Astronomical Society of the Pacific Conference Series, Vol. 331, Extra-Planar Gas, ed. R. Braun, 11
- Wakker, B. P., York, D. G., Wilhelm, R., et al. 2008, ApJ, 672, 298
- Zafar, T., Péroux, C., Popping, A., et al. 2013, A&Ap, 556, A141
- Zschaechner, L. K., Rand, R. J., Heald, G. H., Gentile, G., & Kamphuis, P. 2011, ArXiv e-prints